A Measurement of Jet Cross Sections at Low Q^2 and an Interpretation of the Results in Terms of a Partonic Structure of the Virtual Photon.

by

Mark Smith

September 1999

Oliver Lodge Laboratory
University of Liverpool

A Measurement of Jet Cross-Sections at Low Q^2 and an Interpretation of the Results in Terms of a Partonic Structure of the Virtual Photon.

Mark Smith

Abstract

Measurements of single inclusive jet cross-sections are presented using deep inelastic scattering data from H1 in the kinematic region $0.65 < Q^2 < 50.0$ GeV^2 and $0.3 < y < 0.6$. The results are compared to a number of QCD based models. Good agreement is found with models which treat the virtual photon as having both a pointlike coupling to the quarks and antiquarks in the proton and a coupling where the photon first acquires a partonic structure before interacting strongly with the proton.

The inclusive dijet cross-sections, measured in the kinematic region $1.6 < Q^2 < 100.0$ GeV^2 and $0.1 < y < 0.7$ are in agreement with the picture of the virtual photon having a partonic structure in the region where $E_T^{*2} \gg Q^2$. The ratio $\sigma(res)/\sigma(dir)$ is also presented and shows the partonic structure of the photon to decrease with increasing photon virtuality.

acknowledgements

I'm not very good with words, as you will no doubt notice when you carry on reading this thesis so here goes:

I'd like to thank all the people who helped me produce this thesis, and also some of the people who hindered it's production in various ways. Thanks go to my Supervisor Tim Greenshaw, and to the other people I worked closely with in the Liverpool group, Steve Maxfield and Tanya McMahon. Thanks for answering a lot of stupid questions (anybody who reckons there's no such thing as a stupid question should work with me for a while). Thanks also to Professor Erwin Gabathuler for allowing me to take on this research project and to PPARC, without whose financial support this research would not have been possible.

LUPC also features highly in my thank list, particularly Andy Herries, Mark Stretton and Dave Foxton. The weekends caving in Yorkshire certainly put things into perspective. I'd like to thank Gavin McPhereson for engaging in various climbing activities which again put things into perspective.

The time spent in Hamburg would certainly have been dull without the following people around:- Dave Milstead, Mike McAndrew and Brian Cox all seemed to have a similar affinity for music and vodka which wasn't shared with the rest of Hamburg. None of us managed to get gout though. Special thanks to Kirstee Hewitt for being great fun out in Hamburg. Molly Anderson whom I disliked when I first met her but I was proved wrong, and Hugh Tallini . Thanks also to Stuart Cox, a part of him will always remain in the Hamburg office.

The Liverpool Office provided a sense of togetherness during the days of writing up (If only to keep warm). Many a happy hour was had in there together with my officemates Gavin McPherson and Mike McAndrew. Thanks also to Ali Sheriden and Moshe Hanlon, especially for putting me up when first moving

3

down to London.Down on the first floor I'd like to thank Dave Muskett and Dom Duxbury for carrying out endless favours (the scouse currency) and for being good laughs.

When writing this thesis I'd like to thank Dave Milstead for critically reading the text; a job I know he enjoyed. Tim Greenshaw and Steve Maxfield also gave constructive comments to the thesis for which I'm very grateful.

And finally my parents for helping me out with a lot more than this Phd over the years.

Authors contribution

The work presented in this thesis uses data collected by the H1 detector during the 1995 and 1996 running period.

As a member of the Liverpool H1 group I was responsible for the maintainence and running of the H1 forward tracking detector. During the period spent at DESY I worked as part of the jets working group and was responsible for aspects of the data selection and jet trigger implementation. I also performed a study of the electron finder and made improvements that were implemented in the analysis software used by H1.

The measurements in this thesis formed part of an H1 paper submitted to Physics Letters B.

Contents

List of Figures

Chapter 1

Introduction

Historically, the deep-inelastic scattering (DIS) of leptons on nucleons has provided us with a great deal of information about the fundamental structure of the proton and the forces binding it together. DIS experiments at SLAC in the 1960s collected data that led to the formulation of the quark-parton model of the proton. This theory was later modified by Quantum Chromodynamics (QCD), the non-abelian field theory describing strongly interacting particles. QCD was developed in analogy with Quantum Electrodynamics (QED), the theory describing the interaction of charged particles. These two theories are covered with increasing detail in references [1],[2] and [3]. From the results of several experiments involving hadrons, the proton is believed to consist of three "valence" quarks (u,u,d possessing charge $\frac{2}{3}$, $\frac{2}{3}$ and $-\frac{1}{3}$ respectively in units of the proton charge) and a sea of virtual quark-antiquark pairs. The experiments also found that the quarks only account for $\frac{1}{2}$ of the proton's momentum. QCD predicts that the missing momentum is carried by gluons, the mediators of the strong force.

The large centre of mass energy available at HERA permits the study of a kinematic range that is two orders of magnitude larger in the photon virtuality (Q^2) than previous fixed target experiments, and two orders smaller in the Bjorken scaling variable x. The increased energy also allows features such as high transverse energy jet production to be observed.

In addition to deep-inelastic scattering interactions, in which a highly virtual photon probes the structure of the proton, there is a class of interactions where the incoming lepton radiates an almost real photon that proceeds to interact

14

with the proton. This class of processes, termed "photoproduction", dominates the cross section at HERA. With the photon energies available at HERA real photons can fluctuate into a partonic object before interacting with the proton. These "resolved" processes have been observed in lower energy ep interactions and also in e^+e^- collisions. Their study has enabled the structure of the photon to be mapped out using either a highly virtual photon probe in e^+e^- interactions, or by using a highly virtual parton probe from the proton in ep collisions.

At present the structure of the real photon is reasonably well constrained both through measurements from lepton-photon processes that occur at e^+e^- colliders and from measurements of jet production in ep experiments such as HERA. However, despite theoretical interest in the subject, little is known about the transition region between photoproduction and deep-inelastic scattering. Until recently there existed only one measurement of the structure of the virtual photon[8]. HERA is an ideal place to investigate this transition region. Photons are radiated from the incoming lepton with virtualities ranging from almost zero (10^{-7}) to 10^5 GeV^2. The rate of interactions involving these photons is sufficient to allow a detailed study of their characteristics and to test models that interpolate between photoproduction and DIS. This thesis investigates the transition region between photoproduction and deep-inelastic scattering by studying ep collisions which produce jets with large transverse energy.

An overview of the theory of deep-inelastic scattering is presented in chapter 2 followed, in chapter 3, by a general description of the H1 detector with emphasis placed on the detector components used in this analysis. Chapter 4 outlines the process of selecting deep-inelastic events containing at least one jet before the method of extracting the jet cross section is shown. Measurements of jet cross sections are shown in chapters 4 and 5, followed by the interpretation of these results in terms of the structure of the virtual photon. The conclusions of the study are drawn in chapter 6.

Chapter 2

Theoretical Overview

The process of deep-inelastic scattering (DIS) of leptons on nucleons can be considered to proceed via the mechanism shown schematically in figure 2.1. The incoming lepton radiates a gauge boson which then probes the structure of the nucleon (a proton in the case of HERA). The kinematics of such a DIS interaction can be described in terms of the 4-momenta of the incident and scattered lepton, the incoming hadron and the exchanged boson.
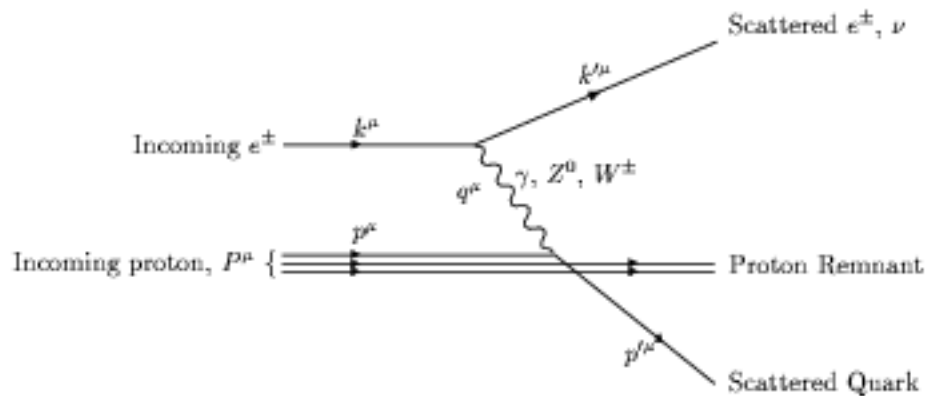
Figure 2.1: Schematic diagram of deep-inelastic ep scattering.

The transverse size of the boson probe is given approximately by $\lambda \propto 1/\sqrt{Q^2}$ where Q^2, the virtuality of the boson, is the negative square of the 4 momentum of the exchanged boson, defined by

$$Q^2 = -q^2 = -(k - k')^2 \tag{2.1}$$

where k and k' are the 4-momenta of the incoming and scattered lepton respectively. W^2 is the invariant mass squared of the $\gamma^* P$ hadronic system.

$$W^2 = (P + q)^2 = M_P{}^2 - Q^2 + 2P \cdot q \tag{2.2}$$

where M_P is the proton rest mass. Another important variable, termed Bjorken x is defined by

$$x = Q^2 / 2P \cdot q \tag{2.3}$$

In the infinite momentum frame of the proton, in which the mass of the proton can be neglected, x can be interpreted as the fraction of the proton's momentum carried by the struck parton. Finally, y is defined as

$$y = P \cdot q / P \cdot k \tag{2.4}$$

which, in the rest frame of the proton, represents the fractional energy loss of the scattered lepton. In the relativistic limit, the above variables are linked by the relations

$$Q^2 = s_{ep} x y \tag{2.5}$$

Where s_{ep} is the total available centre of mass energy.

2.1 The Quark Parton Model.

The lepton-boson vertex shown in figure 2.1 can be calculated in QED, and, if the proton was a point-like object, then the boson-proton vertex could also be calculated this way. From previous experiments, we know that the proton is a composite object and therefore our lack of knowledge of the boson-proton vertex needs to be parameterised. This is done by introducing structure functions and writing the cross section for inelastic lepton-proton scattering as

$$\frac{d^2\sigma}{dx dQ^2} = \frac{4\pi\alpha_{em}{}^2}{xQ^4} \left(y^2 x F_1(x, Q^2) + (1 - y)F_2(x, Q^2) + (y - y^2/2)F_3(x, Q^2) \right) \tag{2.6}$$

Here F_1, F_2 and F_3 are the proton structure functions. These structure functions depend on the distribution of charged objects in the proton. F_3 is the interference term between the photon and the Z^0. This only becomes important when Q^2

approaches the mass squared of the Z^0 and is ignored in the following discussion in which only photon exchange is considered.

The Quark Parton Model provides a physical interpretation for the above formalism by postulating that the proton consists of three non-interacting point-like quarks, each carrying a fraction x of the proton's momentum. A consequence of these assumptions is that the structure of the proton is independent of Q^2 (the structure of the proton can be described as a function of x only). This is termed "Bjorken scaling".

The structure functions provide an experimentally measurable quantity but they are specific to the process of DIS. More general quantities that are applicable to all types of interactions are Parton Distribution Functions (PDFs) $f_i(x, \mu^2)$, which represent the probability to find a parton i in the proton with momentum fraction x when probed at a scale Q^2. The structure function F_2 is related to the parton distribution functions by

$$F_2(x, Q^2) = \sum_i x e_i^2 f_i(x, \mu^2) \tag{2.7}$$

The relation between F_2 and F_1 is given by

$$F_2(x, Q^2) = 2x F_1(x, Q^2) \tag{2.8}$$

Here, the summation is over all the quark colours and also over all flavours of quark that are possible to produce with the energy available. The definition of parton density functions relies on the theorem of factorisation, which states that any cross section can be written as a convolution of the parton level hard scattering cross section $\sigma_{a/b}$ (referred to as the "Matrix element") with the probability of finding the incoming partons in the colliding particle(s). Equation 2.8, known as the Callan-Gross relation is a consequence of the spin $\frac{1}{2}$ nature of the interacting partons.

2.2   The QCD Improved Quark Parton Model.

The theory of Quantum Chromodynamics (QCD) modifies the naive quark parton model. It introduces gluons as the mediators of the strong interaction between quarks, in analogy with the photon as the mediator of the electromagnetic force.

Unlike the photon, the gluons carry colour charge, allowing gluon-gluon as well as quark-gluon interactions. One important implication of this self-interaction of gluons is that, unlike the electromagnetic coupling constant α_{em} which increases with increasing scale, the coupling constant α_s decreases as the momentum scale characteristic of the process involved, μ^2 (which is equal to Q^2 when the photon's virtuality is the largest scale in the event as is the case in DIS) increases.

$$\alpha_s(\mu^2) = \frac{12\pi}{(33 - 2N_F)\ln(\mu^2/\Lambda_{QCD}^2)} \tag{2.9}$$

Here N_F is the number of flavours of quarks. In order for perturbation theory to converge rapidly, αs must be $\ll 1$. This requires a hard scale (large Q^2 or large transverse parton momentum for example) for QCD predictions to be accurate. The scale at which perturbative QCD breaks down is given by Λ_{QCD}. Λ_{QCD} is not a prediction of QCD and must be experimentally determined.

The QCD improved QPM allows for gluon radiation from the quark both before and after the boson-quark vertex. It also allows for a "sea" of virtual $g \rightarrow$ q$\bar{\text{q}}$ fluctuations. A consequence of this is that the structure functions possess a weak dependence on the probing scale Q^2 in the QCD improved QPM model. The distance resolution of the virtual photon probe is given by the uncertainty principal and is proportional to $1/\sqrt{Q^2}$, so at low Q^2 the virtual photon can only resolve the valence quarks in the proton. As Q^2 increases the probe can resolve interactions where the quark has first radiated a gluon. This has the effect of shifting the momentum distribution to lower x as Q^2 increases. Figure 2.2 shows what happens as the virtuality of the photon probe increases. As the photon probe increases in virtuality it is able to resolve more detail in the proton. This allows it to resolve quarks that have radiated gluons before the photon interaction, or have come from the radiated gluons. Each time a parton is radiated the momentum of the parent parton is shifted to lower x.

Although the proton structure is not calculable within QCD, the way in which it evolves with Q^2 is predicted by the Altarelli-Parisi evolution equations [7] shown below.

$$\frac{\partial f_{q_i/p}(x, Q^2)}{\partial \ln Q^2} = \frac{\alpha_s(Q^2)}{2\pi} \int_x^1 \frac{dy}{y} P_{q/q}(\frac{x}{y}) f_{q_i/p}(y, Q^2) + P_{q/g}(\frac{x}{y}) f_{g/p}(y, Q^2) \tag{2.10}$$

$$\frac{\partial f_{g/p}(x, Q^2)}{\partial \ln Q^2} = \frac{\alpha_s(Q^2)}{2\pi} \int_x^1 \frac{dy}{y} P_{g/q}(\frac{x}{y}) f_{q_i/p}(y, Q^2) + P_{g/g}(\frac{x}{y}) f_{g/p}(y, Q^2) \tag{2.11}$$
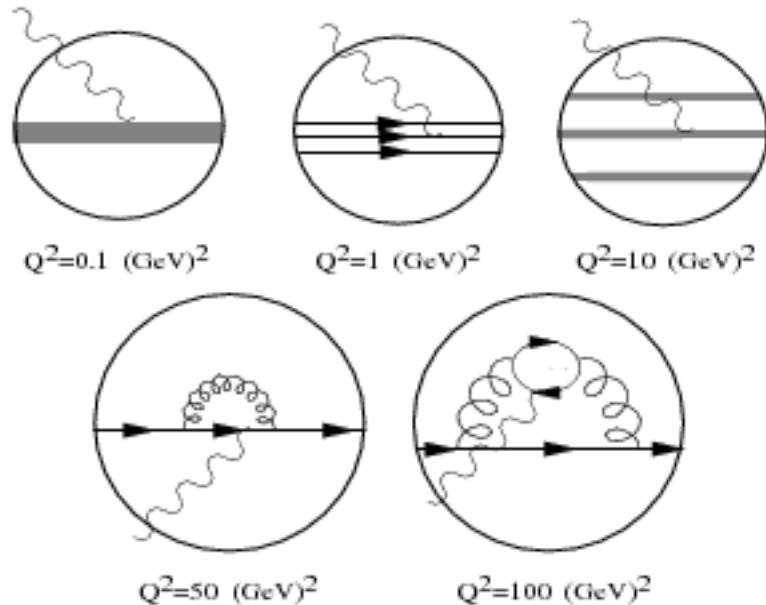
Figure 2.2: The evolution of the parton structure of the proton with Q^2.

$P_{q/q}$, $P_{q/g}$, $P_{g/g}$ and $P_{g/q}$ are the Altarelli-Parisi splitting functions. $P_{a/b}$, where a and b can be either quarks or gluons, represents the probability that a quark a carrying momentum fraction x has originated from a parent quark b of larger momentum fraction y. $f_{a/p}$ are the parton density functions for finding a parton a in the proton.

The evolution of the proton structure as a function of Q^2 is usually represented by a ladder diagram of the type shown in figure 2.3. Each vertex represents an extra order in the perturbative expansion series. In order to calculate the evolution of the proton structure in practice, approximations are made. In the DGLAP approximation [4] the dominant contribution to the calculation for each order in α_s is summed. In the DIS region this corresponds to summing the leading $\ln Q^2$ terms for each order in α_s. In this approximation the transverse momenta relative to the incoming proton direction for each emission are strongly ordered. An alternative approximation is the BFKL approach, where terms in $\ln \frac{1}{x}$ are summed. This means that the BFKL equation is valid in the small x region although at present inclusive cross-section measurements at HERA can be well described by the DGLAP approach.

The solutions to the DGLAP equations depend on the input parton distribu-
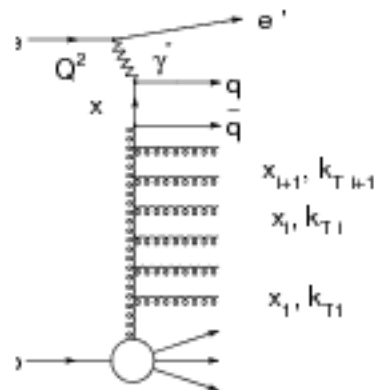
Figure 2.3: Feynman diagram showing the evolution of the structure of the proton as modelled using the DGLAP evolution equations.

tions f_q and f_g at a starting scale μ_0 which must be high enough for perturbative QCD to be valid. These parton distributions have to be measured from data. Once the input distribution has been specified the above equations predict the momentum distributions for higher probing scales.

2.2.1 Photoproduction

Due to the $1/Q^4$ term in equation 2.6 the vast majority of interactions at HERA involve photons of virtuality $Q^2 \approx 0$ (real photons) colliding with the proton, therefore HERA can also be regarded as a photon-proton collider.

The ubiquitous photon is classified as an elementary structureless gauge boson. However, Heisenberg's Uncertainty Principal tells us that it is possible for the photon to acquire partonic structure through the coupling $\gamma \rightarrow q\bar{q}$ as shown in figure 2.4(I). Through further gluon radiation 2.4(II) and (III) the photon can acquire a more complicated structure and, provided the fluctuation lasts longer than the time it takes to traverse the proton, it is possible for the photon to interact with the proton as a partonic object.

In the rest frame of the proton, the photon radiated by the incoming lepton has

Hadronic Fluctuations of the Photon
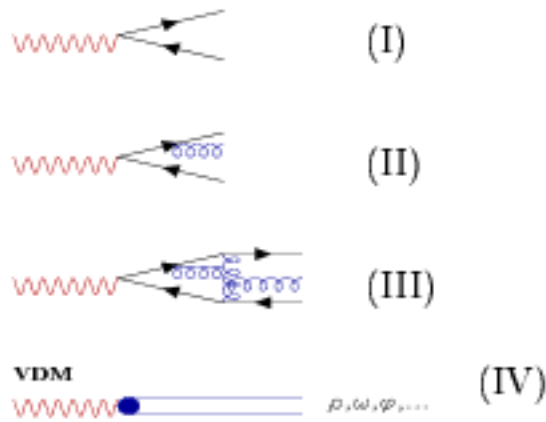
Figure 2.4: The process of a photon fluctuating into a q$\bar{q}$ pair and then acquiring structure through further QCD interactions.

an energy of approximately 20 TeV. At this energy the real photon can fluctuate into a q$\bar{q}$ pair over a distance of approximately 10^4 fm which is much larger than the proton's radius.

2.2.2 Real Photon Structure

In analogy to hadrons, the structure of the photon can be described in terms of parton density functions. But in contrast to hadrons the structure of the photon originates from the $\gamma \rightarrow$ q$\bar{q}$ splitting. The structure of the photon depends on the virtuality of the $\gamma \rightarrow$q$\bar{q}$ fluctuation. If the q$\bar{q}$ are emitted collinear with the incoming photon then the fluctuation is long-lived and gluon radiation can bind the quarks to form a vector meson. This is discussed in more detail in section 2.2.2. If the photon couples to quarks with a large intrinsic transverse momentum (k_t) between them, the fluctuation is too short lived for a complicated structure to be built up. In this region of phase space, perturbative QCD (pQCD) can be used to calculate the resulting contribution to the photon structure.

In this picture the structure of the photon is normally separated into two

independent terms, one corresponding to the non-perturbative part (NP) of the structure, the other to the pQCD calculable part (PT).

$$f_a^\gamma(x, \mu^2) = f_a^{\gamma, NP}(x, \mu^2; \mu_0^2) + f_a^{\gamma, PT}(x, \mu^2; \mu_0^2) \qquad (2.12)$$

The non perturbatively calculable part of the photon structure is normally associated with the fluctuation into a vector meson, and the perturbatively calculable (PT) part, historically termed the "anomalous" part, with the large k_t $\gamma \to q\bar{q}$ fluctuation. The anomalous contribution to the structure of the photon can be calculated in pQCD and is shown below.

$$f_{q/\gamma}(x_\gamma) = e_q^2 \frac{\alpha}{\pi}(x_\gamma^2 + (1 - x_\gamma)^2) \ln \frac{\mu^2}{\Lambda_{QCD}^2} \qquad (2.13)$$

Equation 2.13 depends directly on the scale μ^2 at which the photon is probed, unlike the proton structure where the scale only enters via the evolution equations. It was hoped that a precise measurement of $f_{q/\gamma}(x_\gamma)$ would result in a precise determination of Λ_{QCD}^2 but it has since been realised that the anomalous part of the photon structure cannot be separated from the non-perturbative part [13]. The anomalous part of the photon structure can be seen to rise with increasing μ^2, the scale at which the photon is being probed. If the $q\bar{q}$ pair in the photon are considered as sea quarks in analogy with the proton, then, as μ^2 becomes smaller they cannot be separately resolved and $f_{q/\gamma}(x_\gamma)$ will decrease.

The Vector Meson Dominance model

The Vector Meson Dominance (VMD) model [10], developed to describe soft γN interactions, assumes the photon to be a superposition of a bare photon and a hadronic photon. The hadronic photon is built up as a superposition of vector mesons, the $\rho, \omega \phi...,$ possessing the same quantum numbers as the photon ($J^{PC}=1^{--}$). The cross section for photon-nucleon collisions is then given by,

$$\sigma_{\gamma N} = \sum_{V=\rho,\omega,\phi...} \frac{4\pi}{f_V^2} \sigma_{Vp} \qquad (2.14)$$

where f_V^2 represents the strengths of the $\gamma \to V$ coupling. These couplings have been measured in meson decay experiments[10], and the following values extracted.

$$\frac{f_\rho^2}{4\pi} : \frac{f_\omega^2}{4\pi} : \frac{f_\phi^2}{4\pi} \approx 2.2 : 23.6 : 18.4 \qquad (2.15)$$

The VMD model successfully describes interactions which are dominated by soft collisions (eg. total cross section measurements) but the model fails to describe interactions containing a hard scale.

The VMD and the anomalous part of the photon structure both obey similar evolution equations as for the proton. The evolution equations for the photon are shown below

$$
\frac{\partial f_{q_i/p}(x,\mu^2)}{\partial \ln \mu^2} = P_{\gamma q}(x) + \frac{\alpha_s(\mu^2)}{2\pi} \int_x^1 \frac{dy}{y} P_{q/q}(\frac{x}{y}) f_{q_i/p}(y,\mu^2) + P_{q/g}(\frac{x}{y}) f_{g/p}(y,\mu^2)
$$

$$
\frac{\partial f_{g/p}(x,\mu^2)}{\partial \ln \mu^2} = \frac{\alpha_s(\mu^2)}{2\pi} \int_x^1 \frac{dy}{y} P_{g/q}(\frac{x}{y}) f_{q_i/p}(y,\mu^2) + P_{g/g}(\frac{x}{y}) f_{g/p}(y,\mu^2)
$$

The major difference between the proton and the photon is the $\gamma \rightarrow q\bar{q}$ splitting term:

$$
P_{q/\gamma} = \frac{3\alpha}{2\pi} e_q^2 (x^2 + (1-x)^2) \tag{2.16}
$$

The evolution of the gluon distribution contains no such term as the photon has no coupling to gluons.

2.2.3 Predictions for Jet Cross Sections

QCD predictions are calculable using perturbative techniques as long as there is a hard scale in the event. For DIS, this scale is given by Q^2. For photoproduction Q^2, by definition, is zero and so another scale is required if perturbative QCD predictions are to be accurate. This scale is normally provided by the transverse momentum of the outgoing partons relative to the incident photon-proton direction, and is required to be much larger than Λ_{QCD}. If this is the case then the cross section prediction can be factorised [54] into separate regions. The phenomenologically derived parton distribution functions ($f_{i/A}(x_i)$), evolved to the relevant scale, are used to determine the flux of partons from the initial state hadron, or hadrons in the case of resolved photon interactions. This flux has to be convoluted with the QCD calculation (σ_{ab})of the hard scattering process as shown in equation 2.17.

$$
d\sigma = \sum_{a,b} \int dx_a dx_b f_{a/A}(x_a) f_{b/B}(x_b) d\sigma_{ab} \tag{2.17}
$$

The PDF $f_{i/A}(x_i)$ gives the probability of finding a parton i (quark or gluon) in hadron A. In practice, the perturbative calculation has to be truncated at a certain order. This introduces a dependence on the factorisation scale (μ_F) used to separate the threshold between the QCD calculation and the parton density functions. This can introduce theoretical uncertainty into the prediction.

$$\sigma_{\gamma p \to X} = \sum \int_0^1 \int_0^1 dx_p dx_\gamma \sigma_{a/b}(\mu^2) f_a(x_p, \mu_F^2) f_b(x_\gamma, \mu^2) \qquad (2.18)$$

Here f_a represents the probability of finding a parton a carrying momentum fraction x_p in the proton and f_b the probability of finding parton b carrying momentum fraction x_γ in the photon when probed at a scale give by μ_F^2. The term, $\sigma_{a/b}$, termed the sub-process cross-section, is the prediction of QCD. The summation is over all incoming partons. The number of feynman diagrams contributing towards a process increases factorially with the order of α_s that the process is calculated to. A complete calculation to orders higher than α_s^2 becomes complicated and instead an approximation, called the "Parton Shower" model is used. For parton radiation before the interaction (initial state parton showers), the virtuality of the parton increases with successive emissions. The probability that an emission will occur is given by the Altarelli-Parisi splitting functions detailed in equation 2.12. For radiation after the hard interaction (final state parton showers), the virtuality of the parton decreases with successive emissions until the evolution is stopped at the scale at which α_s becomes large. This is usually taken to be $\approx 1 GeV^2$.

2.2.4 Virtual Photon Structure

In the region $\Lambda_{QCD} \ll Q^2 \ll \mu^2$, the denominator in equation 2.13, Λ_{QCD}, is replaced by the photon's virtuality and the QPM prediction for the virtual photon structure function becomes

$$f_{q/\gamma}(x_\gamma) = e_q^2 \frac{\alpha}{\pi}(x_\gamma^2 + (1 - x_\gamma)^2) \ln \frac{\mu^2}{Q^2} \qquad (2.19)$$

Even in the region of large Q^2, as long as there is a larger scale present in the interaction then large logarithms are present. Therefore as long as a harder scale than Q^2 is present then $f_{q/\gamma}$ is non negligible, and the notion of ascribing structure to the virtual photon is a meaningful one. Hence, for the region $\Lambda_{QCD} \ll Q^2 \ll \mu^2$ equation 2.19 is valid.

In the region $Q^2 = 0$ the photon structure is reasonably well determined experimentally. The transition region between real photons and highly virtual photons where equation 2.19 is valid, is not calculable. Nor is this region tightly constrained by experiment. Theoretical models exist however, described below, which interpolate between the two regions.

The Drees-Godbole (DG) model

Manuel Drees and Rohini Godbole [44], following an analysis by Borzumati and Schuler [11], proposed a phenomenological model to evaluate the effects of including non-zero Q^2 photons in a sample of real photons. These so called "target mass corrections" need to be accounted for when extracting real photon parton density functions.

In the limit $Q^2 \to \mu^2$ the parton densities tend to the values predicted by the QPM, while for $Q^2 < \Lambda_{QCD}$ the Q^2 dependence is negligible. The evolution of the parton densities between these points should be smooth. DG proposed the following ansatz incorporating this behaviour,

$$
\begin{aligned}
f_{q/\gamma}(x, \mu^2, Q^2) &= f^\gamma(x, \mu^2) & Q^2 \leq \omega^2 \\
&= c_q(x, \mu^2) \ln(\mu^2/Q^2) & Q^2 \geq \omega^2
\end{aligned} \tag{2.20}
$$

where $f^\gamma(x, \mu^2)$ are the standard quark PDFs in a real photon. In order to maintain continuity at ω^2

$$
c_q(x, \mu^2) = \frac{f^\gamma(x, \mu^2)}{\ln(\mu^2/\omega^2)} \tag{2.21}
$$

Here, ω^2 represents the value of Q^2 at which the PDFs of the real photon start to become suppressed. The authors recommend using a value of ω of between a few hundred MeV and a GeV [44].

This interpolating factor, although only an approximation, has the correct boundary conditions predicted by QCD. The derivative $\partial f_{q/\gamma}/\partial \ln Q^2$ is discontinuous at $Q^2 = \omega^2$ however. To remove this discontinuity DG proposed a modified

interpolation factor $\mathcal{L}$, given by

$$f_{q/\gamma^*}(x, \mu^2, Q^2) = f_{q/\gamma}(x, \mu^2) \mathcal{L}(\mu^2, Q^2, \omega) \tag{2.22}$$

$$\mathcal{L} = \frac{\ln\left\{(\mu^2 + \omega^2)/(Q^2 + \omega^2)\right\}}{\ln\{(\mu^2 + \omega^2)/\omega^2\}} \tag{2.23}$$

The gluon distribution inside a photon is expected to be further suppressed with increasing virtuality. This can be qualitatively understood from the observation that a gluon has to be radiated from a quark which is itself virtual. If the virtuality of the quark (k^2) is in the region $Q^2 < k^2 < \mu^2$ then the virtuality of the radiated gluon (l^2) lies within the region $k^2 < l^2 < \mu^2$. In the Drees-Godbole model, this increased suppression is acheived by replacing the factor $\mathcal{L}$ by $\mathcal{L}^2$ for the gluon density.

Equation 2.23 is independent of x and does not directly change the x distribution. However because quarks and gluons occupy different regions of x, and as gluons are suppressed more strongly with increasing Q^2, the x distribution is also modified with Q^2.

There is no distinction between the hard perturbative ($\gamma \to q\bar{q}$) and the soft (VMD) components of the photon structure. Therefore the suppression factor should also be valid in the large x region where the perturbative $\gamma \to q\bar{q}$ coupling dominates. In the small x region, because the suppression is logarithmic and not suppressed as $1/(1 + Q^2/m_v^2)^2$, as in the GRS and SaS models described below, the approximation may overestimate the VMD component of the photon PDFs at large Q^2.

The Glück, Reya, Stratmann Virtual Photon Parton Densities

The Glück, Reya and Stratmann GRS parton densities [47] are an extension to the GRV real photon densities. At a low input scale $Q_0 \approx 0.5\,GeV$, the parton densities for the real photon are given by a VMD motivated input. To extend the model to virtual photons, GRS proposed the following boundary conditions to the photon structure.

$$f^{\gamma(Q^2)}(x, \mu^2 = \tilde{Q}^2) = \eta(Q^2) f_{non-pert}^{\gamma(Q^2)}(x, \tilde{Q}^2) + [1 - \eta(Q^2)] f_{pert}^{\gamma(Q^2)}(x, \tilde{Q}^2) \tag{2.24}$$

where $\eta(Q^2) = 1/(1 + Q^2/m_\rho^2)^2$, $\tilde{Q}^2 = \max(Q^2, \mu^2)$ and $m_\rho^2 = 0.59\,GeV^2$. $f_{pert}^{\gamma(Q^2)}$ can be calculated using equation 2.19 in the region where $Q^2 \gg \Lambda_{QCD}$.

The non-perturbative part of the cross section is suppressed as $\sim 1/Q^4$ whilst the perturbative part is suppressed logarithmically as a function of Q^2. The non-perturbative part is therefore suppressed more rapidly so that in the region of large virtuality the splitting $\gamma^* \rightarrow q\bar{q}$ is the dominant contribution to the resolved cross section. Below the input scale ($Q_0 \approx 0.5$) the PDFs for the photon are frozen, the only Q^2 dependence coming from $\eta(Q^2)$. Because of the large uncertainties in the structure of the vector mesons, the VMD component is taken to be proportional to the pion densities f^π.

$$f_{non-pert}^{\gamma(Q^2)}(x, \tilde{Q}^2) = \kappa(4\pi\alpha/f_\rho^2) \begin{cases} f^\pi(x, Q^2) & ; \quad Q^2 > \mu^2 \\ f^\pi(x, \mu^2) & ; \quad 0 \leq Q^2 \leq \mu^2 \end{cases} \tag{2.25}$$

Here, f_ρ^2 gives the probability for the photon to fluctuate into a rho meson. The only free parameter is k, introduced to model the contributions from heavier vector mesons.

The Schuler-Sjöstrand Parton densities.

The Schuler and Sjöstrand approach [46] is similar to that of GRS. They take two sets of real photon PDFs, SaS-1D and SaS-2D, and extend these to non-zero Q^2. The SaS-1D PDFs use a similarly low input scale ($Q_0 \approx 0.6\,GeV$) to the GRS model but instead of approximating the vector meson input by the pion PDF, a fit is performed to the sum of the ρ, ω, and ϕ mesons. The SaS-2D PDFs use a higher input scale ($\mu_0 \approx 2\,\text{GeV}$) and include higher mass vector mesons in the calculation. Heavy flavours are included above a threshold $\mu^2 > m_q^2$ and are treated as massless partons. The Q^2 dependence when probed at a scale μ^2 is included via the following equation.

$$f^{\gamma(Q^2)}(x, \mu^2) = \sum_V \frac{4\pi\alpha}{f_V^2} \left[\frac{1}{1 + Q^2/m_v^2}\right]^2 f^{\gamma, V}(x, \mu^2, \tilde{Q}^2) + \sum_q \frac{\alpha}{\pi} e_q^2 \int_{\tilde{Q}^2}^{\mu^2} \frac{dk^2}{k^2} f^{\gamma \rightarrow q\bar{q}}(x, \mu^2, k^2) \tag{2.26}$$

Here the first summation is over all possible vector meson states (ρ, ω, ϕ), and the second summation is over all possible quarks (u, d, s, c and b). Here $\tilde{Q}^2 = \max(\mu_0^2, Q^2)$.

Considering equation 2.26

- The term inside the first summation represents the probability of finding

the photon in a vector meson state and the second summation term the probability of the photon fluctuating into the "anomalous" $q\bar{q}$ configuration.

- $f^{\gamma,V}(x, \mu^2, \tilde{\mu_0^2})$ represents the vector meson density in the photon. f_V^2 represents the ratios of different vector mesons, and if the different vector meson states are added coherently then the ratio is 1:4 for $u\bar{u}$:$d\bar{d}$.

- The vector meson part is suppressed as $\propto 1/Q^4$.

- In the limit $Q^2 = \mu^2$ the probability of the virtual photon fluctuating into a $q\bar{q}$ pair (second term) vanishes; the probability of a photon fluctuating into a vector meson, although small, is still finite.

- The lower input scale for the VMD states is increased from μ_0 to $\tilde{Q}^2 \geq \mu_0^2$ since the evolution is predicted to start later in μ^2 for virtual photons.

The treatment of the perturbative part is similar to that of the GRS model, the differences in the two models coming from the treatment of the non-perturbative part.

2.3   From Partons to Hadrons

So far the theory has only dealt with partons involved in the hard scattering. Such short distance interactions can be calculated in perturbative QCD as α_s is small. At large distances, corresponding to a small scale, the running of α_s causes it to become large and perturbative QCD cannot be used.

This situation may be viewed in the following way. As two partons are separated, the colour force binding the two quarks together causes the potential energy in the colour field between them to increase. Eventually it becomes energetically favourable to produce a $q\bar{q}$ pair. The quarks then continue to separate and additonal $q\bar{q}$ pairs are produced. This cascade will continue until the potential energy in the field between the partons is sufficiently low to prevent any more $q\bar{q}$ pairs from being formed. The resulting $q\bar{q}$ pairs then form hadrons which are seen in the detector

Models have been developed and tuned to describe this "hadronisation" process and have been implemented into Monte Carlo event generators used to model

QCD predictions.

2.4 Monte Carlo Models

Monte Carlo Models of physics processes are essential for the majority of physics analyses at HERA.

In order to compare results with those obtained using different detectors the data need to be corrected for the limited acceptance, efficiency and resolution of the detector. The complexity of this task excludes evaluating these effects analytically and so Monte Carlo correction methods are used.

Monte Carlo Models are also used to model the non-perturbative long distance physics processes such as hadronisation. This is essential as experimentalists can only measure jets of hadrons in the detector, not partons. An accurate Monte Carlo model is therefore vital if we wish to compare parton based QCD predictions with data that has been corrected for detector effects. A summary of the Monte Carlo programs used in this analysis is given below.

LEPTO

LEPTO [36] simulates deep-inelastic scattering interactions based on the standard electroweak lepton-quark scattering cross section calculations. LEPTO also includes first order (in α_s) matrix element calculations for the Boson-Gluon fusion (BGF) and the QCD Compton (QCDC) processes shown in figure 2.5. These processes are responsible for dijet production in DIS. Higher order radiation is modelled using the DGLAP parton shower algorithm. Hadronisation is performed using the Lund string model as implemented in JETSET7.4

ARIADNE

ARIADNE [38] uses the Colour Dipole model [39] to simulate QCD radiation to all orders. In the CDM model, the partons from the hard scattering together with quarks and diquarks in the proton remnant form colour dipoles which radiate additional partons in analogy to the dipole radiation process in electrodynamics.
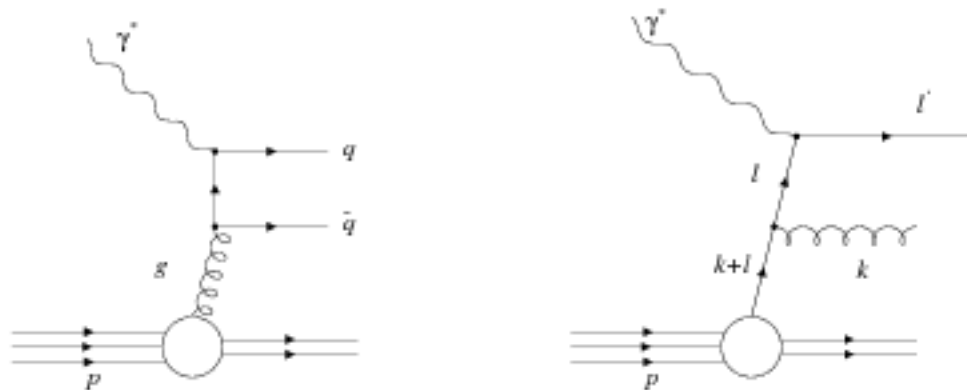
Figure 2.5: The two LO processes responsible for dijet production. On the left is the boson-gluon fusion feynman diagram and on the right is the QCD compton diagram.

These additional partons can then subsequently radiate further partons and the procedure is iterated until a scale of order 1 GeV² is reached and hadronisation is then applied. The CDM model does not include the boson-gluon fusion process, this process is inserted in the ARIADNE Monte Carlo to improve the description of the jet rates and energy flows.

The phenomenological model on which ARIADNE is based leads to parton emissions which are not ordered in transverse momentum, unlike LEPTO. It has been argued ?? that ARIADNE represents the kind of picture shown in figure 2.6 and that this can lead to a similar hadronic final state to interactions where the photon interacts as a partonic object. Since ARIADNE only handles the QCD cascade it has to be interfaced with a Monte Carlo that simulates the hard interactions. JETSET7.4 is used to model the hadronisation process.

2.4.1 DJANGO

DJANGO [42] is a deep-inelastic scattering Monte Carlo that provides an interface between the HERACLES and ARIADNE/LEPTO programs. HERACLES is used to model the effects of photon radiation from the incident and scattered lepton.

For the remainder of the thesis, any references to DJANGO involving a simu-
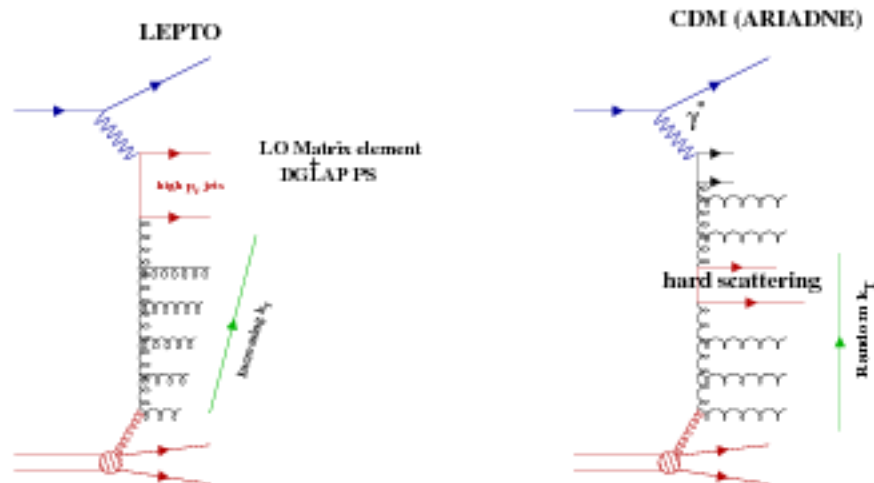
Figure 2.6: The different transverse momentum (k_t) ordering of partons from the proton predicted by LEPTO and ARIADNE.

lation of the H1 detector will refer to the ARIADNE version of DJANGO. When comparing to final physics measurements, reference will be made explicitly to LEPTO or ARIADNE.

2.4.2 HERWIG 5.9

HERWIG 5.9 [40] is a general purpose particle generator used to model photoproduction, DIS, e^+e^- and $p\bar{p}$ processes. HERWIG places emphasis on perturbative QCD; it therefore keeps the number of ad-hoc adjustable parameters to a minimum.

HERWIG 5.9 includes direct and resolved $\gamma - p$ processes generated according to leading order matrix elements and supplemented with parton showering to model higher order effects. HERWIG allows for interference effects (colour coherence) between the initial and final state parton showers. Since the matrix elements are singular as $E_T^{parton} \rightarrow 0$ a lower transverse momentum cut-off is required. The emission of the photon from the incident lepton is generated according to the equivalent photon approximation. HERWIG models the Q^2 evolution of the resolved component using the Drees-Godbole model.

HERWIG uses cluster fragmentation to model hadronisation; it does this by the application of perturbative QCD down to the lowest momentum scales at which QCD is believed to be valid. In the first stage, termed "pre-confinement" partons are clustered to form colour neutral states; in the second step, these states then decay into observable hadrons.

2.4.3 RAPGAP

RAPGAP [41] was originally designed to simulate diffractive processes. RAPGAP also simulates resolved photon interactions for $Q^2 > 0$.

Deep-inelastic scattering processes and resolved contributions to E_T^{jet} production are simulated using leading order QCD matrix elements with an E_T cut-off scheme for light quarks. Initial and final state parton showers are included and hadronisation is performed using JETSET. RAPGAP allows the use of the SaS and GRS PDFs, in addition to the DG model, to describe the Q^2 evolution of the photon structure.

2.4.4 PHOJET

PHOJET models all relevant components of the total photoproduction cross-section including both hard and multiple soft interactions. The hard processes are calculated using leading order QCD matrix elements. Final state QCD radiation and fragmentation effects are implemented using JETSET. The photon flux is calculated using the Weizsacker-Williams approximation. PHOJET is used in this thesis to estimate the level of photoproduction background in the dataset.

2.5 Jet Algorithms

Partons cannot be measured experimentally, only jets of hadrons. A qualitative description of a jet would be "a large amount of hadronic activity within a small angular region", but in order to use jets to quantitatively test and measure QCD, we have to firstly define quantitatively what a jet is. If information is to be extracted about the perturbatively calculable hard scattering then the jet definition

must satisfy the following criteria:

It must be:

- Infared and collinear safe. A jet algorithm is infra-red safe if it doesn't distinguish between a particle, and a particle having radiated another particle of infinitely small momentum. The jet algorithm is collinear safe if it doesn't distinguish between a particle before or after it has emitted a second particle in exactly the same direction as the initial particle was travelling.

- Subject to small hadronisation corrections.

- Unlike e^+e^-, in DIS or p$\bar{\text{p}}$ collisions, the centre of mass energy does not control the hardness of the process, and due to the presence of beam remnants, the high E_T scattering process has to be separated from the underlying soft event. The jets produced by the algorithm should originate directly from the hard scattering process and not be contaminated by the hadron remnants.

There are essentially two classes of jet algorithms, the cone type algorithms where jets are defined by maximising the energy contained in a cone of fixed size, and the clustering algorithms first introduced by the JADE collaboration [26]

For the analysis presented in this thesis, the k_T clustering algorithm is used in the hadronic centre-of-mass frame. This algorithm does not suffer any of the ambiguities inherent in cone algorithms such as overlapping cones, choice of initiators and the introduction of the ad-hoc R_{sep} parameter when comparing with NLO calculations. The k_T algorithm is also motivated by the current understanding of perturbative QCD. The algorithm was used as for p$\bar{\text{p}}$ interactions, and allows particles to be assigned to both a proton and photon remnant[1]. To facilitate this, two infinite momentum pseudo-particles along the incoming photon-proton direction ($\pm$z direction) are included in the clustering procedure. The k_T algorithm used in p$\bar{\text{p}}$ mode defines jets in an *exclusive* way, in that all particles in the event are clustered to either jets or to the beam remnants.

There are two stages to the k_T clustering algorithm :-

---

[1]The facility to assign particles to the photon remnant is used in section 4.10

For every final state hadron k compute

$$y_{kB} = \frac{2(1 - \cos \theta_{kB})}{E_{cut}^2} E_k^2 \qquad (2.27)$$

where the suffix B refers to either the proton or photon beam, E_k is the energy of hadron k and θ_{kB} is the angle between the hadron and the photon-proton axis.

For every pair of hadrons k, l, calculate the following distance measure Y_{kl}

$$y_{kl} = \frac{2(1 - \cos \theta_{kl})}{E_{cut}^2} \min(E_k^2, E_l^2) \qquad (2.28)$$

If one of the y_{kB} has the smallest value of all the above, then particle k is included into the relevant beam jet and does not participate in any further calculations. If one of the y_{kl} has the smallest value, then k and l are combined to form a new "pseudo-particle" by the addition of the four-vectors of k and l.

This procedure is repeated until y_{kB} and $y_{kl} > 1$ and what is left are jets and the beam remnants. E_{cut} therefore sets the scale for jet resolution and separates the hard jets from the beam remnants. E_{cut} was chosen to be 3 GeV in the analysis presented in this thesis. This decision was based upon a study of the photon remnant presented in [28] in which the transverse momentum of the photon remnant was found to be 2.1 ± 0.2 GeV for photoproduction interactions ??. In addition, jets are usually only accepted above a transverse energy threshold, thus ensuring perturbative QCD calculations are valid in this region.

The longitudinally invariant k_T algorithm [29], in contrast to the above method, defines jets in an inclusive way. Again, the jet finding is performed in the photon-proton centre-of-mass frame. The distance measure used is defined by:-

$$d_{kB} = P_{Tk}^2 \quad d_{kl} = \min(P_{Tk}^2, P_{Tl}^2) R_{kl}^2 \qquad (2.29)$$

where

$$R_{kl}^2 = (\eta_k - \eta_l)^2 + (\phi_k - \phi_l)^2 \qquad (2.30)$$

Where η, called the pseudo-rapidity, is an angular variable defined as:

$$\eta = -\ln \tan \frac{\theta}{2} \qquad (2.31)$$

R_{kl}^2 corresponds exactly to the resolution variable used in cone type algorithms. The clustering procedure is as follows:

- Find the pair of particles k, l that have the smallest distance between them.

- Find the smallest d_{kB}.

- If $d_{kl} < d_{kB}$ combine k and l.

- If d_{kB} is the smallest distance measure then particle k is a jet, and is removed from the clustering procedure onto a list of jets.

- Continue until all objects have been placed onto a list of jets, the last objects on the list will be the highest E_T jets in the event.

This definition allows the absorption of the initial-state collinear divergences into universal parton density functions [30].

Chapter 3

The H1 Detector

The Hadron Electron Ring Anlage (HERA), situated in Hamburg, is an ep storage facility and consists of two independent accelerators designed to accelerate and store electrons[1] and protons.

The beams are brought together with zero crossing angle at two interaction points (North and South Halls) every 96 ns. This high bunch crossing rate is necessary to produce a sufficiently high rate of physics events. The H1 and ZEUS detectors are built around the two interaction points and are designed to study all aspects of ep scattering.

In the 1995 and 1996 data taking periods HERA operated with a reduced positron beam energy of 27.55 GeV resulting in a centre-of-mass energy of approximately 300 GeV. During this period HERA operated with 90 positron bunches and 90 proton bunches of which only 86 were colliding, the rest (termed "pilot bunches") being used to determine beam induced background.

3.1   Overview of the H1 Detector

A full description of the H1 detector can be found elsewhere [18] and only those components relevant to this analysis are described in detail here.

The H1 detector was designed to study many aspects of ep physics and so

---

[1]The term electron is generic and taken to mean either electron or positron in this thesis
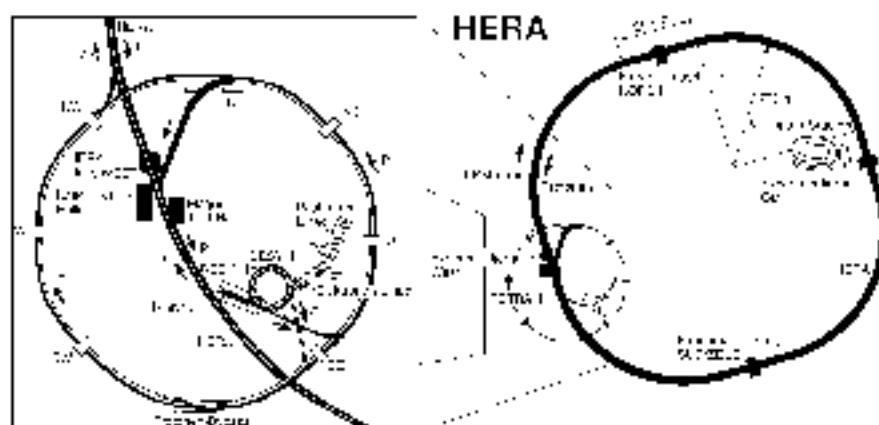
Figure 3.1: Layout of the HERA accelerator complex, including the pre-accelerators and main interaction areas.

consists of a number of sub-detectors that provide complementary information about a collision. The detector has to provide:-

- Good identification and measurement of the scattered electron, since the electron is often used both to identify neutral current DIS events and to measure the kinematics of the scattering process.

- Precise measurements of the hadronic final state. A calorimeter with good energy resolution and fine granularity is especially important for studying the physics of jet production.

- Good luminosity measurement; this is vital for accurate determination of cross section measurements.

- Efficient triggering of physics processes. The high bunch crossing rate (10.4 MHz) means that the detector needs to quickly and accurately distinguish physics processes from the large non-ep backgrounds.

The detector is shown in figure 3.2. It reflects the asymmetric beam conditions with additional tracking and calorimetry in the incoming proton direction. The detector is nearly hermetic, its acceptance for scattered particles is limited only by the forward and backward beam pipe holes.
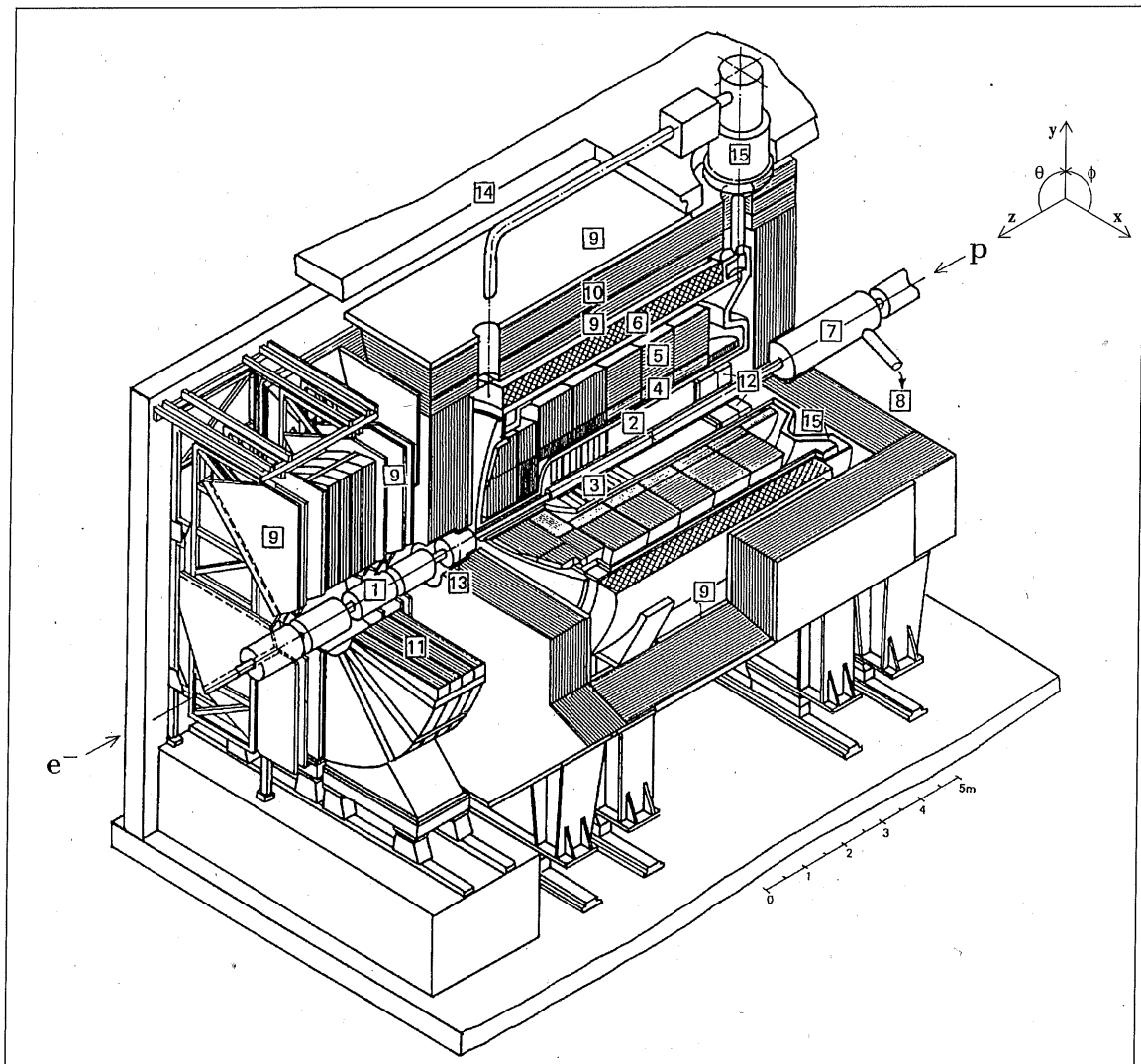
1	Beam pipe and beam magnets	9	Muon chambers
2	Central tracking device	10	Instrumented iron yoke
3	Forward tracking device	11	Forward muon toroid
4	Electromagnetic LAr calorimeter	12	Spagetti calorimeter (SPACAL)
5	Hadronic LAr calorimeter	13	PLUG calorimeter
6	Superconducting coil (1.15 T)	14	Concrete shielding
7	Compensating magnet	15	Liquid argon cryostat
8	Helium supply for 7		

Figure 3.2: Cross-section through the H1 detector. The directions of the incoming beams are shown in the diagram, as are the axes of the H1 coordinate system which has its origin at the nominal interaction point.

The co-ordinate system employed by H1 is also shown in figure 3.2, The origin lies at the nominal interaction point and positive z is defined as the direction in which the proton travels ($\theta = 0$). Throughout this thesis, the regions defined by $\theta < 90°$ and $\theta > 90°$ are referred to as "forward" and "backward" respectively.

3.2 Calorimetry

When a high energy electron or photon interacts with a material, the electric field of the material's constituent atoms cause the incident particle to produce additional particles either by pair production or bremsstrahlung. These additional particles may then undergo further reactions with the material to produce a shower of particles.

Eventually there will not be enough energy for pair production to occur, bremsstrahlung will then be the main source of energy loss until the particle's energy is reduced to the "critical energy" E_c, which is defined as the energy where bremsstrahlung energy loss is equal to energy loss through ionisation. The longitudinal development of the shower is governed by a characteristic of the material it is traversing, called the radiation length (X_o). This is defined as the distance over which the energy of the incident particle is reduced by a factor of e.

The uncertainty on the energy measurement is governed by the statistical fluctuations in the number of particles in the shower. As the number of particles produced is proportional to the energy of the incident electron or photon, the energy resolution is approximately:-

$$\frac{\sigma}{E} \propto \frac{1}{\sqrt{N}} \propto \frac{1}{\sqrt{E}} \tag{3.1}$$

Other terms occur due to noise, calibration uncertainties and leakage of particles produced in the shower. Hadrons, in contrast, lose most of their energy in the form of inelastic nuclear collisions with the absorbing material, resulting in the formation of a shower of "secondary" lower energy particles. The longitudinal dimension of the hadronic shower is characterised by the interaction length (λ_I). This tends to be much larger than the radiation length (for lead $\lambda_I \approx 20 X_o$) and for this reason hadronic calorimeters need to be deeper than their electromagnetic counterparts.

3.2.1   The Liquid Argon Calorimeter

Within H1, the calorimetry in the angular range $4° < \theta < 153°$ is provided by the Liquid Argon (LAr) Calorimeter. The LAr calorimeter is split into two sections, an electromagnetic (EMC) [4] and hadronic (HAC) [5] section. Both are highly segmented, enabling hadronic showers to be distinguished from electromagnetic showers. This is important since the LAr calorimeter is a "non-compensating" calorimeter which means that the energy response for electromagnetic showers is greater than for hadronic showers. A re-weighting of hadronic showers is therefore required.

The LAr calorimeter is a sampling calorimeter. Sampling calorimeters consist of two types of material, a dense, "passive" showering material interspersed with layers of an "active" sampling medium in which the deposited energy can be measured. As the incident energetic particle enters the calorimeter a shower of particles develops in the absorbing material. When the particles pass through the LAr section the argon atoms are ionized, and the resultant charge is measured using rectangular cathode pads.

LAr was chosen as the sampling material because of its high atomic density, which results in the efficient production of large ionisation, its chemical stability, ease of calibration and the homogeneity of response.

The EMC is constructed from layers of 2.4 mm thick lead separated by gaps of 2.35 mm filled with liquid argon. The depth of the EMC varies between 20-30 radiation lengths, the deepest part of the calorimeter being at small θ values where the energies of the particles, due to the asymmetry of the beam energies, are expected to be largest. The measured energy resolution is consistent with $\sigma_E/E = 11.5\%/\sqrt{E} \oplus 1\%$ for electromagnetic particles [24].

The HAC surrounds the EMC and is comprised of 18 mm thick stainless steel layers separated by 2.4 mm LAr filled gaps. The depth of the HAC varies between 5 and 8 λ_I. The energy resolution of the HAC was found to be $\sigma_E/E = 50\%/\sqrt{E} \oplus 2\%$ [24].

3.2.2 The Spaghetti Calorimeter (SPACAL)

Calorimetry in the backward direction of H1 is necessary for two reasons; to provide a precise energy measurement of the scattered electron in the low Q^2 kinematic region and to enable accurate energy flow measurements. To acheive this the SPACAL calorimeter was installed in the 1995 shutdown period.

The SPACAL calorimeter $\boxed{12}$ is a lead/scintillating-fibre calorimeter covering the angular region $153° < \theta < 177.8°$. It has electromagnetic $(22\,X_o \approx 1\,\lambda_I)$ and hadronic ($1\lambda_I$) sections, with energy resolutions of $7.5\%/\sqrt{E} \oplus 2.5\%$ and $38\%/\sqrt{E}$ respectively [21]. The SPACAL timing resolution of better than 1 ns means that it can be used by the trigger to reject non-ep background. Figure 3.3 shows the position of the electromagnetic and hadronic components of the SPACAL in relation to the drift chambers.

The electromagnetic part of the SPACAL consists of 1192 cells of cross sectional area $4.05 \times 4.05\,\mathrm{cm}^2$ each, the hadronic section has 136 cells of cross section $12 \times 12\,\mathrm{cm}^2$ each. The cells are made of grooved lead plates, the grooves being filled with scintillating fibres of diameter 0.5 mm for the electromagnetic part and 1.0 mm for the hadronic section. Incident particles shower in the lead and the products of the shower cause the fibres to scintillate. The fibres are mirrored at the front face to increase light yield. The rear faces of the fibres are connected to light mixers. A small air gap between the light mixer and the fibres guarantees a well defined light transmission. Light output from each cell is then converted into an electronic pulse using photomultiplier tubes (PMTs) having a gain of 10^4 in a 1.2 T magnetic field. Between the SPACAL and the beampipe is a small calorimeter called the "veto-layer" (figure 5.3). This, as its name suggests, is designed to detect events with a large energy deposit in the veto-layer calorimeter. This could be because of leakage from the SPACAL or due to the large amount of beam background that may be present.

3.3 Tracking

The tracking in H1 is divided into three sections, the central track detector (CTD) $\boxed{2}$, the forward track detector (FTD) $\boxed{3}$ and the backward drift chamber (BDC), which is shown in figure 3.3. Each device provides complementary information
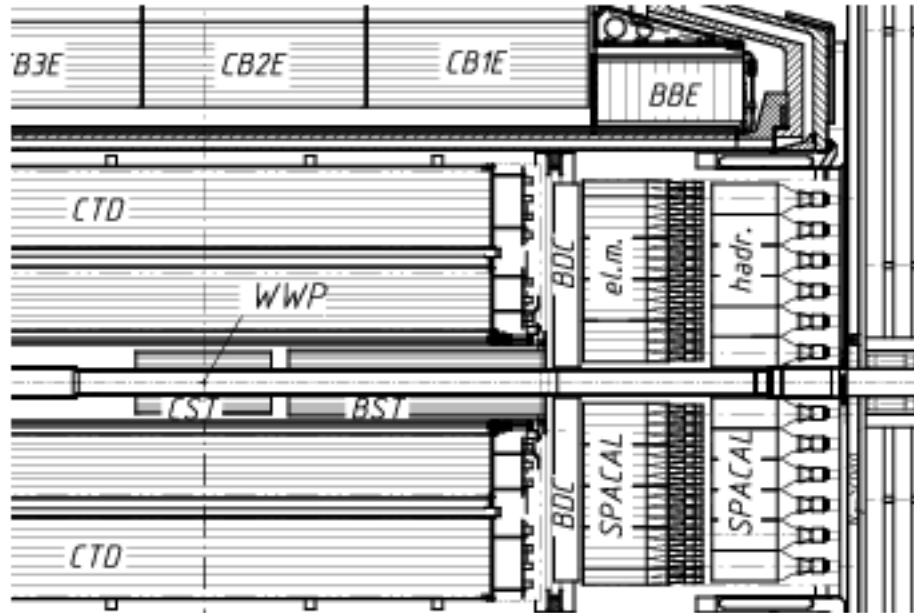
Figure 3.3: Schematic view of the SPACAL calorimeter and backward drift chamber (BDC) in the backward region of the H1 detector.

about the *ep* scattering event. The tracking detectors provide accurate momentum and angle measurement as well as triggering information and particle identification.

The trackers are enclosed inside a superconducting coil $\boxed{6}$ of radius $3\,\mathrm{m}$. This provides a uniform magnetic field of 1.15 T. A superconducting compensator magnet $\boxed{7}$ is used to correct the deviation of the beams caused by the main magnet.

3.3.1   The Central Track Detector

The detectors known collectively as the Central Track Detector $\boxed{2}$ cover the angular region $20° < \theta < 150°$. The CTD consists of a number of interleaved drift chambers and multi-wire proportional chambers. A section through the central tracker can be seen in figure 3.4. Moving radially outward from the interaction point, the inner proportional chamber (CIP), the inner z chamber (CIZ), the inner jet chamber (CJC1) are encountered, followed by the outer z chamber (COZ), the outer proportional chamber (COP) and the outer jet chamber (CJC2).
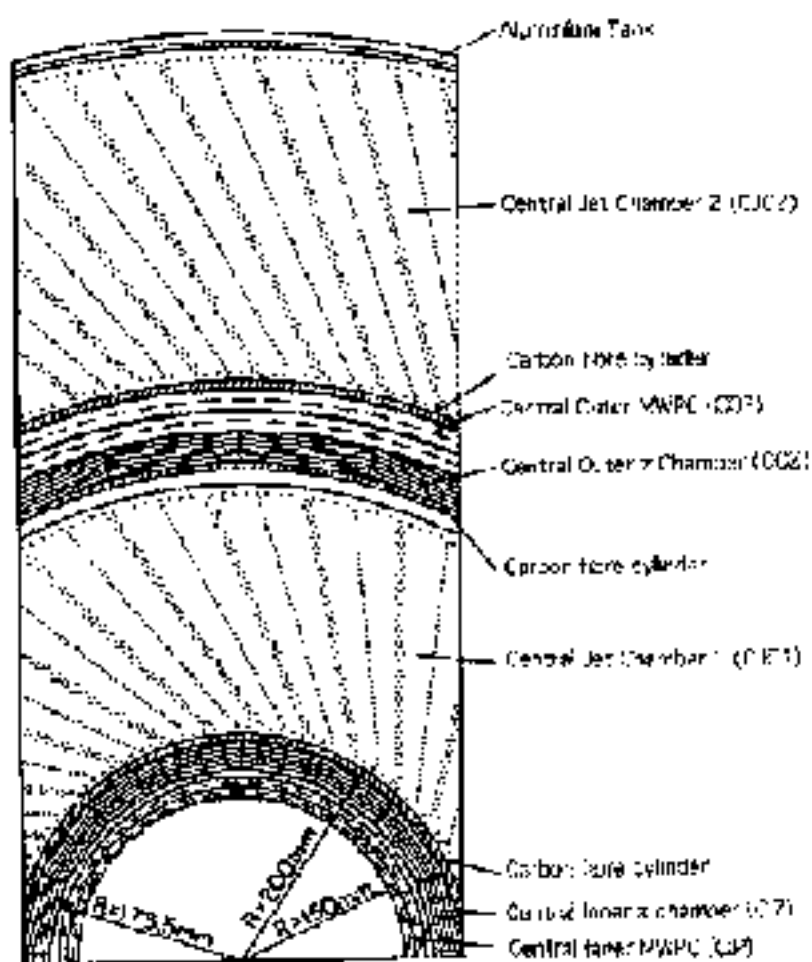
Figure 3.4: r-ϕ view through the CTD

The proportional chambers are used to identify events at the trigger level that have tracks originating from the nominal interaction region. Both the CIP and the COP consist of two concentric cylindrical chambers with anode wires parallel to the beam axis. The signals are read out from the charge induced on the cathode pads. The proportional chambers provide a very quick signal. This, combined with the good time resolution of the proportional chambers ($\sigma \approx 21$ ns) enables the trigger information from the CIP and the COP to be used to define the bunch crossing from which the tracks in the event originated. This bunch crossing time is referred to as t_0.

Reconstruction of tracks in the central region relies mainly on information coming from the central jet chambers (CJC1 and CJC2). In these detectors the anode "sense" wires are strung parallel to the beam direction. CJC1 is divided into 30 cells in ϕ with 24 sense wires per cell, whereas CJC2, with more surface area to cover, has 60 cells in ϕ with 32 sense wires in each cell. The sense wires are staggered by $\pm 150\,\mu$m from the nominal sense wire plane in order to allow resolution of left-right ambiguities. Both ends of the sense wire are read out enabling charge division to be used to obtain a z coordinate with a resolution of approximately 2.2 cm.

The momentum of the particle that produced the track is calculated by measuring the curvature of the track in the H1 magnetic field. In addition, the energy loss of the particle along the track, dE/dx can be used for particle identification.

The two z chambers (CIZ and COZ) are used to improve the z co-ordinate measurement, they provide z co-ordinate information with a resolution of $\approx 300\,\mu$m.

3.3.2 Forward Track detector

Tracks produced at low angles with respect to the proton direction will register fewer hits in the CTD and this will lead to a reduction in the track quality. Most tracks produced at angles $<\ 20°$ will not enter the CTD at all.

The Forward Tracker was designed to measure charged particles in the range $5° \ <\ \theta \ <\ 30°$ and consists of three identical super-modules. Each super-module contains a planar wire drift chamber, a multi-wire proportional counter

(FMWPC), a transition radiation detector and a radial wire drift chamber.

3.3.3   Backward Drift Chamber

Above an angle of 155° tracks are not reconstructed in the CTD. Extending the tracking to cover the backward direction at H1 is important since it allows better measurement of the kinematics in low Q^2 and low x interactions. The BDC, situated directly in front of the SPACAL as shown in figure 3.3, is designed to provide track reconstruction for the final state electron, thus giving a more accurate determination of θ than would be obtained using the SPACAL cluster barycentre alone.

The BDC is subdivided into four double layers of drift chambers in eight octants. The signal wires are strung parallel to the radial direction to optimise the θ resolution. The double layers are rotated by 11.25° to obtain a ϕ measurement. Each double layer is staggered to resolve the left-right ambiguity of the drift direction. The design resolution was 0.4 mm in the radial direction leading to a θ resolution of better than 0.5 mrads in the case where the electron does not initiate a shower of particles before entering the BDC.

The scattered electron track is identified by extrapolating the interaction vertex to the centre-of-gravity of the highest energy SPACAL cluster and finding the closest combination of BDC track hits.

3.4   The Luminosity System

The luminosity system measures the rate of Bethe-Heitler events $ep \to ep\gamma$. This process has a very large cross section (~ 70 mb within acceptance) and can be calculated with very good accuracy using QED.

The luminosity system is shown in figure 3.5. It comprises two small calorimeters, the electron tagger (ET) and the photon detector (PD), situated at $z = -33.4$ m and -102.9 m respectively. The ET and PD are Čerenkov calorimeters, built from arrays of KRS-15 crystals 20 cm ($\approx 22\ X_o$) long. The ET contains 49 crystals and has the dimensions 15.44 x 15.4 cm² while the PD is made of 25
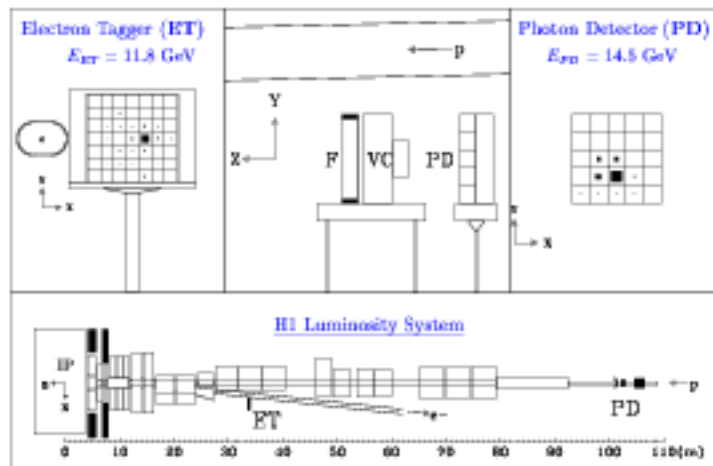
Figure 3.5: The H1 Luminosity system.

crystals and is 10 x 10 cm^2.

Electrons that are scattered through very small angles, with energies different to the beam energy, are deflected in the magnetic field created by the HERA focusing magnets and are detected by the electron tagger if their energy lies between 10 and 20 GeV ($0.3 \leq y \leq 0.6$). Because the electron tagger is not collinear with the beam it does not suffer from background arising from high energy photons.

The main sources of background for the luminosity measurements come from bremsstrahlung processes occuring within the residual gas in the beam pipe. The background is corrected for by measuring the rate of beam-gas events from the pilot bunches and correcting the luminosity accordingly. The PD is protected at the rear from proton beam-halo by a 2 m block of lead, and at the front by a water Čerenkov counter. The water Čerenkov counter prevents synchrotron radiation interacting with the PD and also acts as a veto for out of time photon showers.

The luminosity system can also be used to identify photoproduction processes by requiring an energy deposit in the ET but no energy deposit in the PD.

3.5 The Trigger

A bunch crossing at HERA occurs every 96 ns, which is much shorter than the time taken to read out the H1 detector. As the rate of background processes is far higher than the rate of DIS processes, rapid decisions have to be made to accept or reject the observed events. The H1 trigger system was designed to cope with this complex problem, and presently consists of four levels of event filtering, levels 1, 2, 4 and 5 (L1, L2, L4 and L5.)

The level 1 trigger provides trigger decisions after 2.5 μs. Because the trigger has to collect information from its various sub-detectors, and the bunch crossing time is much shorter than the response time of some of these detectors (in particular the drift chambers have a maximum drift time of $\approx$ 1 μs), the information from the sub-detectors is pipelined, which means the digitised information is stored in a temporary buffer for at least 27 bunch crossings.

Most subsystems in H1 have trigger processors that generate trigger information based on the data they record. The trigger information from the subsystems is sent to the Central Trigger Logic (CTL) which makes logical, physics motivated combinations of the information. These combinations are then tested against predefined conditions, known as sub-triggers. Each time a sub-trigger condition is satisfied an internal counter is incremented. The number of times the sub-trigger condition has to be satisfied before the trigger is "fired" is termed the "pre-scale" value. This prevents high rate sub-triggers from dominating the L1 trigger rate. The CTL then performs a logical OR of all sub-triggers that have satisfied the pre-scale requirements. If this is "TRUE" then an "L1 keep" signal is generated.

Once the first level trigger has decided to keep the event (L1KEEP) "dead time" begins. This is defined as the time in which the detector is insensitive to new physics events. In order to minimise this time, intermediate levels of triggering (L2, L4) are used. These intermediate levels have increasing amounts of information about the event available to them and can reject an event before it is written to tape. This lowers the dead time and allows the detector to accept new events. Approximately 20% of events kept by L1 are accepted by L4 and written to tape. 1% of the rejected events are stored for monitoring purposes.

Offline reconstruction of the event data written to tape is performed at L5.

This uses the H1REC software package to calibrate and reconstruct quantities that are required for physics analysis.

The events are classified according to certain physics criteria. If an event is not classified it is rejected. The classified events are then written to Data Summary Tapes (DSTs) which then form the basis of further physics analysis, as outlined in the next chapter.

Chapter 4

Measurement of Single Inclusive Jet Cross-Sections

4.1 Introduction

The single inclusive jet cross sections

$$\frac{\mathrm{d}\sigma_{ep}}{\mathrm{d}E_T^*} \quad \text{and} \quad \frac{\mathrm{d}\sigma_{ep}}{\mathrm{d}\eta^*}$$

where E_T^* represents the transverse energy and η^* the pseudo-rapidity of the jets measured in the photon-proton centre of mass frame, have been shown to be sensitive to the presence of resolved interactions [5] and to the partonic structure of the real photon. They are also expected to be sensitive to the structure of virtual photon-proton interactions. This chapter studies the characteristics of a sample of interactions containing high E_T^* jets as a function of the photon's virtuality and comparisons are made to various QCD based models.

In section 4.2 the process of selecting deep-inelastic interactions containing jets and the removal of non-DIS background is outlined. Section 4.3 compares different methods of reconstructing the kinematic quantities Q^2 and y. The process of determining the jet cross sections is described in section 4.6 followed by a discussion of systematic uncertainties involved in the measurement in section 4.6.1. The measured single inclusive jet cross sections $\mathrm{d}\sigma_{ep}/\mathrm{d}E_T^*$ and $\mathrm{d}\sigma_{ep}/\mathrm{d}\eta^*$ are presented in sections 4.7 and 4.8. Jet cross sections are presented as a function of the photon's virtuality and transverse energy of the jets in section 4.9. If the photon participates in the interaction as a partonic object then the spectator par-

tons are expected to form a photon remnant in addition to the proton remnant. To investigate this picture, a study of the fraction of the photon's momentum reconstructed as a photon remnant is presented in section 4.10.

4.2   Event Selection

The data analysed in this chapter were collected in two separate running periods. The chosen Q^2 and y ranges ensure that the acceptance and the trigger efficiency were high in both cases.

The data presented in the kinematic range $0.65 < Q^2 < 20.0$ GeV² were taken in a special run in which the mean position of the interaction point was shifted by 70 cm in the +ve z direction. This increased the angular acceptance of the SPACAL down to $\theta = 178.5°$, enabling the measurement of the scattered electron down to $Q^2_{min} \approx 0.3$ GeV². During this "shifted vertex" period, an integrated luminosity of $150\,\text{nb}^{-1}$ was collected by H1. After subsequent off-line selection (sections 4.2.1 to 4.2.2) $121.8\,\text{nb}^{-1}$ was used for physics analysis.

Data in the range $20 < Q^2 < 50\,\text{GeV}^2$ were collected in the 1996 running period and, after off-line selection, correspond to an integrated luminosity of $1\,400\,\text{nb}^{-1}$.

4.2.1   Run Selection

Before making the cross section measurement a pre-selection of the data sample is necessary to ensure that all detectors were functioning reliably and that the beams were stable.

All *ep* runs used for this analysis were required to have all major detector components active for at least 80% of the run time, and on average all major detector components were on for over 95% of the time. In addition, runs were only considered if they had been classified by the shift crew as good or medium quality which means there were no obvious hardware problems with the main detectors used in this analysis.
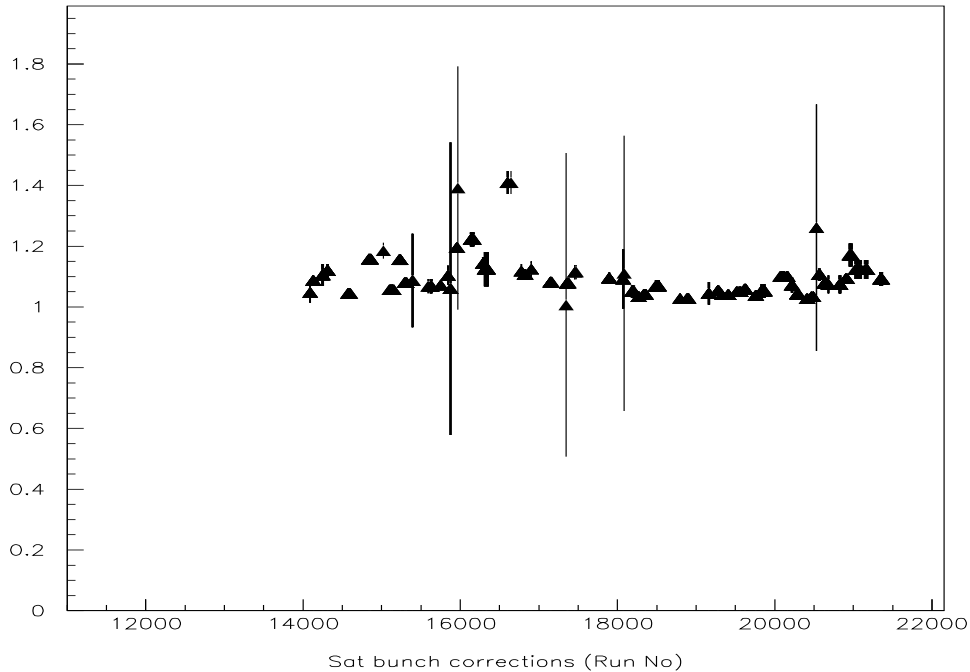
Figure 4.1: The fraction of the total luminosity originating from the forward proton satellite bunches as a function of the run number.

Satellite bunch corrections to the luminosity measurement

As a consequence of the bunch compression needed to reduce the longitudinal size of the proton bunches to its design value of $\sigma_z \approx 11\,\mathrm{cm}$, some fraction of the proton current escapes the main bunch to form a smaller "satellite" bunch, separated from the main bunch by $72\,\mathrm{cm}$ in the incoming proton direction. In this analysis only the main bunch is used for physics purposes, the other bunch being rejected by a cut on the z vertex position. The H1 luminosity system however is equally sensitive to all bremsstrahlung events and so the integrated luminosity must be corrected to take this effect into account.

$$\mathcal{L}_{measured} = \mathcal{L}_{sat} + \mathcal{L}_{nom} = f \times \mathcal{L}_{measured} + (1 - f) \times \mathcal{L}_{measured}$$

where f is the fraction of events that were contained in the satellite bunch, f is shown as a function of run numbers used in this analysis in figure 4.1

Two methods were used to determine the fraction of the luminosity carried by the satellite bunches. The first method uses events from both the shifted and nominal vertex running periods. Events are selected from both periods using identical criteria apart from the z vertex cut. An assumption is made that the spread of the satellite bunch is the same as that of the main bunch. The luminosity fraction carried by the satellite bunch is then

$$f = \frac{N_{sat}}{N_{svd}} \frac{\mathcal{L}_{svd}}{\mathcal{L}_{measured}} \tag{4.1}$$

Here $\mathcal{L}_{svd}$ is the luminosity of the shifted vertex sample, N_{sat} is the number of events surviving the cuts from the nominal vertex sample, N_{svd} is the number of events surviving the cuts from the shifted vertex sample and $\mathcal{L}_{measured}$ is the luminosity measured during the nominal vertex data taking.

The second method normalises the forward satellite bunch to the main bunch. This has the advantage of eliminating any systematic difference during the different data taking periods. Due to the reduced statistical uncertainty, the first method is used to calculate the effect of the satellite bunches and the difference between the first and second method is included in the errors.

Satellite bunches typically contribute a few percent ($\ll 20\%$) of the measured luminosity. On average $\mathcal{L}_{nom}$ is known to an accuracy of better than 2%. This includes the uncertainty of the contribution from the satellite bunches.

4.2.2 Trigger Selection

There are four trigger phases corresponding to different luminosity periods of the luminosity fill. Phase 1 corresponds to the beginning of a fill where the proton and electron beam currents are high. In this phase, because of the high rate of events, the backward calorimeter triggers were either heavily pre-scaled or were turned off. As the background decreases, data taking enters phases 2, 3 and 4 in which all the detectors used in this analysis are operative. For this analysis only phases 2, 3 and 4 were used.

The L1 trigger

Low Q^2 neutral current DIS events are distinguished from other classes of events by the detection of the scattered electron in the SPACAL calorimeter.

Events are selected at the level 1 triggering stage by requiring that the energy deposited in a group of 4×4 electromagnetic SPACAL cells be larger than 4 GeV and that the timing of the energy cluster to be consistent with an ep bunch crossing. Events in which the proton interacts upstream of the SPACAL and deposits an energetic hadron in the SPACAL from the rear will be vetoed by the ToF device [18].

The most energetic cluster in the SPACAL was taken to be the scattered electron. For this analysis, the SPACAL Inclusive Electron Trigger (IET), S0, was used to select events. The efficiency of the S0 trigger is 100% for interactions containing a scattered electron with energy $> 11\,\mathrm{GeV}$ [21]. S0 was not prescaled during the selected shifted vertex running periods.

The L4 algorithm

At level 4 events are processed using a fast version of H1REC. This program has all the information from the detectors but, owing to time constraints, the most accurate calibration cannot be performed. To reduce the time taken to make a trigger decision the algorithm used is split up into logical modules. A module is only executed if its output is required for the L4 trigger to make a decision. The level 4 filter typically removes events in which the interaction point was downstream of the nominal interaction point, but still passed the weaker level 1 requirements. A histogram of the extrapolated tracks is made, and if more than 50% of these tracks lie at $z < -75\,\mathrm{cm}$ then the event is rejected. In order to study the efficiency of the L4 filter 1% of all rejected events are kept for monitoring purposes.

4.3   Kinematic Reconstruction

With the H1 detector, both the scattered lepton and the hadronic final state are well measured. This allows the kinematics of the collision to be reconstructed using the momentum of the scattered lepton ("electron method"), the hadronic final state ("Jacquet-Blondel method") or a combination of both ("Sigma method")[50].

In the laboratory frame, the measurements of the scattered electron angle, θ_e, and the energy, E_e' are used to define the kinematics Q^2 and y by the relationships below. In the following equations E_e represents the incoming electron energy and E_e' the scattered electron energy.

$$Q_e^2 = 4 E_e E_e' \cos^2 \frac{\theta_e}{2} \tag{4.2}$$

$$y_e = 1 - \frac{E_e'}{E_e} \sin^2 \frac{\theta_e}{2} \tag{4.3}$$

The hadronic final state can also be used to define the kinematics by the Jacquet-Blondel method.

$$Q_{JB}^2 = \frac{1}{1-y} \left((\sum_i P_{xi})^2 + (\sum_i P_{yi})^2 \right) \tag{4.4}$$

$$y_{JB} = \frac{1}{2 E_e} \sum_i (E_i - P_{zi}) \tag{4.5}$$

Here, E_i is the energy of the ith hadron, measured in the calorimeter, and P_{xi}, P_{yi} and P_{zi} are the x, y and z components of the momentum of that hadron which is assumed to be massless. The sum is over all final state hadrons i. For particles lost in the forward beampipe $E_i \approx P_{zi}$ and the transverse momentum is small, therefore the contribution to y_{JB} and Q_{JB}^2 is negligible. This is not true however for particles lost in the backward beampipe as the estimation of y_{JB} will be reduced by $\approx 2 E_i$.

In both of the above methods, the incoming lepton energy is taken to be fixed. This is only true in the absence of any initial state radiation which would effectively lower the beam energy and alter the kinematics of the event. The sigma method replaces the denominator in 4.5 by $\sum = \sum_i (E_i - P_{zi})$, where i includes all final state particles excluding the scattered lepton. Momentum conservation requires that this be equal to twice the incoming lepton energy. The advantage of using this formula is that it will give the true lepton energy in the case where the lepton has radiated photons prior to the collision. We thus have:

$$y_\Sigma = \frac{\Sigma}{\Sigma + E'(1 - \cos\theta_e)} \tag{4.6}$$

$$Q_\Sigma^2 = \frac{E'^2 \sin^2\theta_e}{1 - y_\Sigma} \tag{4.7}$$

The electron only method provides a good estimator of the Q^2 of the event. Figure 4.2 (right) shows the resolution to be better than 5% over the Q^2 range considered in this thesis.

Taking the partial derivatives of equations 4.3 and 4.2 with respect to the scattered electron energy and angle give the following:

$$\frac{\delta Q^2}{Q^2} = \left(\frac{1}{E'_e} \oplus \tan\frac{\theta_e}{2} \right) \tag{4.8}$$

$$\frac{\delta y}{y} = \frac{(1-y)}{y} \left(\frac{\delta E'}{E'} \oplus \frac{\delta\theta}{\tan\frac{\theta_e}{2}} \right) \tag{4.9}$$

It can be seen using equations 4.8 and 4.9 that the Q^2 resolution is dominated by the electron energy resolution except at large θ_e. The y resolution is good at high y but degrades at low y due to the term $\propto \frac{1}{y}$ in equation 4.9. The y resolution is shown in figure 4.2 (left) as a function of y.

For the range of Q^2 and y considered in this analysis the electron method gives a more accurate reconstruction of the kinematics of the interaction than the sigma or Jacquet-Blondel methods. Therefore, the scattered lepton is used to determine the event kinematics.
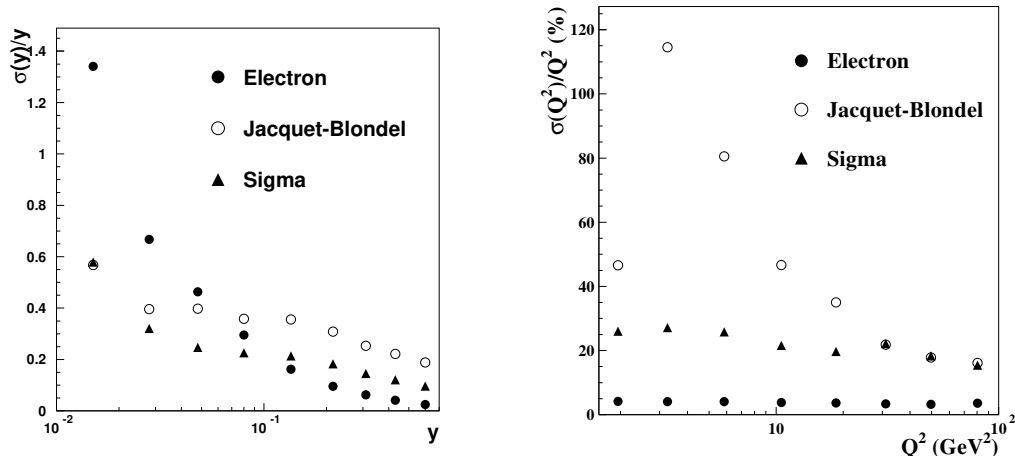
Figure 4.2: Comparison of the resolutions of three different y (left) and Q^2 (right) reconstruction methods, the electron only, Jaquet-Blondel and the Sigma method. The results were obtained using the DJANGO Monte Carlo

4.4 Off-line Event Selection

After the cuts applied at L1 and L4 there is still some residual non-DIS background. To further suppress this background the following cuts are applied:-

- The energy of the highest energy electromagnetic cluster in the SPACAL, which is assumed to be the scattered electron, was required to be greater than 11 GeV. As seen in figure 4.3a, this requirement provides a good filter to reduce photoproduction background. In addition, requiring the energy be more than 11 GeV ensures that the SPACAL electron triggers used for this analysis are 100% efficient.

- The electron cluster barycentre is required to lie more than 8.7 cm from the centre of the beam pipe to ensure that there is little energy leakage into the beam-pipe.

- The transverse spread of an electromagnetic cluster is smaller than that of a hadronic cluster. Hence a requirement that the transverse radius of the cluster be less than 3.5 cm further reduces non-DIS background. The transverse spread of clusters from DJANGO and PHOJET, representing pure DIS and pure photoproduction respectively, is shown in figure 4.3c, along with the position of the cut.

- The electromagnetic cluster is required to have an associated track from the BDC. The association is made by extrapolating a straight line from the z vertex through each BDC track candidate onto the z coordinate of the SPACAL cluster barycentre. The closest extrapolated track was then considered to be the electron. If a track cannot be found within $2.5\,\text{cm}$ from the barycentre of the electron cluster then the event is rejected. This reduces the background from neutral particles (eg γs) faking the electron signal.

- Electrons should deposit all of their energy in the electromagnetic section of the SPACAL whereas a hadronic shower, having a longer interaction length, will penetrate through to the hadronic section of the SPACAL. Figure 4.3d shows the energy deposited within a cone of radius $10\,\text{cm}$ from the barycentre of the most energetic SPACAL cluster for DJANGO and PHOJET events. The event is accepted if the hadronic energy is less than $0.5\,\text{GeV}$ (shown as the line in the figure).

- To reduce the none beam-beam background the position of the z vertex, defined by at least one forward or one central track, is required to be less than $30\,\text{cm}$ from the nominal interaction point, taken to be $+70\,\text{cm}$ for the shifted vertex data sample and $-0.5\,\text{cm}$ for the 1996 data.

- The time, τ, relative to the bunch crossing time t_0, at which the electron deposits its energy in the SPACAL is required to fall between $12 < \tau < 18\,\text{ns}$. This cut removes proton beam related background.

- The sum $\sum_i (E_i - P_{zi})$ which, if no particles escape into the SPACAL beam-pipe, and in the absence of any QED initial state radiation (ISR) should be twice the electron beam energy, was required to be in the range $45\,\text{GeV} < \Sigma_i(E_i - P_{zi}) < 75\,\text{GeV}$. This variable is a good discriminator against photoproduction background events (see Fig. 4.3b) as the scattered lepton escapes detection in photoproduction events. This will reduce $\sum_i (E_i - P_{zi})$ by twice the scattered lepton energy.

The value of θ_e measured using the BDC is used in preference to that obtained using only the SPACAL cluster barycentre. This is because the BDC has a better spatial resolution than the SPACAL.
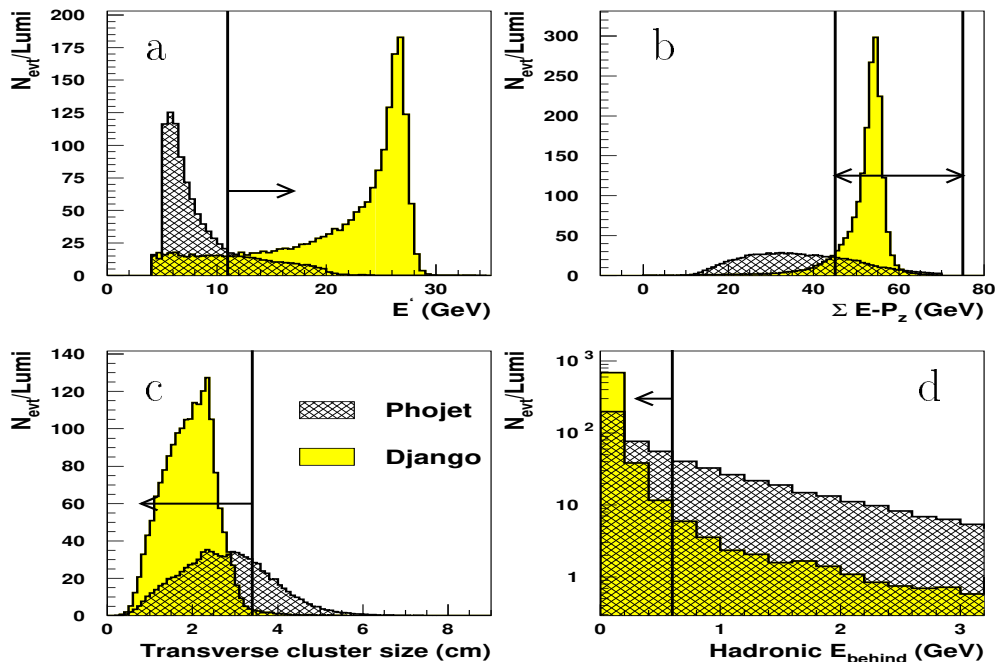
Figure 4.3: DIS (DJANGO) and $\gamma - p$ (PHOJET) comparisons of candidate electron energy (top left), $\Sigma E - P_z$ (top right), transverse cluster size(bottom left) and hadronic energy behind the scattered electron candidate (bottom right). The cuts applied to remove $\gamma - p$ background are indicated by the arrows.

In order to produce results that are defined purely in terms of Lorentz invariant kinematic variables and to enable comparisons with photoproduction data where the scattered electron is detected in the electron tagger, the selection was restricted to the following region of phase space.

- $0.3 < y_e < 0.6$

- $0.65 < Q_e^2 < 50\,\mathrm{GeV^2}$

Here, the subscript e indicates that the scattered electron was used to define these quantities. The lower Q^2 limit of $0.65\,\mathrm{GeV^2}$ was chosen to ensure hermetic detector coverage. No extrapolation to regions beyond the detector acceptance was performed as this would introduce a large dependence on the MC model used to correct the data.

A Monte Carlo study shown in figure 4.4 concluded that after the above cuts had been applied, the photoproduction background, which has a large resolved photon component and hence could have a large effect on the measurement, was less than 3% in all bins presented.

Figure 4.5 shows the distribution of events in the Q^2 and x plane after the above selection cuts.

4.4.1 P_T Balance in the Laboratory Frame

At HERA, neglecting the small transverse momentum of the incoming particles, the vector sum of transverse momentum before the collision is zero. Neglecting particles lost in the forward and backward beampipes after the collision, conservation of momentum then requires that the transverse momentum of the scattered lepton (P_T^e) be balanced by the transverse component of the vector sum of the hadronic momenta (P_T^{had}).

The ratio of P_T^{had} to P_T^e provides a useful measure of the accuracy of the LAr energy scale. P_T^e relies on the well determined electromagnetic energy scale of the SPACAL. The good agreement between data and Monte Carlo for the SPACAL has been demonstrated in figure 4.4. Any difference in the ratio P_T^{had} to P_T^e therefore originates from the uncertainty in the Monte Carlo description of the LAr hadronic energy scale.

Figure 4.6 shows the ratio P_T^{had} to P_T^e for events containing at least one jet with transverse energy $E_T^* > 5\,GeV$ in the kinematic range $Q_e^2 > 1.6$ GeV^2 and $0.1 < y_e < 0.6$. P_T^{had} is calculated from calorimeter clusters. The broadness of the distribution is caused by events in which P_T^e is small . The data-MC agreement implies that the energy scale of the Liquid Argon calorimeter is well described.

4.5 Jet Selection

After the cuts outlined above were applied, a jet finding algorithm was applied to the remaining events.

Jet finding was performed using the k_T clustering algorithm discussed in sec-

1995 Shifted Vertex Data
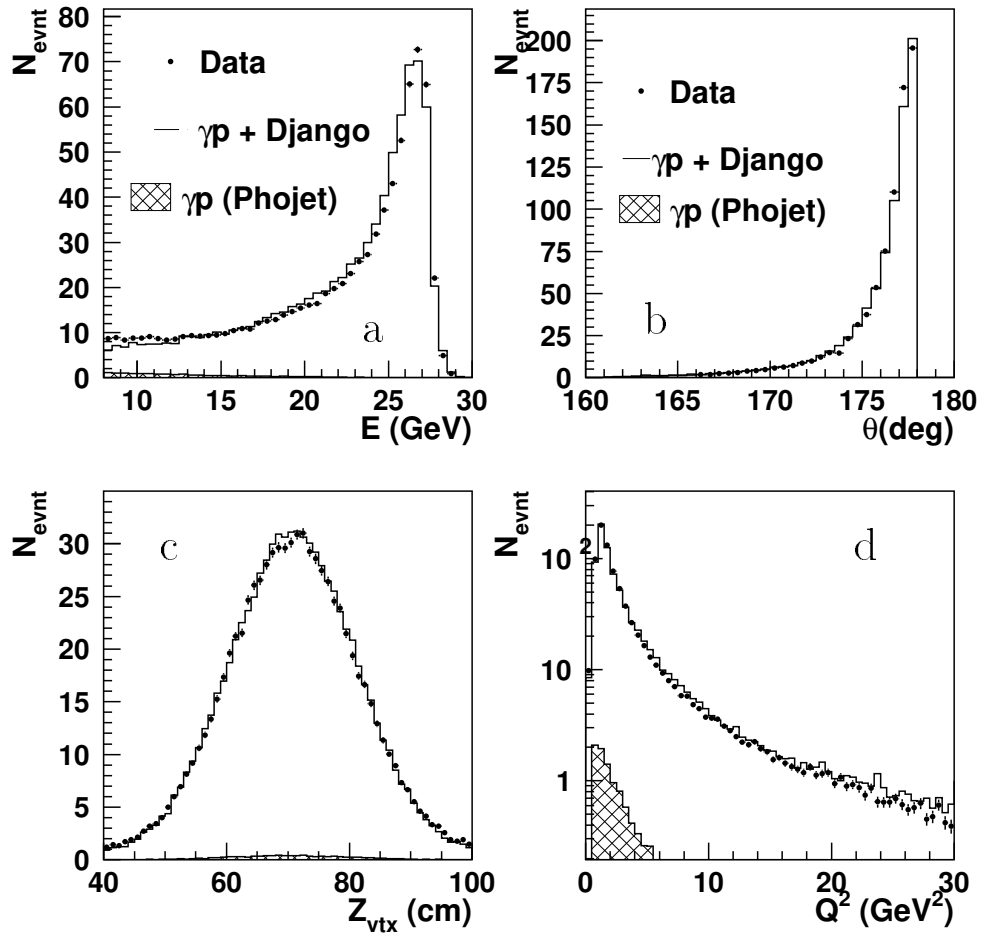
Figure 4.4: The reconstructed quantities: scattered electron energy (a), electron scattering angle (b), z vertex distribution (c) and Q^2 (d) for 1995 shifted vertex data before jet and kinematic cuts have been applied. The data are compared to PHOJET (hatched histogram), used to estimate the photoproduction background, and the sum of PHOJET and DJANGO (solid line)
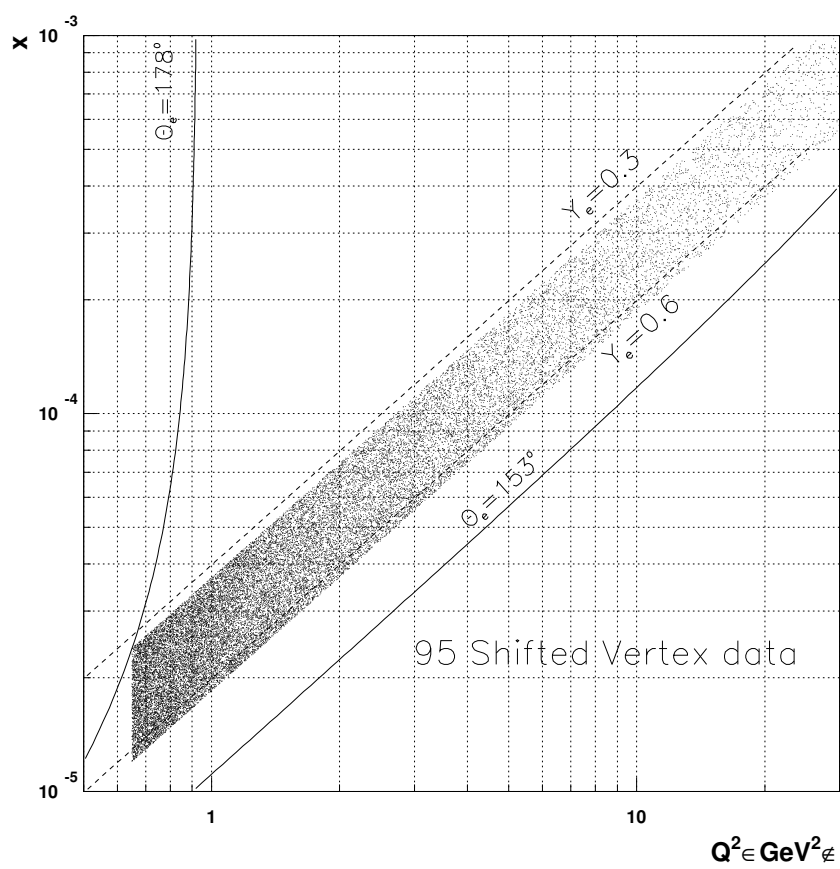
Figure 4.5: Distribution of events surviving selection cuts in the x-Q^2 plane.
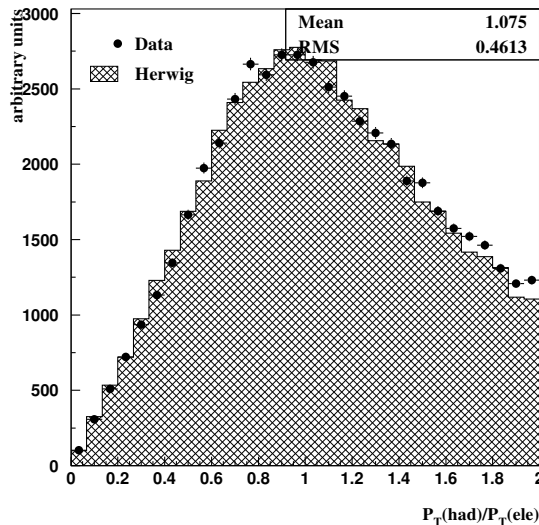
Figure 4.6: P_T^{had}/P_T^e for data and for HERWIG after detector simulation (hatched histogram).

tion 2.5. Jets were reconstructed in the γ^*p frame. This is defined as the frame in which the proton and the photon have equal and opposite momentum. This is the frame recommended in the k_T algorithm prescription for events that have the possibility of containing two remnants [27]. The momentum of the scattered electron 4-vector was used to define the boost vector to the γ^*p frame.

To ensure that the jet cross-section measurements are in a region of phase space where pQCD calculations are accurate and to ensure that the jets lie within the acceptance of the detector the following selection criteria is applied:-

- Transverse jet energy $E_T^* > 4\,\text{GeV}$.

- Pseudorapidity in the range -2.5 $<$ η_{jet}^* $<$ -0.5, with positive η_{jet}^* corresponding to the proton direction.

4.5.1 Jet Characteristics

The transverse energy flow around the jet axis in a slice of $|\eta_{cluster} - \eta_{jet}|$ is shown in figure 4.7 versus the distance in ϕ from the jet axis $\delta\phi = \phi_{cluster} - \phi_{jet}$. A good description of the energy flow uncorrelated with the jet (the jet pedestal)

is important because it will directly effect the jet cross sections predicted by the Monte Carlo.

In HERWIG there is the possibility of adjusting the amount of energy flow that is uncorrelated with the jets. This is called the Soft Underlying Event (SUE). One possible reason for an increase in energy flow could be additional interactions between the spectator partons in resolved events. To investigate this, the predictions of HERWIG with no SUE and with SUE in 15% of the events have been studied.

If the evolution of the jet pedestal as a function of Q^2 is not well described then it is unclear as to whether the change in the jet cross sections as a function of Q^2 is due to the changing pedestal, or the Q^2 evolution of the photon PDFs. Within statistical errors, HERWIG with no soft underlying event (SUE) gives an adequate description of the jet profiles for all values of Q^2 studied here and so for the correction procedure no SUE is included in HERWIG.

To ensure that the reconstructed jets are behaving in a way that is expected from QCD the jet profiles in ϕ were fitted by the function below, which was used in reference [53] to parameterise the characteristics of the jet profile.

$$f(\Delta\phi) = \Lambda \exp(-(\sqrt{|\Delta\phi|} + b)^4 + b^4) + P \qquad (4.10)$$

Here, P represents the underlying event energy (pedestal) and Λ, the amplitude of the jet profile. The full width at half maximum above the pedestal is then

$$\Gamma = 2((\ln 2 + b^4)^{\frac{1}{4}} - b)^2 \qquad (4.11)$$

The jet width (Γ), the pedestal height P and the amplitude of the jet profile Λ are shown as a function of E_T^* in figure 4.8. Perturbative QCD predicts that the jet width decreases with increasing transverse jet energy. Figure 4.8 a shows that the jets measured in this thesis obey this law.

4.6 Acceptance Correction

In order to measure the true cross section for jet production and to allow comparisons with QCD predictions, the measured H1 data need to be corrected to remove the effects of detector inefficiencies and smearing. The data are corrected

1995 Shifted Vertex Data
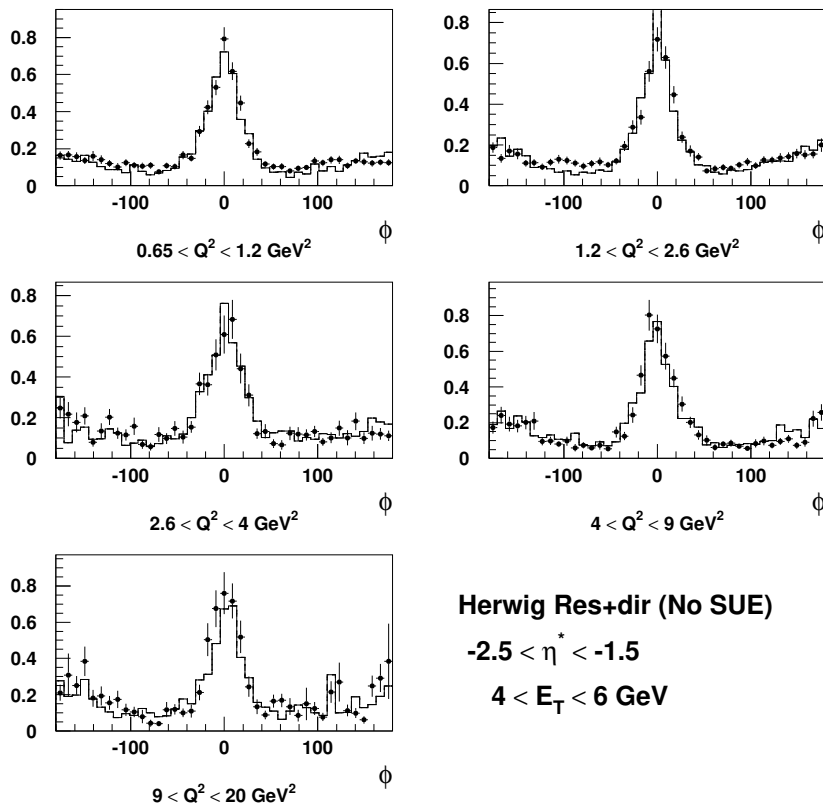
Figure 4.7: Observed transverse energy flow in a slice of pseudorapidity $|\eta_{jet} - \eta_{clus}| < 1$ shown versus the azimuthal angle $\Delta\phi$ for jets selected in data. The histogram represents the prediction from HERWIG with no soft underlying event included after full detector simulation.

back to the hadron level, this is defined as the distributions obtained from Monte Carlo generators after hadronisation of the outgoing partons. To compare directly with pQCD calculations the data would have to be corrected back to the parton level, but this would introduce a strong dependence of the measurements on the particular fragmentation and hadronisation model used for the correction. To avoid this the data are only corrected to the hadron level and pQCD predictions are then compared to the data with the help of a Monte Carlo generator.

The binning was chosen to ensure that all bins had sufficient number of events and to keep the migration of events from one bin to another to less than 60%.

The differential cross sections $d\sigma_{ep}/dE_T^*$ and $d\sigma_{ep}/d\eta^*$ were determined according to the following expressions.

1995 Shifted Vertex Data
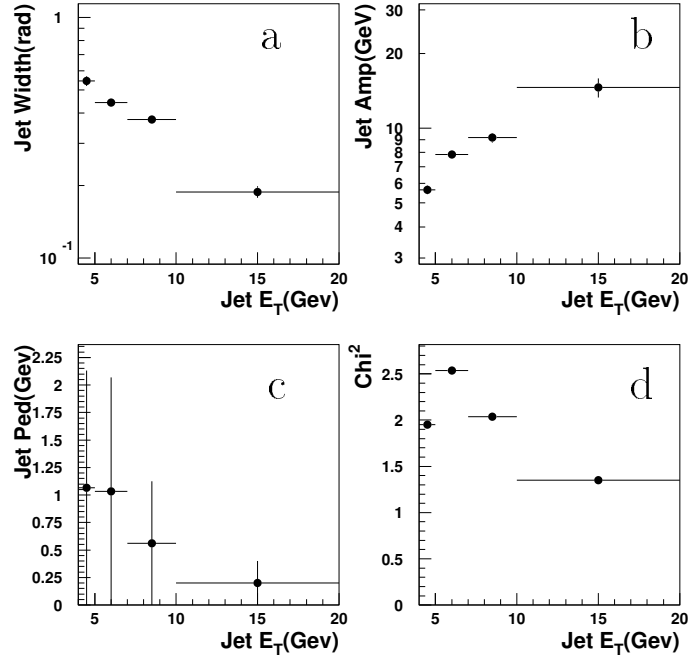
Figure 4.8: The jet characteristics: jet width (a), jet amplitude (b), transverse energy outside the jet (c) and the χ^2 of the fit performed to the jet profile (d) as a function of jet transverse energy.

$$\frac{\mathrm{d}\sigma}{dE_T^*} = \frac{N_{obs}^i}{\mathcal{L}_{nom}} \frac{1}{\varepsilon_{trigger}^i} \frac{1}{\Delta E_{T_i}^*} \frac{Purity(i)}{\epsilon_i} \qquad (4.12)$$

$$\frac{d\sigma}{d\eta^*} = \frac{N_{obs}^i}{\mathcal{L}_{nom}} \frac{1}{\varepsilon_{trigger}^i} \frac{1}{\Delta \eta_i^*} \frac{Purity(i)}{\epsilon_i} \qquad (4.13)$$

where

- N_{obs} is the number of observed data events in a given bin that pass the selection cuts (section 4.4).

- $\mathcal{L}_{norm}$ is the corrected integrated luminosity of the data.

- $\varepsilon_{trigger}$ is the efficiency of the trigger used to select DIS events containing jets. This can be directly determined from the data as there are other uncorrelated triggers used to select DIS events.

- *Purity* is defined as the fraction of measured events that originated in the bin in which they were measured; a low purity implies that a large fraction of the measured data in that bin came from migrations of events originating from outside the bin. Purity is estimated using a MC according to the formula below.

$$Purity(i) = \frac{N^i_{gen\ and\ rec}}{N^i_{total\ rec}} \qquad (4.14)$$

Here $N_{gen}(i)$ is the number of events generated in bin i and $N_{gen\ and\ rec}(i)$ is the number of events measured in bin i that originated from the same bin.

- The Efficiency, ϵ_i, is defined as the fraction of events that stay in the same bin after reconstruction by the detector.

  ϵ_i is estimated using MC events, as the number of events generated and reconstructed in a particular bin, divided by the total number of events generated in that bin.

$$\epsilon_i = \frac{N^i_{gen\ and\ rec}}{N^i_{gen}} \qquad (4.15)$$

The acceptance correction is defined as

$$C^i_f = \frac{N^i_{gen}}{N^i_{rec}} = \frac{Purity(i)}{\epsilon_i}$$

where N^i_{gen} refers to the MC bin content before detector effects and N^i_{rec} corresponds to the bin content after reconstruction by the detector. The data are then corrected by multiplying the content of bin i by C^i_f.

The acceptance correction is performed using Monte Carlo events that have been generated in the same kinematic region as the data and have undergone a full simulation of the H1 detector based on the GEANT program [34]. Two Monte Carlo models were used for the correction procedure, both having passed through the simulation of the H1 detector.

DIS events are modelled using DJANGO. The shifted vertex DJANGO sample corresponds to a luminosity of $218\,\mathrm{nb}^{-1}$ and the nominal vertex sample to a luminosity of $1400\,\mathrm{nb}^{-1}$.

HERWIG 5.9 was used to simulate both direct and resolved DIS events. For the resolved photon contribution, the evolution of the photon PDFs uses the Drees-Godbole parameterisation of virtual photon structure (see section 2). The parameter ω was set to 1 GeV^2. The factorisation and renormalisation scales were set equal to the transverse momentum of the partons involved in the hard scattering with a cutoff set to $P_T^{min} = 1.5$ GeV. The integrated luminositues of the shifted vertex direct and resolved HERWIG sample are 329.04 nb^{-1} and 130.61 nb^{-1} respectively. For the 1996 HERWIG simulation the luminosity was 5204.5 nb^{-1} for the direct sample and 348.96 nb^{-1} for the resolved.

The photoproduction background was modelled using a sample of events generated by PHOJET 1.03 [37]. Events were generated up to a maximum Q^2 of 0.001 GeV^2. The sample corresponds to ~ 300 nb^{-1}. To reduce computer time, events were analysed before undergoing the full simulation of the detector and only events liable to fake a DIS signal were simulated.

The correction factors used to correct the data are determined using the HERWIG Monte Carlo sample which gives a good description of the uncorrected jet E_T^* (Fig. 4.9) and η_{jet}^* (Fig. 4.14) distributions.

4.6.1 Sources of Systematic Uncertainty

In addition to the statistical errors on the measurement there are systematic uncertainties that can influence the results obtained, and whose effects need to be included in the error of the measurement. The complexity of the detector means that analytical error propagation techniques would be too difficult so the relevant parameters for which there is some uncertainty are adjusted in turn and the whole analysis procedure is repeated. The results of the new analysis are then compared with the original measurement and any difference is considered to be a contribution to the systematic error.

- Electromagnetic energy scale uncertainty of the SPACAL.

  The uncertainty in the calibration of the EM energy scale of the SPACAL varies linearly from 3% at 8 GeV to 1% at 27.5 GeV [22]. This can affect the results in two ways. The energy of the electron enters into the determination of the kinematic variables, and is used to calculate the Lorentz boost to

transform objects from the laboratory to the γ^*p frame.

The effect of the energy scale uncertainty was estimated by varying the EM energy scale of the SPACAL by $\pm 2\%$ and repeating the analysis with the new electron energy.

- Uncertainty in the scattered electron angle.

  The uncertainty in the alignment of the BDC leads to an uncertainty in the measured θ_e. The angle θ_e enters into both the estimators of the kinematics for the event and the boost to the γ^*p frame.

  The electron angle was varied by ± 2 mrad to estimate the possible effects on the measurements due to the angle uncertainty.

- The LAr hadronic energy scale calibration uncertainty.

  The transverse energies of the particles comprising a jet will be affected by the calibration of the LAr hadronic energy scale. This will then lead to uncertainties in the transverse energies of the jets.

  To evaluate the effect this will have on the final result, the energies of all the hadronic clusters that had the majority of their energy deposited in the LAr calorimeter was varied by $\pm 4\%$.

- Uncertainty in the hadronic energy scale of the SPACAL.

  The potential miscalibration of the hadronic energy scale of 7% needs to be taken into account. Jets going in the backward direction can deposit large amounts of energy into the hadronic section of the SPACAL.

  The $\Sigma(E - P_z)$ measurement is especially sensitive to the calibration of the SPACAL energy scale. Any error on the energy of a particle (δE) will affect the $\Sigma E - P_z$ measurement by $\sim 2\delta E$.

- Statistical errors on the MC model used to correct the data. Due to limited Monte Carlo statistics the correction factors are not known exactly. An error needs to be assigned to quantify this lack of knowledge.

- Model dependence of the correction factors. If the data are corrected with a model then biases can be introduced. By correcting the data with a different MC model and then including the difference between the two models as a systematic error these biases can be estimated.

  See appendix A for a more detailed account of how the errors were evaluated.

After all the errors have been evaluated they were added in quadrature (they are assumed to be independent). Positive and negative contributions to the errors were added together in quadrature separately. This was done because some systematic errors, like the model dependence, have very asymmetric errors.

The Monte Carlo (HERWIG) used to calculate the acceptance does not include initial (ISR) and final (FSR) state QED radiation. The effect of radiative corrections was studied using the HERACLES program which includes complete first order radiative QED processes. To estimate the effects of radiative corrections, the cross section for jet production was calculated with both radiative effects turned on and off. The percentage difference was then calculated.

$$C_F^{rad} = \frac{\sigma_{non-radiative}^{jet}}{\sigma_{radiative}^{jet}} \qquad (4.16)$$

The only Monte Carlo available that has passed through the detector simulation is a purely inclusive DJANGO file. There are too few events to allow a useful determination of the effects of ISR and FSR, so instead these effects were calculated at the hadron level where it is more efficient to generate events.

In order to simulate the H1 detector, photons within 5 degrees of the scattered electron are merged with the electron, this is a good approximation of a what would happen in a SPACAL calorimeter cell [43].

Generated hadrons that would fall outside the detector acceptance ($\theta_{lab} > 178.5°$ or $\theta_{lab} < 1°$) are ignored to simulate the effects of the H1 detector. This means photons emitted collinearly with the incoming lepton will not be included when recalculating the kinematics of the event. For the radiative Monte Carlo the kinematics and also the boost vector are recalculated after ISR and FSR. The cross section is then evaluated for two files, one including radiative events and the other not.

The effect is 15-25% for jets with E_T^* of 4 GeV and decreases with increasing E_T^* becoming negligible for $E_T^* > 7$ GeV. The results presented in this chapter have not been corrected for radiative effects. The differences in the measurement when including radiative effects have been included in the systematic errors.

4.7 Measurement of the Inclusive Jet E_T^* Spectra

The inclusive jet E_T^* spectra are expected to be sensitive to the presence of resolved processes. The cross section for jet production in resolved events is expected to fall more rapidly with increasing E_T^* than for direct interactions. There are two reasons for this :-

1. If only a fraction of the photon's momentum enters the collision ($x_\gamma < 1$) then the energy available for jet production, $\hat{s}$, and therefore the maximum transverse energy of the jets (E_T^{max}) will be reduced compared to a direct ($x_\gamma = 1$) interaction.

This can be seen in equation 4.17

$$\hat{E}_T = \frac{\sqrt{x_p x_\gamma y s_{ep}}}{2} \sin \theta^* \tag{4.17}$$

Here x_p is the fraction of the proton's momentum involved in the hard collision, x_γ is the fractions of the photon's momentum involved in the collision and θ^* is the scattering angle of the jets in the centre of mass frame of reference.

2. The dominant contribution to jet production over a wide range of E_T^{jet} in the case of resolved interactions involves the exchange of a spin 1 particle (gluon) whereas direct processes involve the exchange of a spin $\frac{1}{2}$ quark. The matrix elements for spin 1 propagators are proportional to $(1 - \cos \theta^*)^{-2}$ or $1/E_T^4$. The QCD matrix elements for spin $\frac{1}{2}$ propagators follow a $(1 - \cos \theta^*)^{-1}$ or $1/E_T^2$ behaviour.

Hence, both the shape and the magnitude of the E_T^* cross section should be sensitive to the presence of resolved processes. Resolved processes should be concentrated more at low E_T^* and low Q^2 . This behaviour is shown in figure 4.9 in which the observed jet E_T^* distribution is shown, and a comparison is made with the predictions of the HERWIG and DJANGO models. Both models have passed through a full simulation of the H1 detector.

The solid curve (HERWIG) is a model containing resolved and direct processes, the dashed curve (DJANGO) is a model of direct only processes. In the region of low Q^2 where resolved processes are expected, the model containing

resolved contributions to the cross section falls more rapidly with increasing E_T^* than the direct model and is consistent with the measured H1 data.
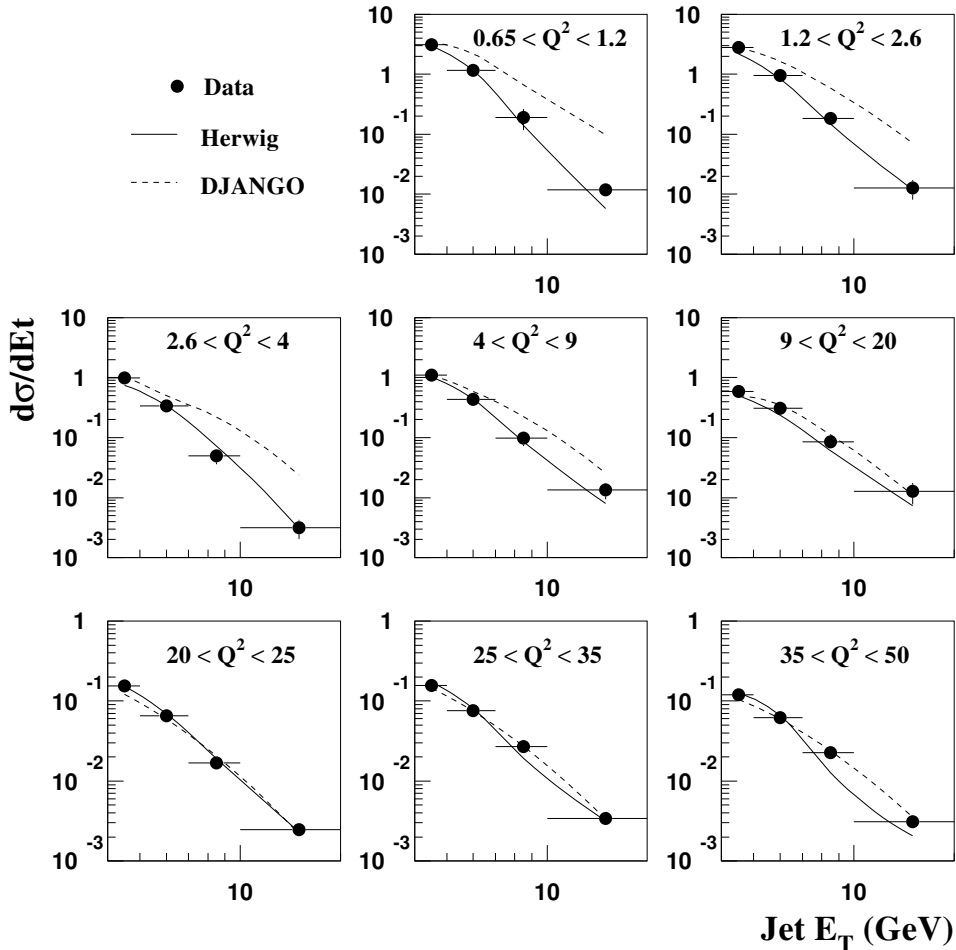
Figure 4.9: The observed E_T^* distribution of jets in the data compared to HERWIG and DJANGO, used to correct the data. Both models have passed through a full simulation of the H1 detector.

To study the migrations between the chosen bins, the E_T^* dependence of the purities of the $d\sigma_{ep}/dE_T^*$ distributions for these Q^2 regions are shown in figure 4.10, as determined using the HERWIG DG and RAPGAP models with a full simulation of the H1 detector. The purity is approximately constant with Q^2 but exhibits a rise with E_T^*. At low E_T^* it is approximately 0.3 and rises to 0.6 for values of $E_T^* > 10\,\text{GeV}$. There is no significant model dependence in these quantities. Similarly, the E_T^* dependence of the efficiency is shown in figure 4.11.
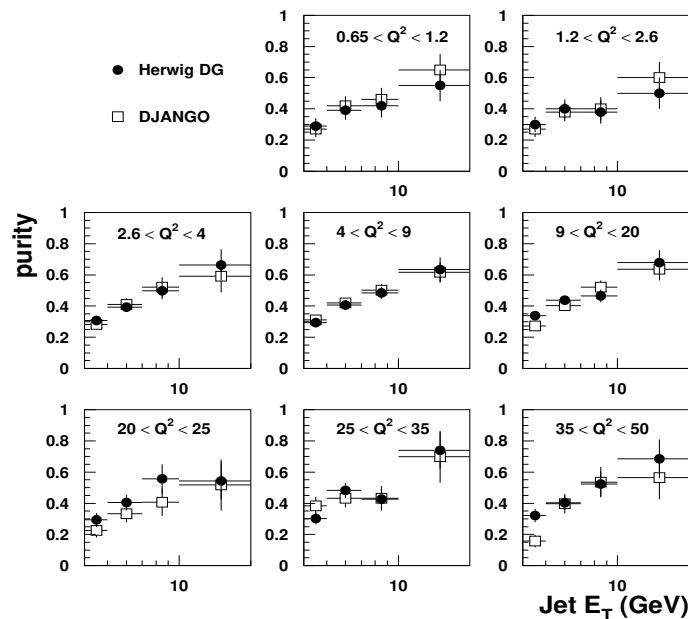
Figure 4.10: Purity (defined in equation 4.14) as a function of E_T^* evaluated using the HERWIG Monte Carlo (filled circles) and DJANGO (open squares).

Again there is no significant Q^2 dependence. The efficiency is typically 0.2 in the lowest E_T^* region and slowly rises to 0.6 for $E_T^* > 10\,\mathrm{GeV}$. Again, both models predict the same magnitude and shape of these distributions.

As can be seen earlier in figures 4.9 and 4.4, both DJANGO and HERWIG-DG provide an excellent description of the resolutions and efficiencies of all important quantities related to the jet and DIS event selections. These can therefore be used to verify that the regions of phase space chosen are not subject to large migration effects or low efficiency.

The correction factors in these E_T^* and Q^2 bins are shown in figure 4.12. Within the statistical precision of the MC models there is no dependence on E_T^* and Q^2. Furthermore, the correction factors determined with the two models are statistically compatible.

The corrected $\mathrm{d}\sigma_{ep}/\mathrm{d}E_T^*$ measurements are shown in figure 4.13, and the values are listed in table C.1. The data are compared to two QCD motivated models, HERWIG direct and HERWIG DG. The data compares well to the HERWIG DG model, which includes a resolved component to the virtual photon.

The HERWIG direct contribution (dashed line) accounts for an increasing fraction of the cross section as Q^2 increases, but, especially in the low Q^2 bins is not sufficient to describe the measured cross section alone.

4.8 Measurement of the Inclusive Jet $\mathrm{d}\sigma_{ep}/\mathrm{d}\eta^*$ Cross Section

The inclusive jet cross sections $\mathrm{d}\sigma_{ep}/\mathrm{d}\eta^*$ is expected to be sensitive to the nature of the photon-proton interaction. Resolved interactions are expected to generate a different jet pseudorapidity distribution than direct events, since, for resolved processes, the parton from the photon involved in the hard collision has only a fraction (x_γ) of the photon's initial momentum. As a consequence of this, the di-parton centre-of-mass system will be boosted more in the incoming protons direction (forward) than it would be for a direct interaction.

For direct interactions, the full momentum of the photon is involved in the collision with a parton from the proton so the di-parton centre of mass system
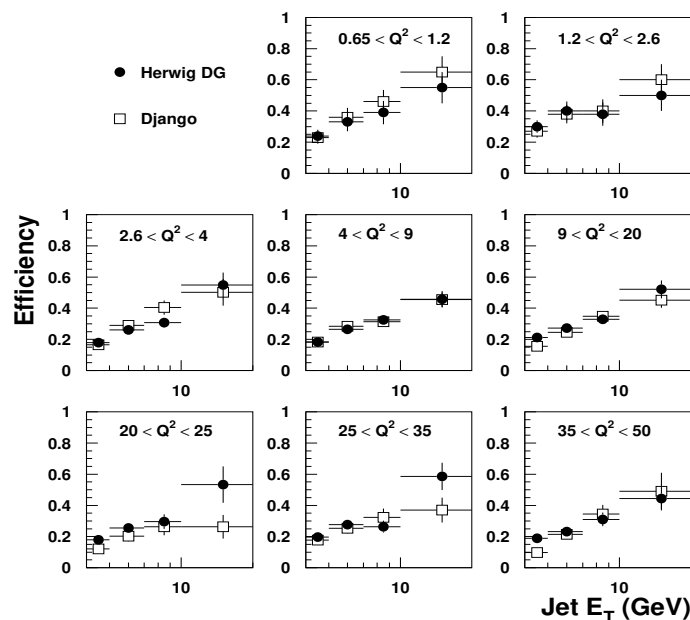
Figure 4.11: Efficiency (defined in equation 4.15) as a function of E_T^* calculated using HERWIG (filled circles) and DJANGO (open squares).
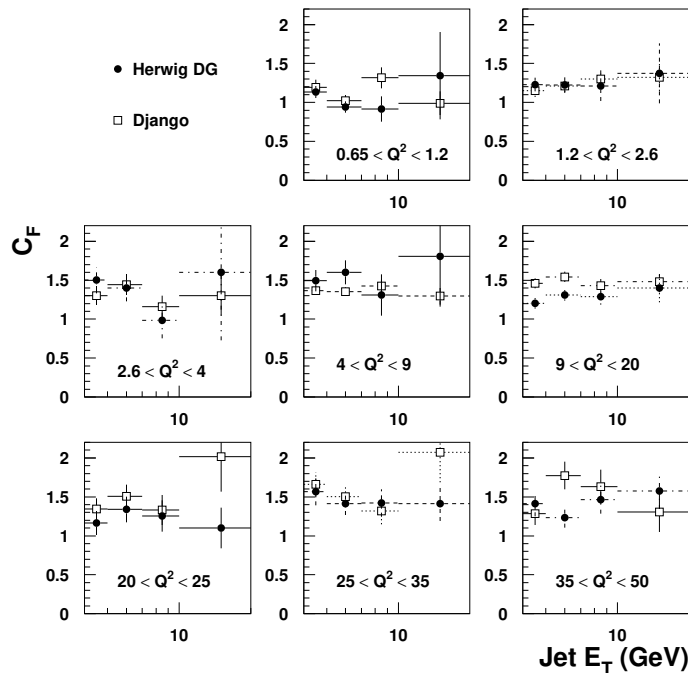
Figure 4.12: Correction factors as a function of E_T^* obtained from HERWIG (filled circles) and DJANGO (open squares).

boost is usually smaller, and the jets will have a tendency to be distributed in the central rapidity region.

Shown in figure 4.14 are the measured H1 data compared to the two Monte Carlo models used to correct the data. The HERWIG prediction is in good agreement with the observed η^* distribution whilst the DJANGO prediction tends to overestimate the observed distribution in the lower Q^2 bins but gives good agreement in the higher Q^2 bins.

Shown in figure 4.15 is the purity as a function of η^* estimated using DJANGO and HERWIG. There is no dependence of the purity on Q^2 or η^*. The effeciency as a function of η^* is shown in figure 4.16. The effeiciency is flat as a function of η^* and Q^2. The average efficiency is 35% and it never falls below 20% in the measured regions.

The correction factors are shown in figure 4.17 as a function of η^*

Figure 4.18 shows the inclusive ep jet cross section $d\sigma_{ep}/d\eta^*$ for jets with
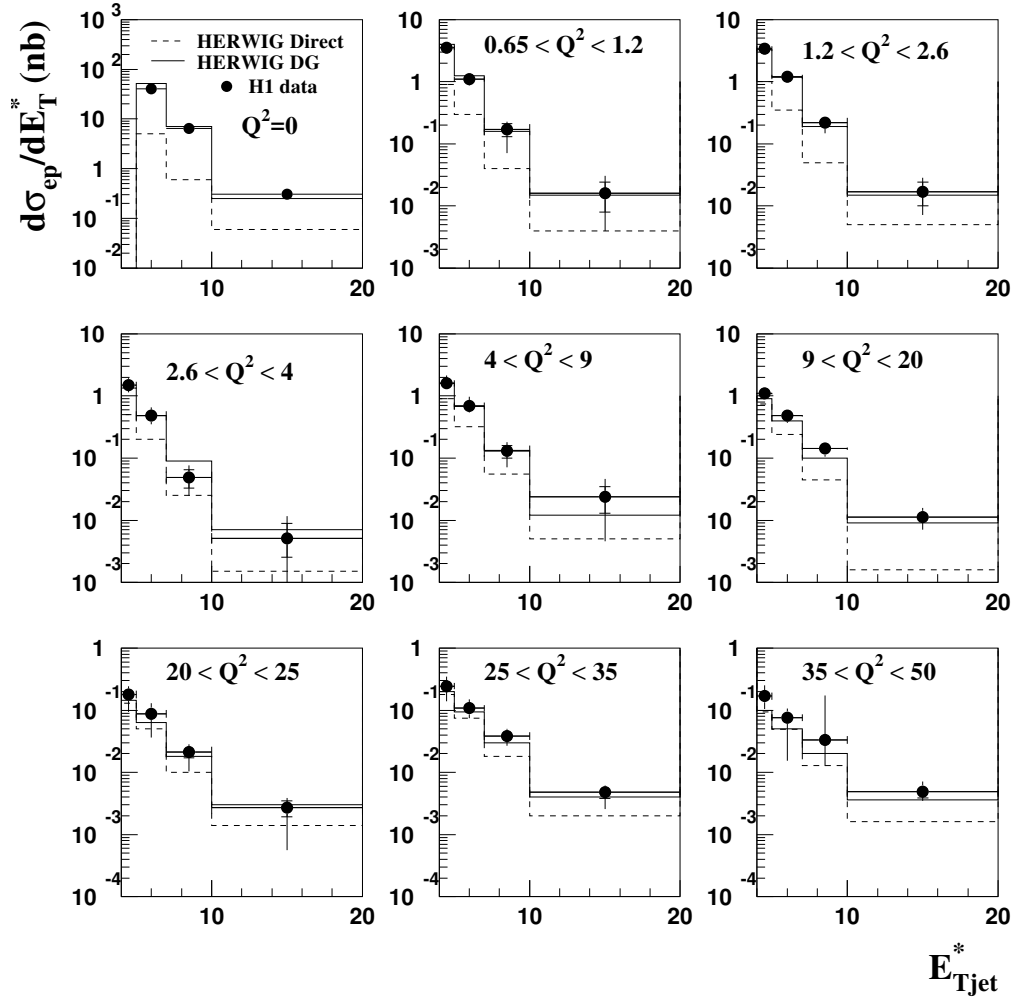
Figure 4.13: The differential jet cross-section $d\sigma_{ep}/dE_T^*$ for jets with $-2.5 < \eta^* < -0.5$ and $0.3 < y < 0.6$. The inner error bars indicate the statistical errors, the total error bars show the quadratic sum of the statistical and systematic errors. Not shown is the error from the uncertainty in the luminosity determination which leads to a 3% normalisation error for the data with $0.65 < Q^2 < 20\,\mathrm{GeV}^2$ and a 2% normalisation error elsewhere. The data are compared to the HERWIG DG model (solid line) and to the direct contribution to this model (dashed line).
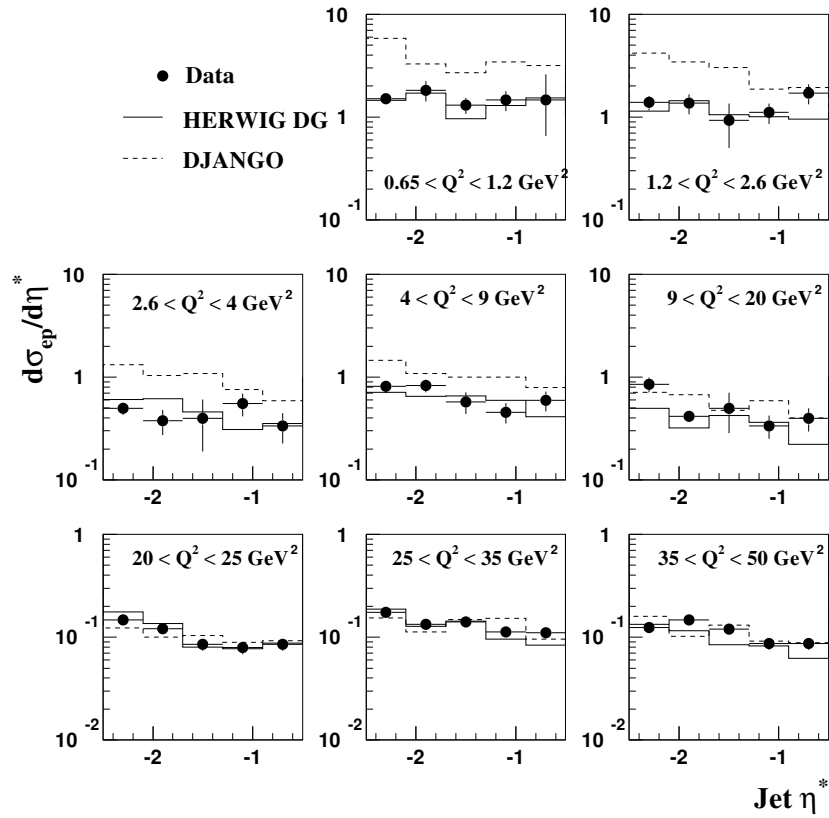
Figure 4.14: The uncorrected data jet η^* distribution for jets with $E_T^* > 5\,\mathrm{GeV}$ compared to the predictions of HERWIG and DJANGO . Both predictions include a full simulation of the H1 detector.
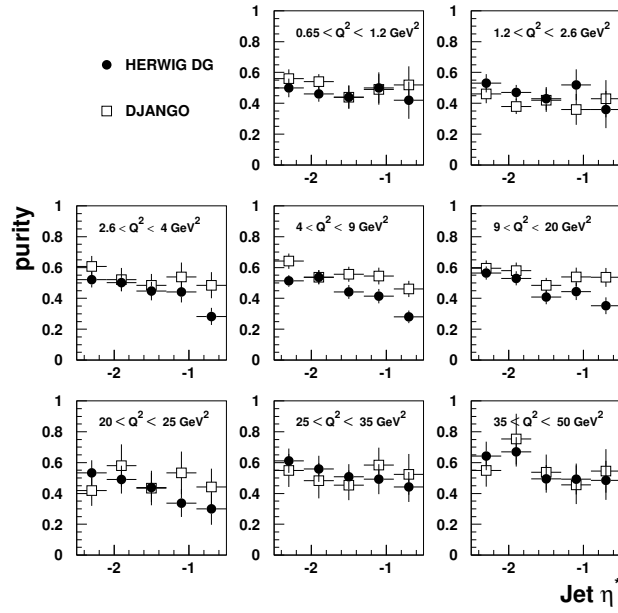
Figure 4.15: Purity as a function of η^*_{jet} calculated from HERWIG (filled circles) and DJANGO (open squares).
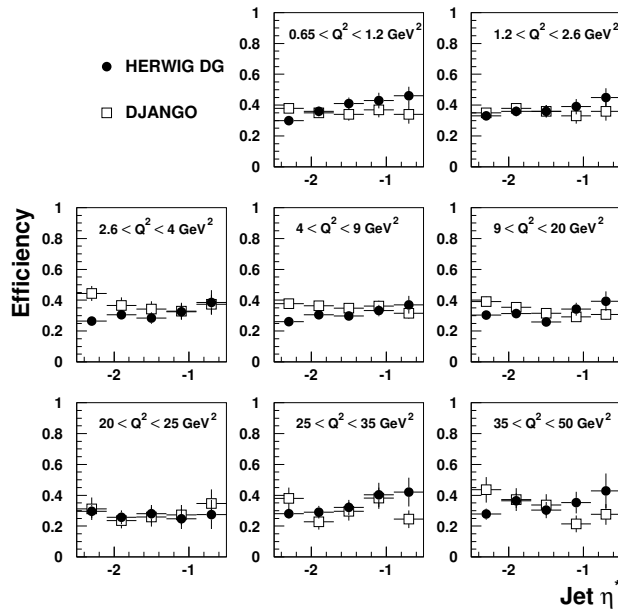
Figure 4.16: Efficiency 4.15 as a function of η^*_{jet} determined using HERWIG (filled circles) and DJANGO (open squares) .
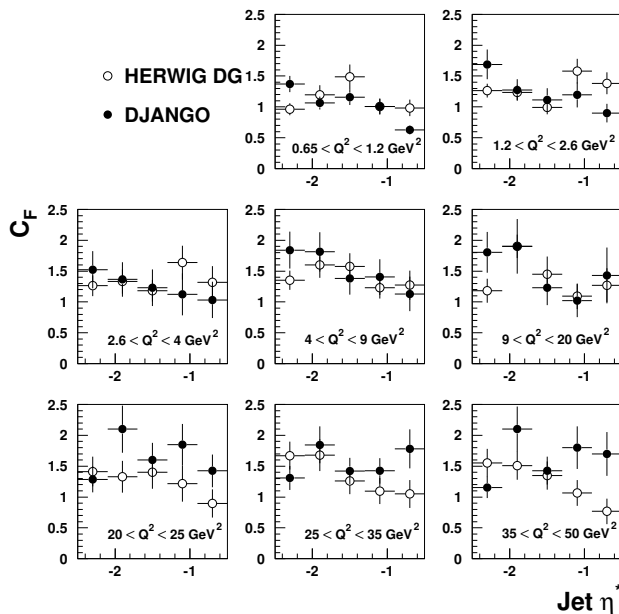
Figure 4.17: Correction factors as a function of η^*_{jet} obtained using HERWIG (filled circles) and DJANGO (open squares).

$E^*_T > 5\,\mathrm{GeV}$ in the kinematic region, $0.65 < Q^2 < 50\,\mathrm{GeV}^2$ and $0.3 < y < 0.6$ compared to two QCD motivated models, HERWIG direct and HERWIG DG. The data compare well to the HERWIG DG model, which includes a resolved component to the virtual photon. The relative contribution from resolved photon processes increases towards the proton direction $(+\eta^*)$.

A model that treats the virtual photon as a purely point-like object underestimates the measured $\mathrm{d}\sigma_{ep}/\mathrm{d}\eta^*$ jet cross section particularly in the lowest three Q^2 bins shown. As the photon's virtuality approaches the transverse energy of the jets, the data are in agreement with the HERWIG direct prediction which treats the photon as point-like.

4.9 Total Inclusive Jet Cross Section as a Function of Q^2

In order to study the Q^2 dependence of the cross sections, the Q^2 dependence of the flux of photon's from the electron, $F_{\gamma|e}$, is factored out using the Weizsacker-
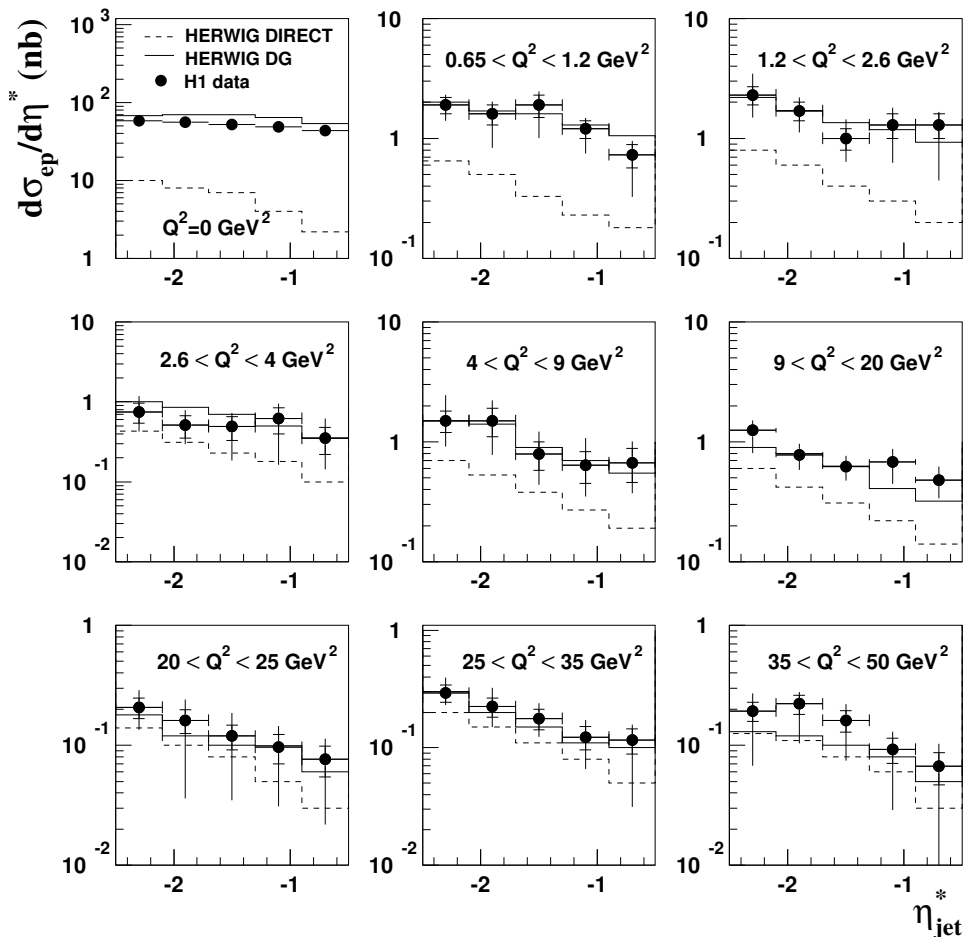
Figure 4.18: The differential jet cross-section $d\sigma_{ep}/d\eta^*$ for jets with $E_T^* > 5\,\text{GeV}$ and $0.3 < y < 0.6$. The inner error bars indicate the statistical errors, the total error bars show the quadratic sum of the statistical and systematic errors. Not shown is the error from the uncertainty in the luminosity determination which leads to a 3% normalisation error for the data with $0.65 < Q^2 < 20\,\text{GeV}^2$ and a 2% normalisation error elsewhere. The data are compared to the HERWIG DG model (solid line) and to the direct contribution to this model (dashed line).

Williams approximation [17]. This converts an ep cross section into a γ^*p cross section using the relationship :-

$$\sigma_{\gamma^*p \to jet+X} = \frac{\sigma_{ep \to e+jet+X}}{F_{\gamma|e}} \tag{4.18}$$

where $F_{\gamma|e}$ is given by

$$F_{\gamma|e} = \int_{y_{min}}^{y_{max}} \mathrm{d}y \int_{Q^2_{min}}^{Q^2_{max}} \mathrm{d}Q^2 f_{\gamma|e}(y, Q^2) \tag{4.19}$$

with

$$f_{\gamma|e}(y, Q^2) = \frac{\alpha}{2\pi Q^2} \left\{ \frac{1 + (1-y)^2}{y} - \frac{2(1-y)}{y} \frac{Q^2_{min}}{Q^2} \right\} \tag{4.20}$$

The flux is integrated over $0.3 < y < 0.6$ and Q^2_{max} and Q^2_{min} are the upper and lower edges of the Q^2 range.

This remains a reasonable approximation [14] at non-zero Q^2 so long as there is a scale harder than Q^2 ($\mu^2 \gg Q^2$) present in the event, as is the case for jet production with sufficiently high E_T^*.

This is true for the majority of the data presented in this chapter, but in some bins of E_T^* and Q^2 the condition $E_T^* \gg Q^2$ is not satisfied. The results are still presented as γ^*p cross sections and the values for the flux factors are presented in table 4.1 so that the ep cross sections can be obtained easily.

The cross section σ_{γ^*p} is shown in figure 4.19 as a function of Q^2 at fixed jet E_T^*. The measured data are compared to two MC models incorporating virtual photon structure. HERWIG includes the Drees Godbole parameterisation of virtual photon structure whilst RAPGAP uses the SaS-2D parton densities of the virtual photon. Also shown are the predictions of HERWIG when no suppression of photon structure with increasing Q^2 is included (dot-dashed line). The resulting cross sections are flat as a function of Q^2 in contrast with the data which show a steep Q^2 dependence. The jet cross sections shown in figure 4.19 are largest in the low Q^2 region and are suppressed as Q^2 increases. This behaviour is consistent with the photon possesing partonic structure that is suppressed as Q^2 increases, as predicted by the two models which give good agreement to the data.
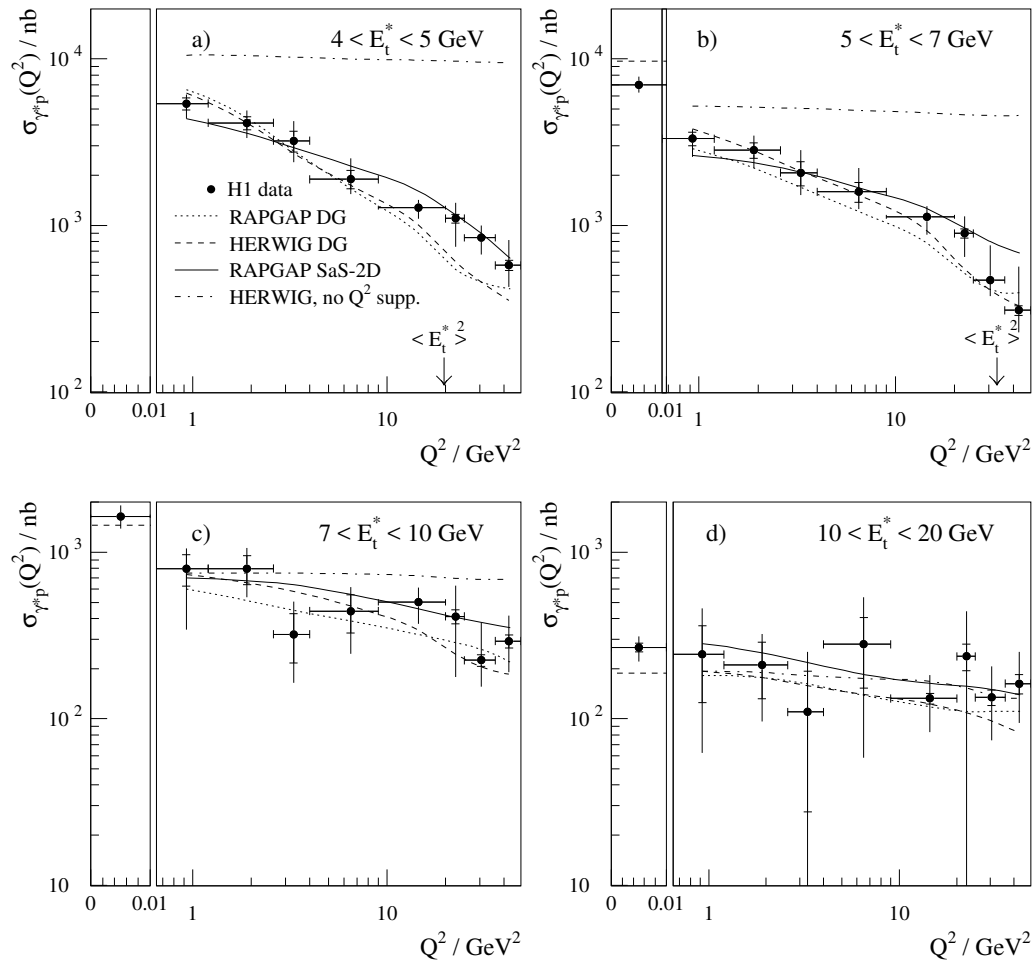
Figure 4.19: The inclusive γ^*p cross section $\sigma(Q^2)$. The data are compared to the HERWIG DG model (solid line) and to LEPTO (dashed line).

Q^2 (GeV^2)	Flux factor
$< 10^{-2}$	1.16×10^{-2}
$0.65 < Q^2 < 1.2$	6.56×10^{-4}
$1.2 < Q^2 < 2.6$	8.27×10^{-4}
$2.6 < Q^2 < 4$	4.61×10^{-4}
$4 < Q^2 < 9$	8.68×10^{-4}
$9 < Q^2 < 20$	8.54×10^{-4}
$20 < Q^2 < 25$	2.39×10^{-4}
$25 < Q^2 < 35$	3.60×10^{-4}
$35 < Q^2 < 50$	3.81×10^{-4}

Table 4.1: The flux factors used to convert ep to γ^*p jet cross-sections (see equation 4.19).

The same data are shown in figure 4.20 compared to two different MC predictions that treat the photon as a point-like object. Both DIS models give a good description of the data in the three highest Q^2 bins. Neither model can give an adequate description of the data in the region where $E_T^2 \gg Q^2$. Reasonable agreement is obtained when comparing the data to ARIADNE, with the exception of the low Q^2 or the high E_T^* regions where a poor description of the data is obtained.

4.10   A Study of the Photon Remnant

The k$_T$ algorithm used in $p\bar{p}$ mode assigns particles to a photon as well as to a proton remnant. The fraction of the incident photon's energy reconstructed in the remnant is given by

$$f = \frac{\Sigma E_i^*}{E_\gamma^*} \tag{4.21}$$

Here, the summation is over the energies of all particles assigned to the photon remnant by the k$_T$ algorithm and E_γ^* is the energy of the photon in the γ^*p frame calculated from the four-momenta of the incoming and scattered electron.

If the virtual photon interacts directly with the proton it will impart all of its momentum to the struck quark in the proton. If the virtual photon interacts
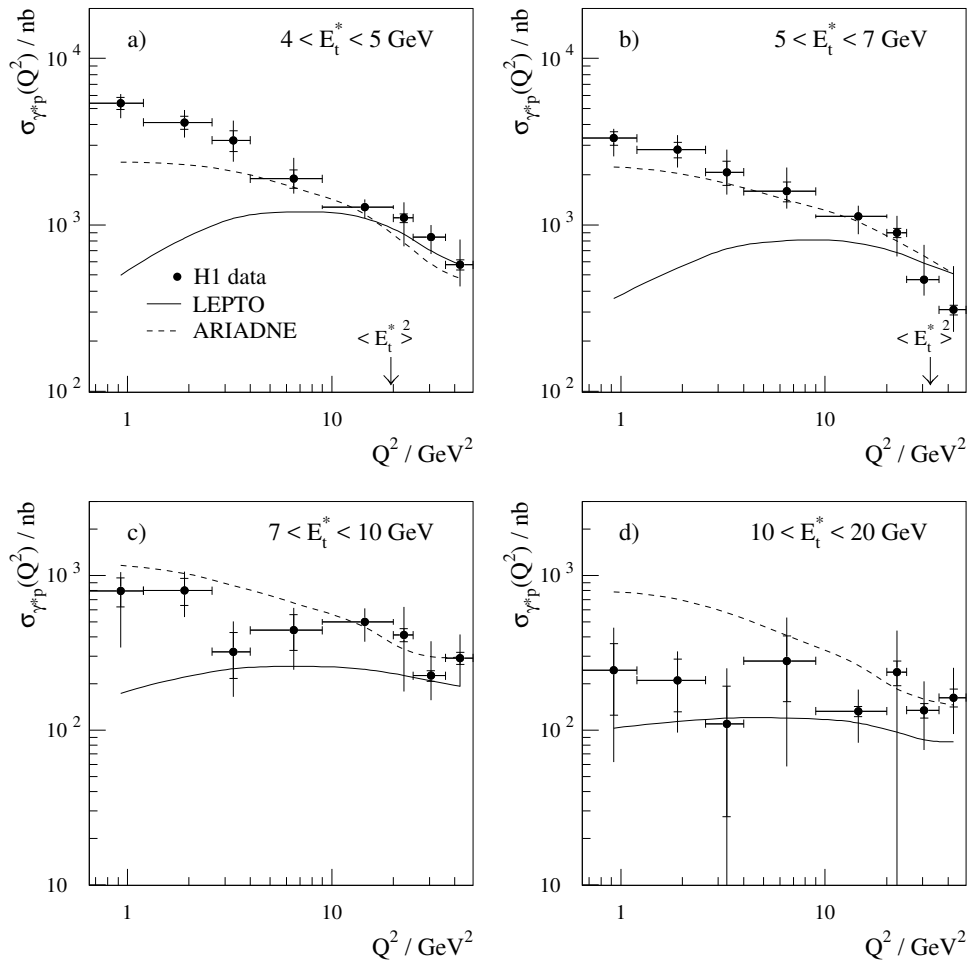
Figure 4.20: The inclusive γ^*p cross section $\sigma(Q^2)$. The inner error bars denote the statistical errors and the outer error bars the statistical and systematic errors added in quadrature. The data are compared to two different DIS models, LEPTO (solid line) and ARIADNE (dashed line).

as a resolved object, then the interacting parton from the photon will carry a fraction x_γ of the photon's momentum, leaving a remnant carrying the remaining momentum fraction, $(1-x_\gamma)$.

Figure 4.21 shows the uncorrected distribution of f as a function of Q^2 for events with at least one jet with $E_T^* > 5\,\mathrm{GeV}$. At $Q^2 = 0$, where resolved processes dominate, approximately half of the initial photon's momentum is reconstructed as a remnant jet. As Q^2 increases the distribution becomes more concentrated towards lower f values. In the highest Q^2 bin where the photon is expected to have no discernible structure and hence no remnant, f is concentrated at zero.

Two QCD based models, LEPTO and HERWIG DG, are also shown compared to the data. Both the Monte Carlo predictions are shown after the simulation of the effects of the H1 detector. The distribution from LEPTO (dashed line) is peaked at zero for all bins of Q^2 as expected from a Monte Carlo that incorporates only direct interactions. The distribution from HERWIG DG is peaked at 0.5 in the lowest Q^2 bin and shows an evolution to lower values of f as Q^2 increases, consistent with that of the measured data.

4.11   Conclusions

In this chapter the measurement of the single inclusive jet cross sections $\mathrm{d}\sigma_{ep}/\mathrm{d}\eta^*$ and $\mathrm{d}\sigma_{ep}/\mathrm{d}E_T^*$ has been described for events in the kinematic region $0.3 < y < 0.6$ and $0.65 < Q^2 < 50\,\mathrm{GeV}^2$ containing at least one jet with $E_T^* > 5\,\mathrm{GeV}$ in the region of pseudorapidity $-2.5 < \eta^* < -0.5$. The cross sections have been compared to DIS models in which the photon is treated as a point-like object and also to models where the photon is treated as having both point-like and partonic qualities.

In the region where $E_T^2 \gg Q^2$, models incorporating partonic structure to the virtual photon accurately describe the cross sections measured in this thesis, those without such structure do not.

The Q^2 evolution of the single inclusive jet cross sections has also been measured. This shows a rise of the jet cross sections at low Q^2 that is correctly predicted by models including a partonic structure of the virtual photon that is
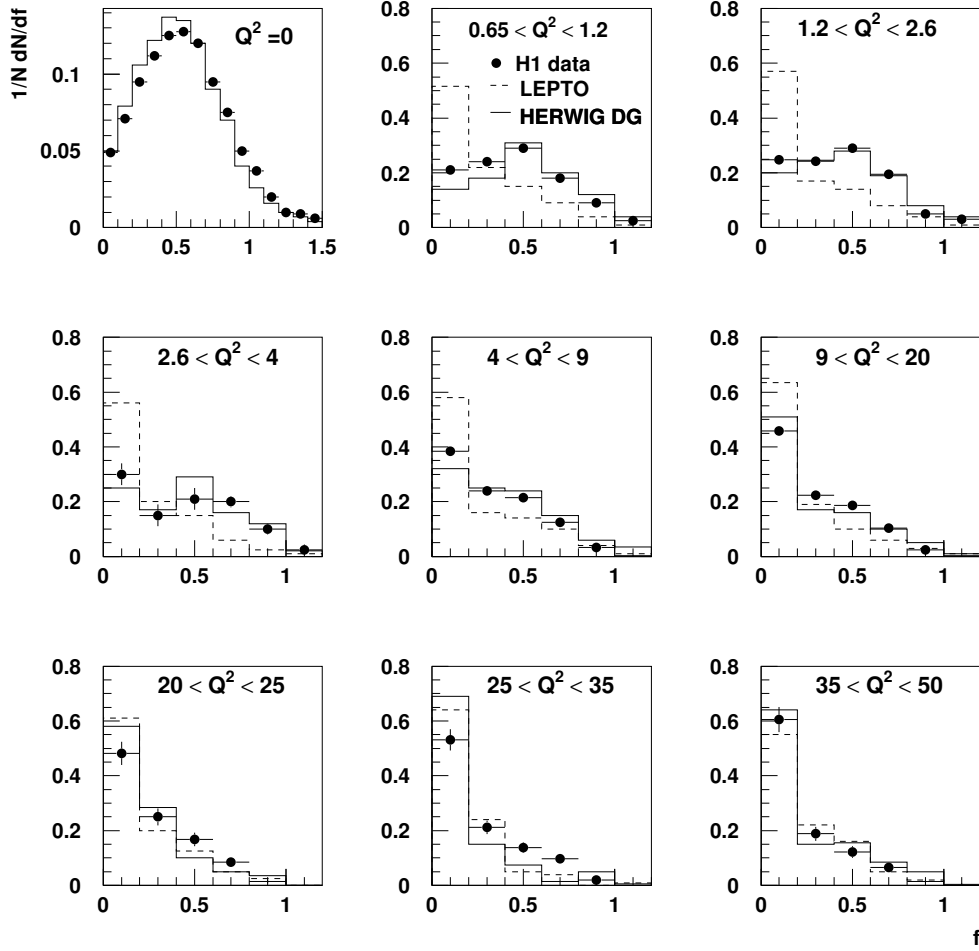
Figure 4.21: The uncorrected distribution of the observed fraction of the initial photon's momentum that is reconstructed as a remnant jet (f) for events containing at least one jet with $E_T^* > 5\,\mathrm{GeV}$ and $-2.5 < \eta_{jet}^* < -0.5$ The data are compared to the HERWIG DG model (solid line) and to LEPTO (dashed line) after detector simulation.

logarithmically suppressed with increasing Q^2 . The model that gives the best description of the data is RAPGAP, which uses the SaS-2D parameterisation of the structure of the photon.

Using the k$_T$ clustering algorithm, the fraction of the incident photon's energy reconstructed in the incident photon direction has been measured. In the region where $Q^2 > E_T^{*2}$ the fraction is peaked at zero, consistent with the picture of a point-like photon probing the structure of the proton. In the region $E_T^2 \gg Q^2$, however, the fraction is peaked at values greater than zero and supports the picture of a photon that includes a partonic component that is suppressed with Q^2.

Chapter 5

A Measurement of Inclusive Dijet Cross Sections

5.1 Introduction

With the increased luminosity of 1996 [1] it is possible to accurately measure the rate of events in which there are two high E_T^* jets present. Using the larger sample of data collected in 1996 also enables a measurement of jet production in a larger kinematic range than was possible with the 1995 shifted vertex data.

During the 1995 and 1996 data taking periods a study of the insert region of the SPACAL calorimeter (detailed in section 5.2) was performed to improve the precision of the electron position measurement down to lower distances from the beampipe. This meant that is was possible to measure jet cross sections down to Q^2 values of approximately $1.6\,\mathrm{GeV}^2$ using data taken at the nominal vertex position with good acceptance.

Using the data collected in 1996, the cross section $\mathrm{d}\sigma/\mathrm{d}\bar{\eta}^*$ is measured. Here, $\bar{\eta}^*$ is the average pseudo-rapidity of the two highest transverse energy jets in the interaction. The procedure for extracting the cross section and a discussion of the results is presented in section 5.3. This is followed by a measurement of the ratio $\sigma(res)/\sigma(dir)$, where $\sigma(res)$ is the cross section for interactions where the photon participates as a partonic object and $\sigma(dir)$ the cross section for direct interactions.

---

[1] HERA produced $8\,\mathrm{pb}^{-1}$ in 1996 of which H1 collected $6\,\mathrm{pb}^{-1}$.

5.2 Improvements to SPACAL Position Estimators

5.2.1 Improvements to the cluster radius estimator.

To reduce the background from non-DIS interactions, a cut is made on both the longitudinal and transverse cluster dimensions of the scattered electron candidate as detailed in section 4.4. A study of the existing estimators for the transverse dimensions and position is shown in this section as are improvements to these estimators.

The estimator of the transverse size of a cluster for the 1995 data sample was based on the linear weighted method. This uses an energy weighted sum of the distances R_i between the cluster barycentre and the cells belonging to the cluster.

$$R_{clus} = \sum_{N}^{i=1} R_i w_i \qquad w_i = \frac{E_i}{E_{clus}} \qquad (5.1)$$

Here, the summation is over all cells that contribute to the cluster. E_{clus} corresponds to the energy of the cluster, E_i to the energy of the clusters constituent cell i, and R_i to the distance of cell i from the cluster barycentre.

Using the estimator given in equation 5.1 results in a strong dependence of the cluster radius on the impact position of the scattered lepton. This dependence is shown in figure 5.1 (left) and arises because the transverse size of the electromagnetic shower caused by the incident lepton is smaller than the SPACAL cell size. Figure 5.1 (left) shows that the linear cluster radius estimator has maxima (minima) at 12, 16, 20 (10, 14, 18) cm. These positions correspond to the edge (centre) of the SPACAL cells. The linear estimator effectively measures the transverse cluster size to be that from the impact point of the scattered lepton to the centre of the cell containing the most energy.

An alternative method of estimating the transverse size of the cluster that suffers less from the problems outlined above involves making the cluster size larger than the cell size. This can be achieved by giving more weight to the lower energy components of the cluster by using a logarithmic weighting of cluster
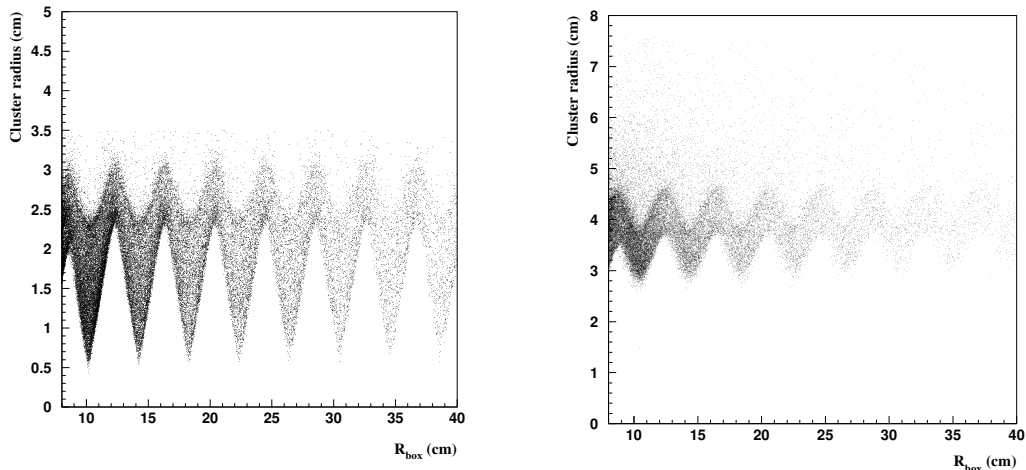
Figure 5.1: Linear (left) and logarithmic cluster radius estimators as a function of $R_{box} = \max(|x_{cl}|, |y_{cl}|)$, where x_{cl} and y_{cl} are the x and y positions of the cluster, respectively.

energies instead of the above linear weighting.

$$w_i = \frac{W_i}{\sum_{j=1}^{N} W_i} \qquad W_i = \max(0, w_{cut} + \ln \frac{E_i}{E_{clus}}) \qquad (5.2)$$

where E_{clus} corresponds to the energy of the cluster. The parameter w_{cut} acts as a minimum cell energy cut; larger values of w_{cut} result in lower energy cells being included in the clustering procedure thereby increasing the cluster radius. A w_{cut} of 4.95 was chosen for the data corresponding to a cut on cell energies of approximately 150 MeV, well above the noise level of 25 MeV for an individual SPACAL cell. Using a value for w_{cut} of 4.95 produces cluster radii larger than the SPACAL cell size without including cells containing excessive electronic noise.

Figure 5.1 (right) shows the logarithmic transverse cluster size estimator using the same data set as 5.1 (left). The effect of using the logarithmic approach is to increase the cluster radius and to reduce the dependence on the incident particles position within a cell. Tighter cuts can be placed on the cluster radius allowing better discrimination between hadronic and electromagnetic clusters. Figure 5.2 shows the cluster radius distributions for data (points), photoproduction background estimated using the PHOJET Monte Carlo (hatched histogram), and the sum of the photoproduction background and a DIS Monte Carlo (solid line). Using a logarithmic cluster radius estimator improves the signal to background discrimination compared to using a linear weighting of cell energies. Figure 5.2

shows that events with a cluster radius of above 6 cm arise almost exclusively from photoproduction background. A cluster transverse radius cut $R_{clus} < 6$ cm gives a high efficiency for selecting deep-inelastic scattering events with good background rejection.
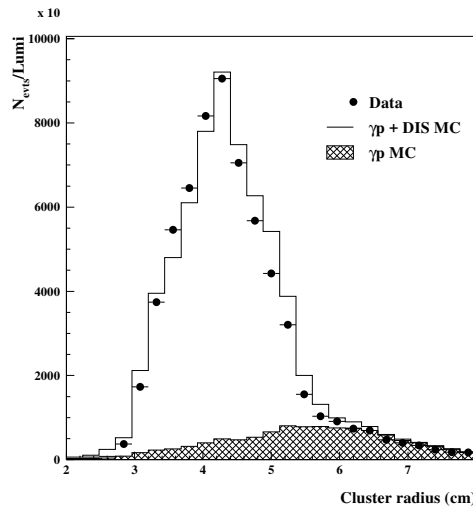
Figure 5.2: The cluster radius estimator using a logarithmic weighting of cell energies. The cluster radius distribution is shown for 1996 data (solid points) in the kinematic region $1.6 < Q^2 < 100\,\text{GeV}^2$ and $0.3 < y < 0.6$. A comparison is made to PHOJET (hatched histogram) and the sum of PHOJET and RAPGAP (solid line).

5.2.2   Study of the SPACAL Insert Region

In order to be able to measure down to low Q^2 values, the scattered lepton needs to be detected down to very small angles. Using shifted vertex data meant that low angles could be reached with good acceptance. Using nominal vertex data down to such low Q^2 values requires a study of the region close to the beampipe in order to ensure accurate reconstruction of the kinematics. The region of the SPACAL close to the beampipe is shown in figure 5.3.

The angular measurement of the scattered lepton is made using the BDC. The high track multiplicity present requires the SPACAL to reconstruct the electron impact point with as high a precision as possible. This impact point is then used by the BDC to avoid false tracks. Incorrect cluster position estimation results in

both incorrect cluster-track linking and in an increased track-cluster separation (a cut is placed at 2.5cm in the analysis) which will lead to a lowering of the efficiency of the SPACAL/BDC track linking requirement.

Shown in figure 5.4 (left) is the difference between the cluster radial position and the true radial position of the scattered lepton (as predicted by DJANGO 6.0) as a function of the radial distance from the beampipe. For distances less than 15 cm from the beampipe, the reconstructed cluster barycentre is systematically shifted outwards, the effect becoming more pronounced as the cluster is reconstructed closer to the beampipe.

With reference to figure 5.3, it can be seen that there are two contributions to the outward shift of the reconstructed cluster barycentre. Firstly, as the insert cells are smaller than the normal SPACAL cells, less energy is deposited in the cell thereby reducing the weight of the insert cells. Secondly the centres of the insert cells (shown as crosses in figure 5.3) are shifted outwards resulting in a further outward bias in the position measurement.

A solution for the first of these contributions is to rescale the energies of cells in the insert region by the reciprocal of the ratio of the cross-sectional areas of the insert cells compared to the standard cells. This compensates for leakage due to the reduced cell sizes in the insert region. The veto layers could also be used to add further information to the reconstruction but this has not been done as there is as yet no adequate simulation of the veto layers [32].

The second effect can be reduced by altering the coordinates of the insert cells to minimise $\Delta R = \sqrt{((x_{gen} - x_{clus})^2 + (y_{gen} - y_{clus})^2)}$. Adjusting the insert cell coordinates (shown as circles in figure 5.3) will only affect impact positions close to the beam pipe and so will not bias the estimate of the leptons impact position away from the central region of the SPACAL.

Figure 5.4 shows the difference between the reconstructed radial position of the incident lepton and the true position as given by DJANGO 6.0 for the standard H1 lepton finder before (left) and after (right) applying the above improvements. The effect of these is to improve the spatial accuracy of the cluster barycentre reconstruction in the SPACAL region close to the beampipe. This region corresponds to small Q^2 . The same effect is observed in data. Shown in figure 5.5 is the same plot as in figure 5.4 but replacing the Monte Carlo radial position

with the extrapolated BDC impact position. The discrepancy is still noticeable but is reduced as the correct BDC track depends on the cluster barycentre. The improvement using the new reconstruction method can still clearly be seen.

5.3 Event Selection

The procedure used to select the DIS events used in the di-jet analysis is similar to that descibed in the previous chapter. Therefore, only the differences are outlined below.

5.3.1 Trigger Selection

Due to the increased luminosity of 1996 and the higher rate of collisions, more stringent requirements need to be imposed at the level 1 triggering stage. For the di-jet analysis, events are selected by the S2 trigger. The S2 trigger requires the presence of an electromagnetic cluster exceeding a threshold energy in the SPACAL, in conjunction with a track in the central tracker with transverse momentum greater than 800 MeV. Because of the larger background at small distances from the beampipe the SPACAL energy threshold of 2.5 GeV at large radii is raised to 5.7 GeV for clusters with centres of gravity less than 12 cm from the centre of the beampipe. The event also has to have a well defined interaction vertex and timing consistent with it being due to an ep collision. The efficiency of this trigger for selecting dijet events is shown in figure 5.6 as a function of the kinematic variables used in the analysis of $d\sigma/d\bar{\eta}^*$. These variables are defined in section 5.4. The S2 efficiency is high for all the Q^2 bins presented in this chapter. The main source of inefficiency arises from the z_{vertex} requirement. The lower efficiency towards higher $\bar{\eta}^*$ values can be explained by the fact that the efficiency for reconstructing tracks is lower in that region.

To further increase the purity of the DIS sample the same cuts are applied as for the 1995 data with the following alterations.

- The scattered electron must deposit an energy of more than 8 GeV in the calorimeter. This allows an increase in the y and Q^2 range used for the analysis.
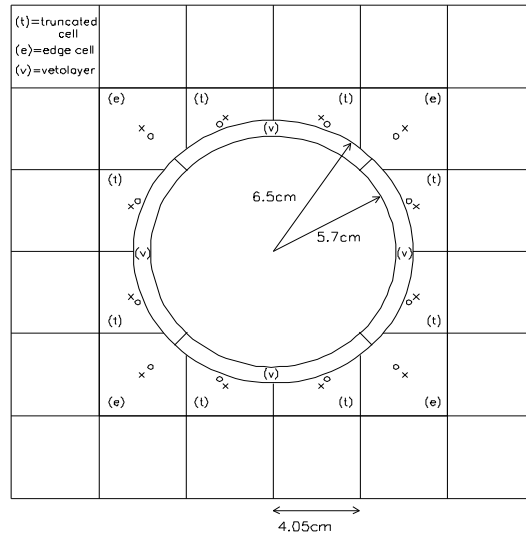
Figure 5.3: The insert region of the SPACAL in the $x - y$ plane.
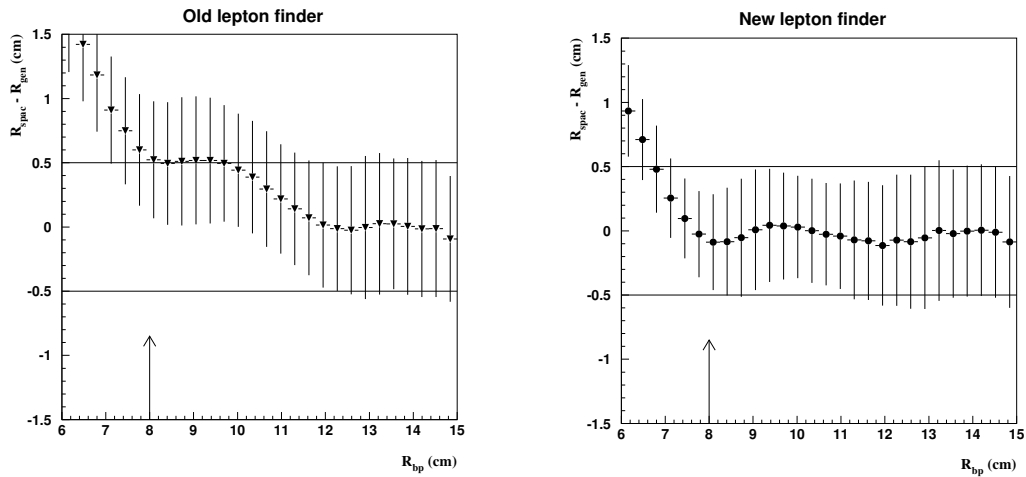
Figure 5.4: Old (left) and new (right) position estimator accuracy as given by DJANGO 6.0, plotted against the radial distance from the centre of the beampipe. At small radii where energy deposits in the insert region of the SPACAL become important there is a systematic outward shift in the reconstructed position. This effect is reduced when including the improvements to the insert region outlined in the text. The arrow represents the position of the radial cut used in the dijet analysis.
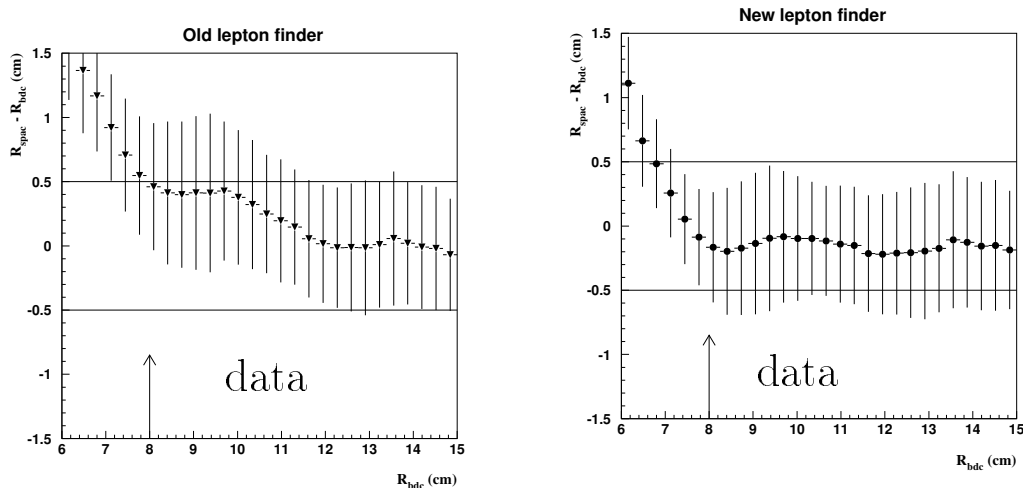
Figure 5.5: Difference between the radial position given by the cluster barycentre and that given by the BDC, plotted as a function of the distance from the beampipe as estimated from the BDC for the old (left) and new (right) lepton finder. The arrow marks the radial cut used in the analysis of the dijet data.

- The scattered electron cluster barycentre must lie further than 8 cm from the centre of the beampipe. This is lower than the cut used in the previous chapter due to the improvement of the electron position estimator detailed in section 5.2.

- The transverse radius of the SPACAL cluster, calculated using the logarithmic weighting of cell energies described in section 5.2.2, is required to be less than 6 cm.

As no comparison is made with photoproduction data the main constraints on the y range are the resolution of the H1 detector and the photoproduction background that will occur at high y. The following kinematic range is selected for analysis :-

- $0.1 < y_e < 0.7$

- $1.6 < Q_e^2 < 100 \, \mathrm{GeV}^2$
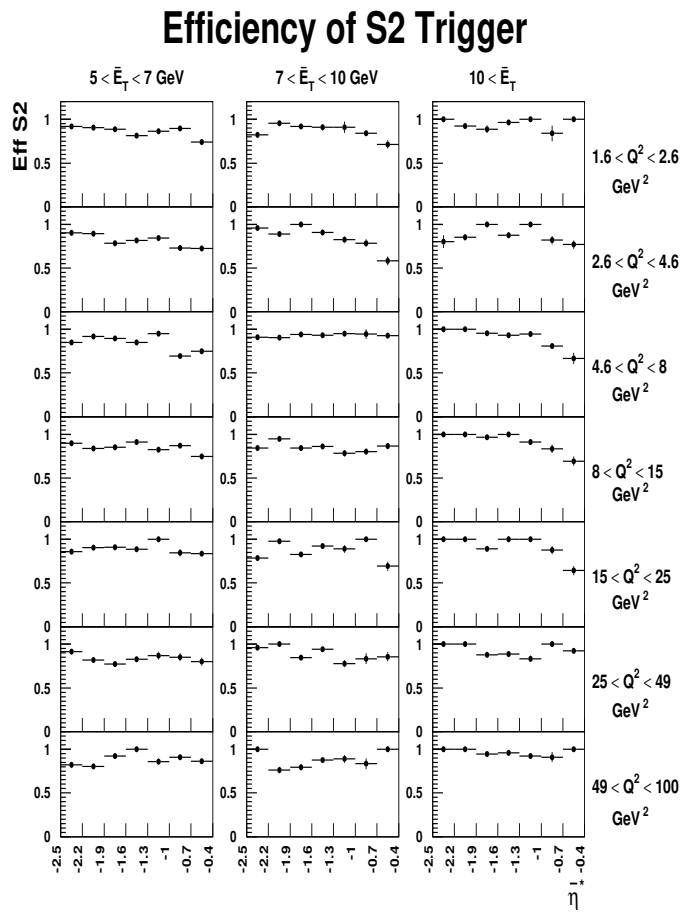
Figure 5.6: Efficiency of the S2 trigger used to select dijet DIS events as a function of the virtuality of the photon, the average transverse energy and average psuedo-rapidity of the two highest E_T^* jets.

5.3.2   Jet Selection

Jets are selected using the longitudinally invariant version of the k_T algorithm described in section 2.5. An analysis by Spiekermann presented in [51] showed that performing clustering over both calorimeter clusters and tracks, with each track contributing a defined maximum transverse energy, reduced the dependence of the jet finding efficiency on pseudo-rapidity and compensated for energy losses due to dead material. For the remainder of this thesis jet finding is performed using both calorimeter clusters and tracks, with each track contributing a maximum transverse energy (in the lab) of 350 MeV. 350 MeV is the cutoff which results in the best description of energy flows, such as $\Sigma E - P_z$.

Figure 5.7 shows the Monte Carlo Correction factors obtained with and without including tracking information in the jet clustering procedure. Also shown on the right of the plot (figure 5.8) is the corrected jet cross section $d\sigma/d\bar{\eta}^*$ obtained using a subset of 1996 data with and without tracking information included in the jet finding. The correction factors are dramatically reduced, as is their dependence on $\bar{\eta}^*$, when tracking information is included. This is a result of the increased efficiency of selecting jets above a certain E_T^* threshold when using tracks. Including tracking information does not significantly change the values of the final physics cross section measurements. However, reducing the dependence of the correction factors on both the transverse energy of the jet and the jet pseudo-rapidity allows the error due to the LAr calorimeter energy scale uncertainty to be reduced.

In leading order QCD, high E_T^* jets should be produced with equal but opposite E_T^*. Requiring that the difference in E_T^* between the two highest E_T^* jets divided by the sum of the E_T^* be less than 0.25 reduces the probability of a jet originating from a source other than the hard scattering such as the proton/photon remnant. The requirement that the transverse energies of the jets are approximately balanced also limits the probability for hard final state QCD radiation. This enables accurate comparisons between the MC predictions, which are all calculated in leading order, and the data. The average transverse energy of the two highest E_T^* jets, $\bar{E}_T^*$, is required to be greater than 5 GeV. This limits the measurement to a kinematic region where pQCD is accurate.
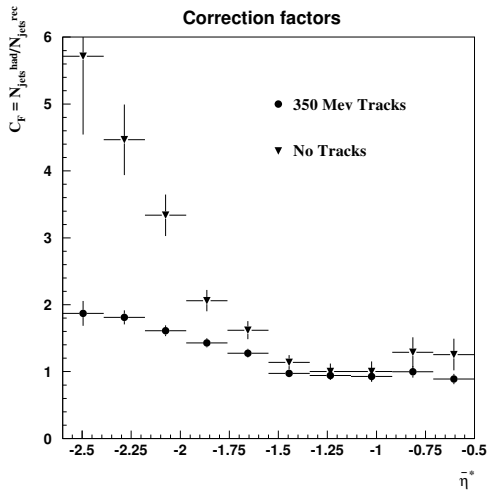
Figure 5.7: Correction factors shown as a function of the average jet pseudo-rapidity $\bar{\eta}^*$ determined using HERWIG with calorimeter information only (triangles) and with tracking information included (solid circles).
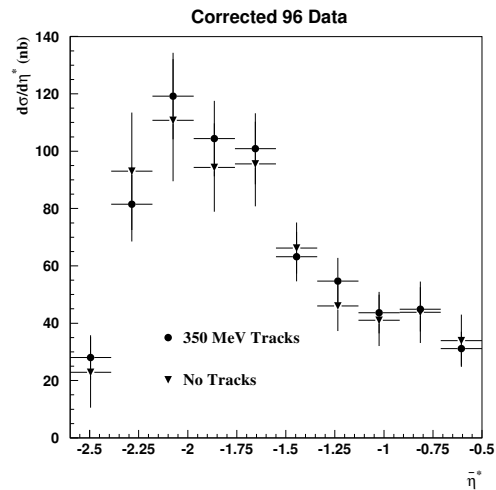
Figure 5.8: The jet $\bar{\eta}^*$ distribution corrected for detector effects using HERWIG with (solid points) and without (triangles) tracking information included in the jet finding.

These cuts are summarised in:

$$\frac{E_{T_1} + E_{T_2}}{2} > 5\,\text{GeV} \tag{5.3}$$

$$\frac{E_{T_1} - E_{T_2}}{E_{T_1} + E_{T_2}} < 0.25 \tag{5.4}$$

To ensure the jets are well within the detector acceptance they must satisfy the following requirements:-

$$-2.5 < \bar{\eta}^*_{jet} < -0.4 \tag{5.5}$$

$$|\Delta \eta_{jets}| < 1.0 \tag{5.6}$$

In leading order the high E^*_T jets should be produced back to back in ϕ. False jets will tend to be distributed randomly in ϕ. Requiring the jets to be back to back in ϕ therefore suppresses dijet events in which one of the jets was not from the hard scattering process.

$$|\Delta \phi_{jets}| > 150° \tag{5.7}$$

These cuts do not constrain the transverse energies of both jets to be the same thus avoiding the infrared sensitive region $E_T^1 = E_T^2$ where next to leading order perturbative QCD is not predictive [52].

Remaining photoproduction background was evaluated using PHOJET. The MC sample used corresponds to an integrated luminosity of 519.2 nb^{-1}. From this sample no events survived the DIS, kinematic and jet cuts and the photoproduction background is therefore estimated to be negligible.

5.4   Inclusive $\mathrm{d}\sigma/\mathrm{d}\bar{\eta}^*$ Dijet Cross Section

This section describes the measurement of the dijet cross-section $\mathrm{d}\sigma/\mathrm{d}\bar{\eta}^*$. This variable was chosen because it is sensitive to the parton distributions in the proton and photon. In order to limit the dependence of the cross-section to the parton content of the proton and photon the following restrictions are imposed.

When the difference between the pseudo-rapidities of the two highest E_T^* jets ($|\Delta\eta|$) is limited to $|\Delta\eta| < 1.0$, θ^*, the angle between the jet-jet axis and the beam axis is constrained to be close to 90°. This limits the variation of the cross section with $\cos\theta^*$. Therefore, the shape of the $\bar{\eta}^*$ distribution results mainly from the parton content of the photon and proton and is not due to the matrix element variation. Applying the cut $|\Delta\eta| < 1$ also reduces the number of dijet events in which the proton/photon remnant has been misidentified as a jet whilst also ensuring jets are well contained in the detector for the measured $\bar{\eta}^*$ bins.

The fraction of the photon's momentum involved in the interaction, x_γ, can be reconstructed using the two highest E_T^* jets as shown in equation 5.8.

$$x_\gamma^{rec} = \frac{\displaystyle\sum_{jet\ 1,2} E_T^{1,2} e^{-\eta_{1,2}^*}}{\sum_i (E - p_z)} \tag{5.8}$$

Here the summation in the denominator is over all particles in the event excluding the scattered lepton. Rewriting equation 5.8 in terms of $\Delta\eta$ and $\bar{\eta}^*$, and using the fact that the two jets have approximately equal transverse energies, we have:-

$$x_\gamma^{rec} = \frac{2\bar{E}_T^*}{\sum_i (E - P_z)} e^{-\bar{\eta}^*} \cosh\frac{\Delta\eta}{2}. \tag{5.9}$$

Model name	α_s	Proton PDF	γ^* PDF	P_T^{min} (GeV)
HERWIG(HO)/DG (×1.7)	2-loop	GRV-HO	GRV-HO*DG ($\omega = 0.2\,\text{GeV}$)	3
RAPGAP(HO)/SAS-2D	1-loop	GRV-HO	SAS-2D	3

Table 5.1: A Summary of the parameters of the two Monte Carlo models used to correct the di-jet data.

When the cut $|\Delta\eta| < 1.0$ is imposed $\cosh(\Delta\eta^*) \to 1$ (for the maximum allowed). Equation 5.9 can then be approximated by :-

$$x_\gamma^{rec} = \frac{E_T^{jet^*} e^{-\bar{\eta}^*}}{\sum_i (E - P_z)} \qquad (5.10)$$

The distribution of $\bar{\eta}^*$ can be seen to be directly related to the x_γ distribution. The variable $\bar{\eta}^*$ was chosen as the variable to measure as it can be accurately reconstructed whilst being sensitive to the underlying parton dynamics. In Figure 5.4.1 the resolutions of Q^2 , $\bar{\eta}^*$, $\bar{E}_T^*$ and $|\eta_1 - \eta_2|$ obtained using RAPGAP are shown. The χ^2 values of the fit to the resolutions are large but the fits give a good qualitative description of the resolutions shown. Figure 5.4.1 shows the resolutions given by the fit are all less than half the size of the bin widths chosen for this analysis for the relevant variables. The bin widths chosen for this analysis are all greater than twice the resolution in the relevant kinematic variable.

Both HERWIG and RAPGAP are used to correct the data. HERWIG uses the DG parameterisation to model the resolved photon contribution. The luminosity of the HERWIG sample used here corresponds to twice that of the data sample. RAPGAP was generated using the SaS2D parton densities for the virtual photon and corresponds to approximately three times the luminosity of the data. Both simulations use the GRV-HO parton densities [15] for the proton. The comparison of the HERWIG and RAPGAP predictions with the observed data is shown in figure 5.4.1. The properties of the two Monte Carlo simulations used to correct the data are summarised in table 5.4.

5.4.1 Acceptance Correction of Data

The data are corrected for detector effects using the same bin-by-bin correction procedure as used for the single inclusive data. RAPGAP, which gives the best description of the uncorrected data, was used to correct the data. As is shown later, the SaS2D parton densities for the photon, as implemented in the RAPGAP program, underestimate the resolved component. It was therefore necessary to reweight the mixture of direct and resolved processes to obtain a good description of the observed distributions. The simulated HERWIG files used to estimate model dependence were generated with NLO α_s. Because HERWIG calculates the cross sections in LO α_s, using NLO α_s results in a lower cross section prediction. To improve the description of the data the prediction from HERWIG is multiplied by a factor of 1.7 .

Shown in figure 5.4.1 is the observed jet $d\sigma/d\bar{\eta}^*$ plotted as a function of Q^2, $\bar{E}_T^*$ and $\bar{\eta}^*$. The data are compared to two MC models that include a simulation of the effects of the H1 detector. The two MC models are in reasonable agreement with the data. HERWIG overestimates the cross section in the lowest $\bar{E}_T^*$ region in the highest three Q^2 bins. In these bins however RAPGAP produces a good description of the observed distributions. To investigate the bin migrations the resolutions of the Q^2, $\bar{\eta}^*$, $\bar{E}_T^*$ and $\Delta\eta$ are shown in figure 5.4.1 along with the results of a Gaussian fit to the distributions. The resolutions of the variables are all smaller than the bin widths used to present the $d\sigma/d\bar{\eta}^*$ cross-section measurement with the possible exception of the $\bar{E}_T^*$ variable. The purity of the bins used to measure the cross-section was calculated using HERWIG and RAPGAP. The resulting purities are above 40% in most of the selected bins and are always greater than 30%.

The correction factors obtained from RAPGAP and HERWIG are shown in figure 5.11. Both Monte Carlos give very similar correction factors apart from the high Q^2 bins and the high $\bar{E}_T^*$ bin where in the lowest $\bar{\eta}^*$ bin the correction factors are different by up to a factor of two.
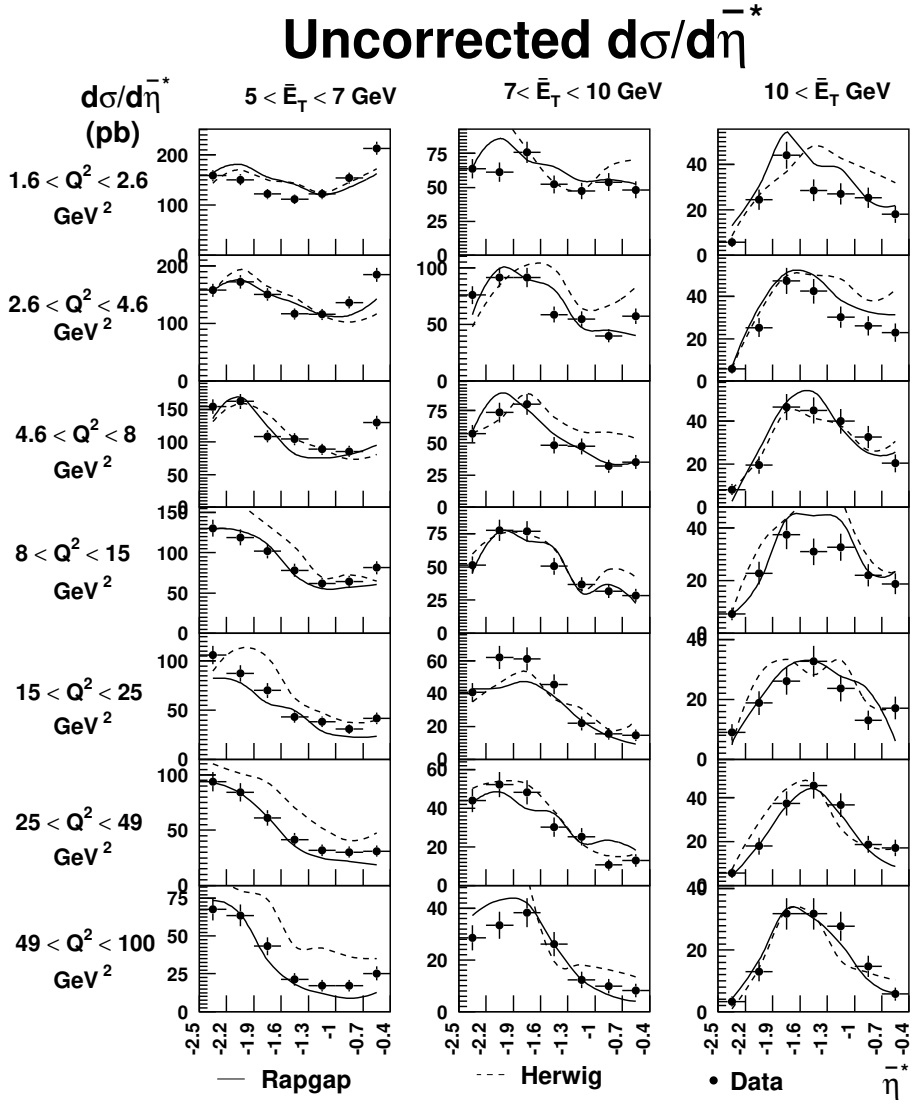
Uncorrected dσ/dη̄*

Figure 5.9: The uncorrected jet $\bar{\eta}^*$ distribution for different regions of Q^2 and $\bar{E}_T^*$ compared to predictions from RAPGAP (solid line) and HERWIG (dashed line). Both Monte Carlos have been passed through a full simulation of the H1 detector.
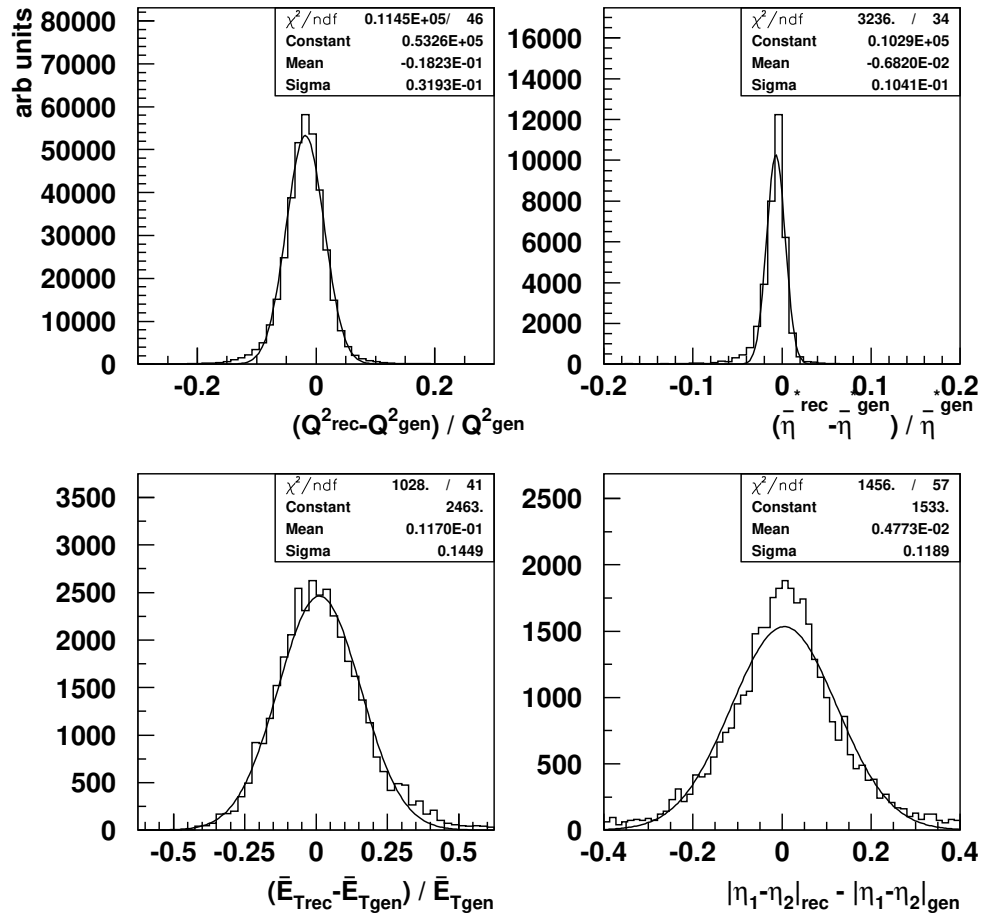
Figure 5.10: The resolution for variables used in the determination of $d\sigma/d\bar{\eta}^*$ predicted by HERWIG5.9 after good event cuts have been applied. Shown in the top left and right are the Q^2 and $\bar{\eta}^*$ resolutions, respectively. The $\bar{E}_T^*$ and $|\eta_1 - \eta_2|$ resolutions are shown in the lower left and right plots. The results of a Gaussian fit are shown in the corner of each plot.
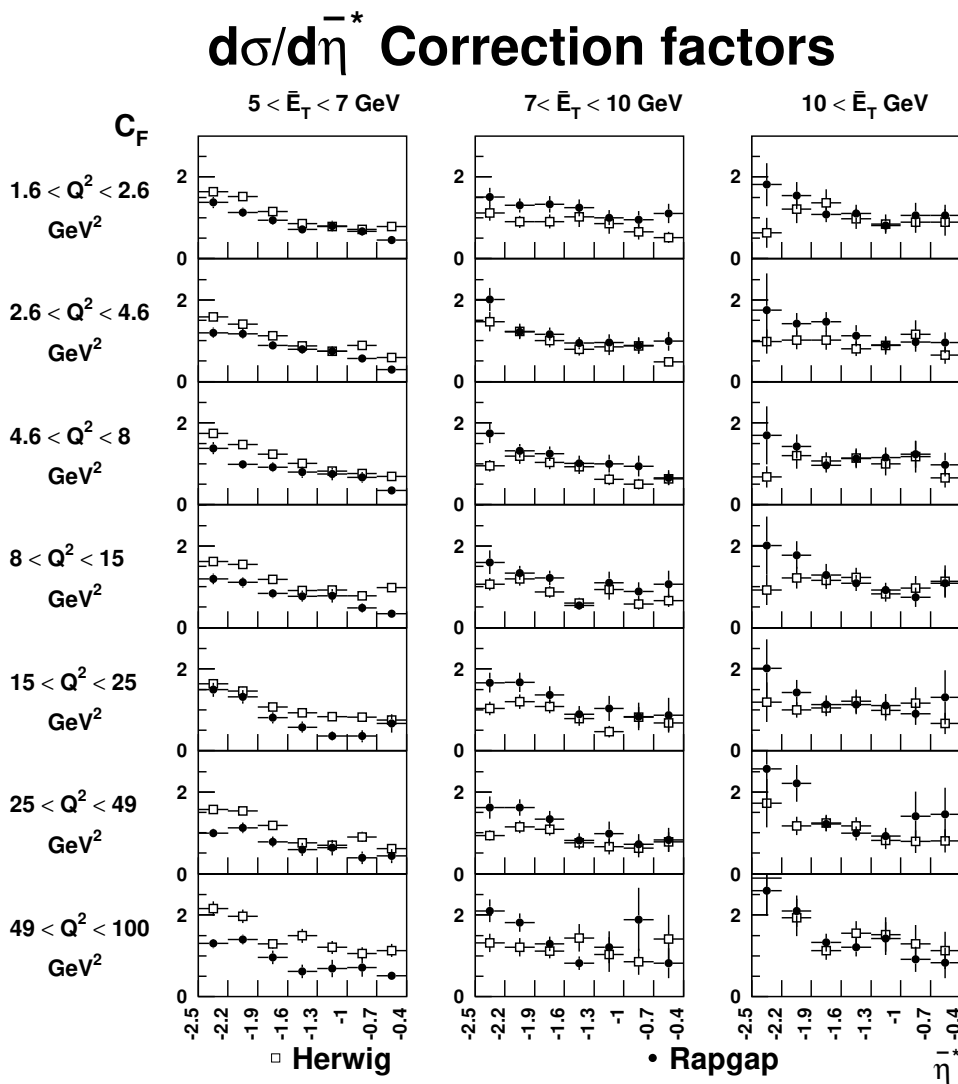
Figure 5.11: Correction Factors as a function of η^* obtained from RAPGAP (closed points) and HERWIG (open squares) for different regions of Q^2 and $\bar{E}_T^*$

5.4.2 Systematic Uncertainties

In addition to the systematic uncertainties considered for the single inclusive jet cross sections, a number of further studies are performed.

- To check the dependence of the cross section on the minimum parton transverse momentum cut-off (P_T^{min}) in the Monte Carlo, P_T^{min} was raised from 2.0 GeV to 2.5 GeV. This resulted in a negligible change to both the predicted cross section and the correction factors.

- The systematic uncertainty due to the statistical uncertainty (σ_ε) in the trigger efficiency determination, shown in figure 5.6, was evaluated by taking the largest difference between the results obtained with ε_{trig} and the results corrected with either $\varepsilon_{trig} + \sigma_\varepsilon$ or $\varepsilon_{trig} - \sigma_\varepsilon$.

The largest source of systematic uncertainty arises from the model dependence of the correction procedure. To evaluate this effect, the data is corrected using both RAPGAP and HERWIG which include different parton showering mechanisms. The differences between the two corrected measurements is then assigned as a systematic error. The LAr energy scale uncertainty proved to be the second largest source of systematic error. Including the effects of initial and final state radiation resulted in a change in the cross section which was typically less than 7%. The data are not corrected for these effects, which have been included in the systematic error.

The corrected differential cross-section $d\sigma/d\bar{\eta}^*$ is shown in figure 5.12 in the kinematic region $1.6 < Q^2 < 100\,\mathrm{GeV}^2$ and $0.1 < y < 0.7$ for events containing two high E_T^* jets. The data are also compared to RAPGAP with the SaS2D paramaterisation of virtual photon structure and RAPGAP DIRECT, which treats the photon as a purely pointlike object. The data shows a tendency to have a flatter $\bar{\eta}^*$ dependence for the lower Q^2 bins presented. This is expected if all of the photon's momentum does not enter into the collision as the jets would then be boosted in the positive $\bar{\eta}^*$ direction. The highest $\bar{E}_T^*$ bin does not exhibit this behaviour as it is dominated by direct interactions. This is due to the probability of resolved interactions having the enegy required to produce high E_T^* jets is smaller than for direct interactions.
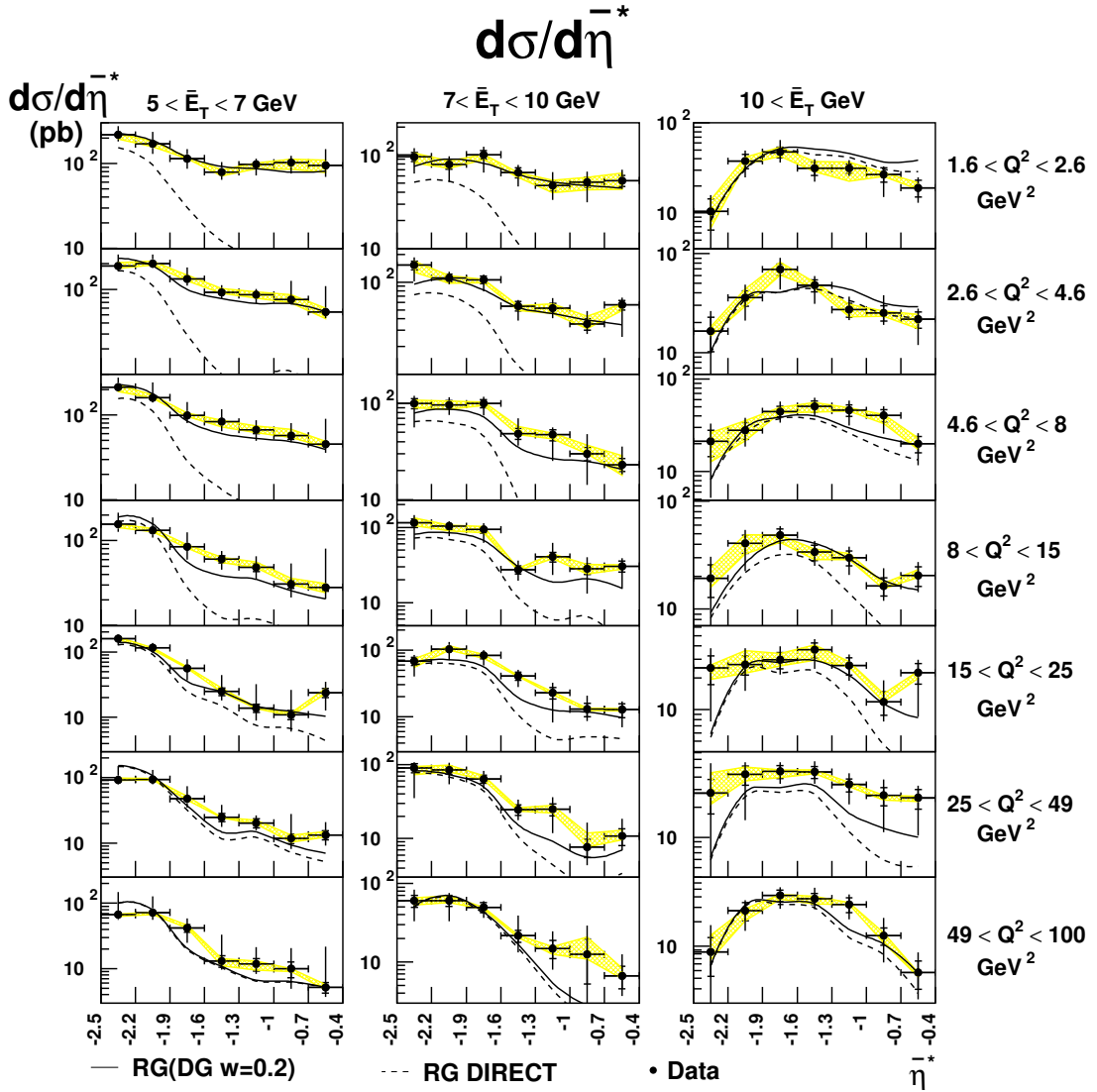
Figure 5.12: The corrected differential cross section $\mathrm{d}\sigma/\mathrm{d}\bar{\eta}^*$ for high E_T^* dijet events in the kinematic range $1.6 < Q^2 < 100\,\mathrm{GeV}^2$ and $0.1 < y < 0.7$. The data are compared to RAPGAP with the Drees-Godbole parameterisation of virtual photon structure (solid line) and the direct only contribution to this model (dashed line). The shaded curve represents the 4% uncertainty of the Liquid Argon hadronic calorimeter energy scale.

Figure 5.12 shows quite clearly that a model that treats the photon as a purely pointlike object cannot describe the measured H1 data in the low Q^2, low E_T^* bins. Shown in figure 5.13 are the same data compared to the predictions of RAPGAP using three different input virtual photon PDFs. It can be seen that all three give a more accurate description of the data than the direct only model shown in figure 5.12.
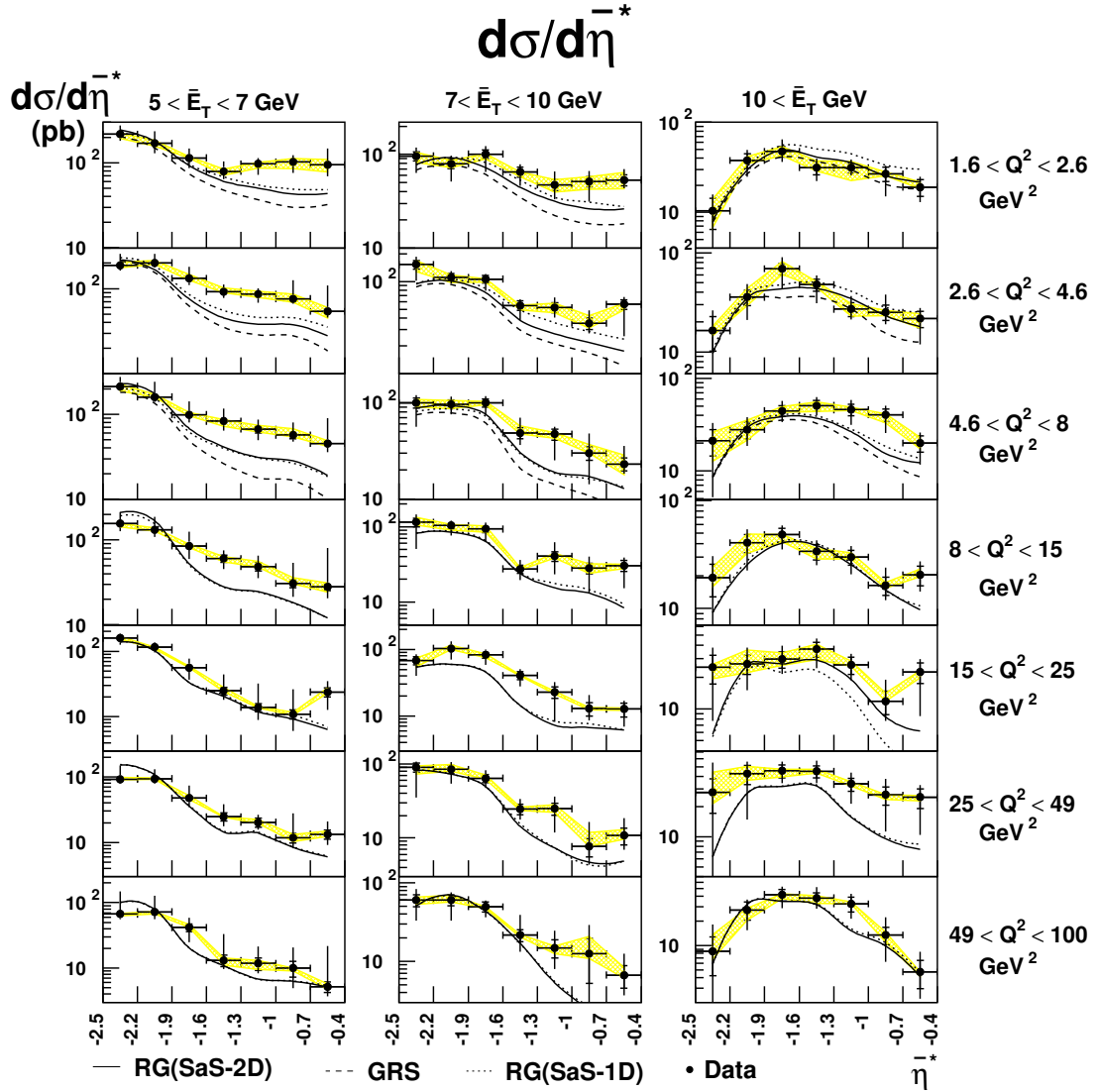
Figure 5.13: The corrected differential cross section $d\sigma/d\bar{\eta}^*$ for high E_T^* dijet events in the kinematic range $1.6 < Q^2 < 100\,\text{GeV}^2$ and $0.1 < y < 0.7$. The predictions from RAPGAP using the SaS1D (dotted curve), SaS2D (solid line) and GRS (dashed curve) parameterisations of photon structure are also overlayed. The shaded curve represents the 4% uncertainty of the LAr hadronic calorimeter energy scale.

The predictions from the SaS models underestimate the data in the low Q^2 region whilst the predictions from Drees-Godbole, with $\omega = 0.2$, give a good description of the data. The better description of the data by the Drees-Godbole model is not surprising since the normalisation can be tuned by adjusting ω.

5.5   Resolved/Direct(Q^2) Ratio

The measurement of the ratio of resolved to direct events is discussed in this section. Studying this ratio as a function of Q^2 and E_T^* illustrates several features of the evolution of the structure of the photon with Q^2. With two jets in the event it is possible to cleanly reconstruct the variable x_γ . The estimate of x_γ (x_γ^{rec}) was made using the sum of the energies minus the longitudinal momenta of the two highest p_T jets and particles in the event. This estimate of x_γ is prefered to that in formula 5.8 because the uncertainties in the energy scale of the LAr calorimeter are expected cancel partially using this method.

$$x_\gamma^{rec} = \frac{\displaystyle\sum_{jet\,1,2} (E^{1,2} - p_z^{1,2})}{\displaystyle\sum_{h}(E^h - p_z^h)} . \tag{5.11}$$

Here, the lower summation is over all the hadrons resulting from the interaction.

If the photon interacts purely as a pointlike object then all of its momentum will enter the hard scattering process and $x_\gamma = 1$. Due to higher order effects and detector resolution however, x_γ is smeared so that it forms a distribution that does not necessarily peak at $x_\gamma = 1$. This is illustrated in fig 5.14. The direct and resolved contributions to the x_γ distribution is plotted together with the sum of direct and resolved.

An operational definition of a direct interaction is defined as $x_\gamma > 0.7$. Resolved interactions are defined as $x_\gamma < 0.7$. This differs from the usual threshold of 0.75 commonly employed in photoproduction [48]. The value of 0.7 was chosen as the threshold to increase the purity of the resolved bin. In photoproduction the resolved contribution is dominant whereas in the sample of data analysed here the direct contribution is largest. Therefore a lower x_γ cut was required to reduce the migrations of direct events across the x_γ cut. Using this definition of
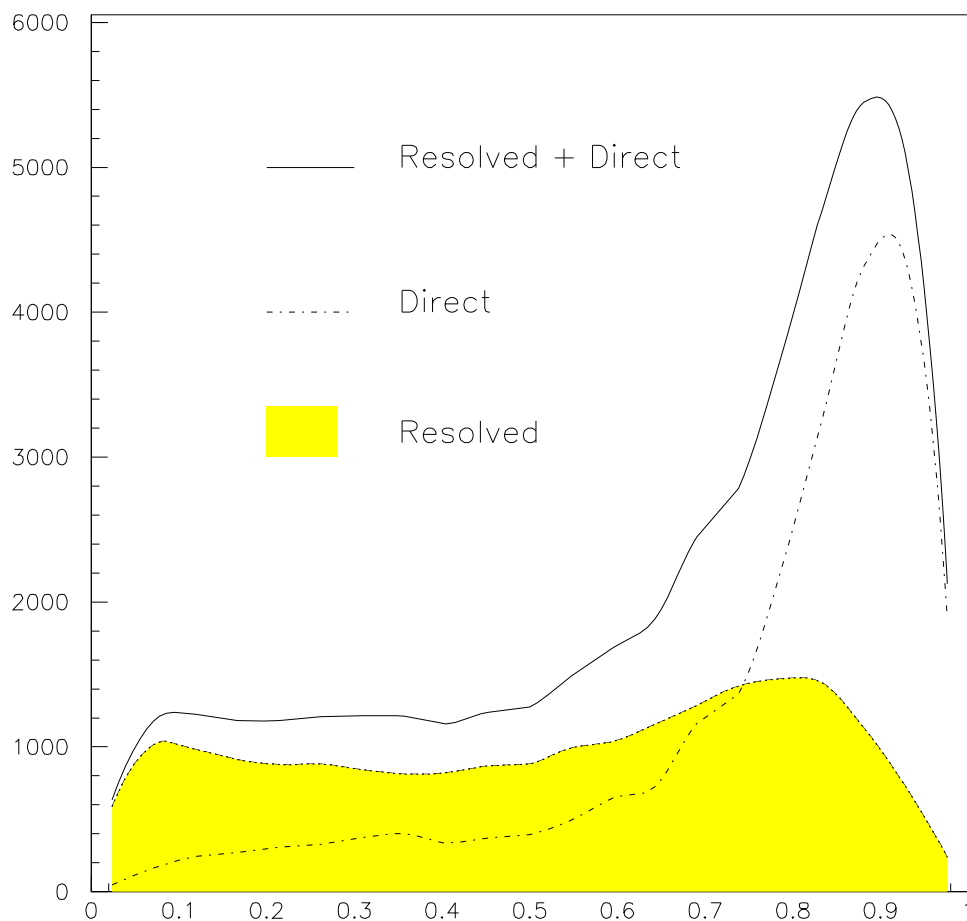
Figure 5.14: The x_γ distribution, estimated using the two highest E_T^* jets in RAPGAP Monte Carlo events before detector simulation.

direct and resolved, the ratio

$$R = \frac{Resolved}{Direct} = \frac{N_{res}}{N_{dir}} \qquad (5.12)$$

is calculated, where N_{res} is the number of events with $x_\gamma < 0.7$ and N_{dir} is the number of events with $x_\gamma > 0.7$.

Shown in figure 5.5 is the observed x_γ distribution plotted as a function of the average transverse energy of the two highest E_T jets in the interaction. Also shown are the predictions of the HERWIG and RAPGAP Monte Carlos. Both Monte Carlos have passed through a simulation of the H1 detector. The Monte Carlos give a good description of the data in all regions of average transverse jet energy except in the region where $5 < \bar{E}_T^* < 7$ GeV. In this region the data lies between the two Monte Carlo predictions. It can be seen that as the average transverse energy of the jets increases the x_γ distribution becomes peaked at 1. This is due to a kinematic effect of resolved events having a reduced energy compared to direct events. This suppresses jet production at large E_T^* for resolved events.

The same systematic uncertainties were considered here, as for the $d\sigma/d\bar{\eta}^*$ cross section measurement. The dominant contribution to the systematic uncertainty arises from the Liquid argon calorimeter energy scale uncertainty of 4%.

Shown in figure 5.5 is the correction factors obtained from HERWIG and RAPGAP. The correction factors are remarkably consistent

Figure 5.17 shows the measured values of $R = \sigma(res)/\sigma(dir)$ in the kinematic region $0.1 < y < 0.7$ and $1.6 < Q^2 < 100\,\mathrm{GeV}^2$ for jets with average psuedo-rapidities in the region $-0.4 < \bar{\eta}^* < -2.5$. The ratio is presented in three bins of $\bar{E}_T^*$, where $\bar{E}_T^*$ is the average transverse energy of the two highest E_T^* jets in the event. The data are shown as solid points with the statistical and systematic errors added in quadrature. A comparison is made with the predictions from RAPGAP with three different choices for the virtual photon parton densities. The prediction with no Q^2 suppression of the photon parton densities ($\omega = 999$) divided by a factor of two is shown as the dashed line. The direct only contribution is shown as the solid curve and the predictions obtained using the DG PDFs with two different settings of ω are shown as the dotted ($\omega = 0.1$) and dash-dotted curves ($\omega = 0.2$) respectively. The data disfavour the two extreme models of a photon having structure at all Q^2 and E_T^{*2}, and
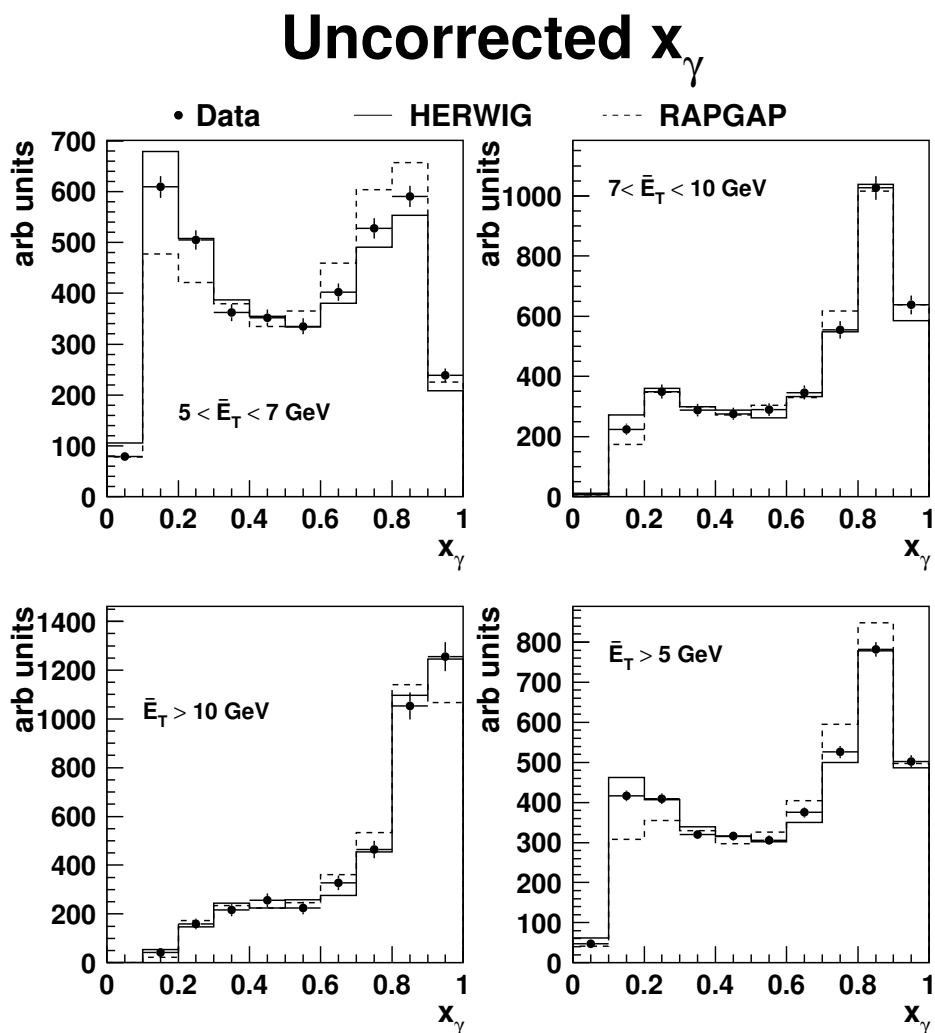
Figure 5.15: The x_γ distribution, estimated using the two highest E_T^* jets in the interaction for data events passing the jet and kinematic cuts outlined in 5.3. The predictions from RAPGAP and HERWIG after detector simulation are shown as the full and dashed curves respectively.
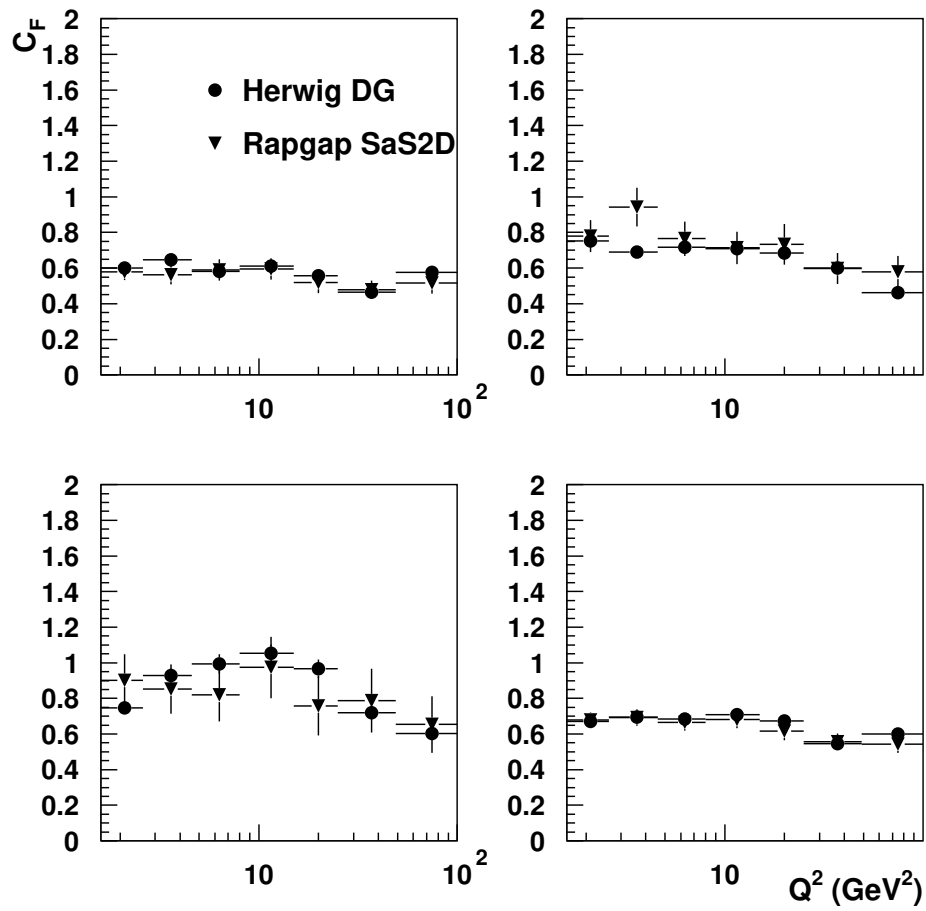
Figure 5.16: The Correction factors for the ratio $R = \sigma(res)/\sigma(dir)$ distribution as a function of Q^2 compared to HERWIG (circles) and RAPGAP (triangles).
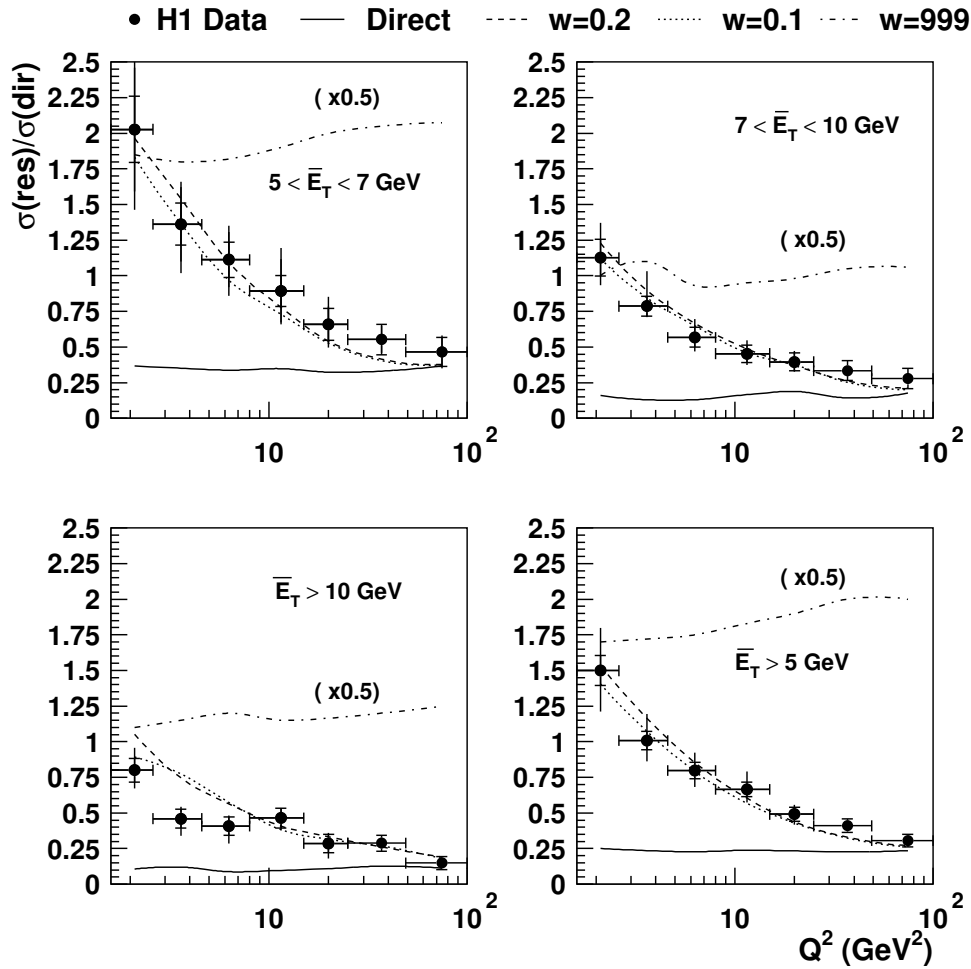
Figure 5.17: The measured ratio $\sigma(res)/\sigma(dir)$ as a function of Q^2 shown in three different $\bar{E}_T^*$ bins. The data are compared to the predictions from RAPGAP using the DG model with $\omega = 0.1$ and 0.2 as shown in the dotted and dashed curves respectively. The full curve represents the prediction using only the direct contribution. The dot-dashed curve shows the ratio multiplied by a factor $\frac{1}{2}$ when there is no Q^2 suppression of the real photon PDFs

having no structure independent of Q^2. The ratios measured are consistent with a logarithmic suppression of the photon structure as a function of Q^2 , in agreement with both the single inclusive jet cross sections measured in chapter 4 and the dijet cross section $d\sigma/d\bar{\eta}^*$ presented in section 5.4.

The measured ratios are also compared to other QCD based predictions of how the structure of the photon evolves with its virtuality in figure 5.18. Within the measurement errors the data cannot differentiate between the various models of the Q^2 evolution of the photon structure. The only model that systematically underestimates the data is that of GRS. This underestimation arises from the requirement that the probing scale must be greater than five times the photon's virtuality and the virtuality be less than $10\,\text{GeV}^2$. This requirement is only satisfied in a portion of the data shown.

5.6 Conclusions

In this chapter measurements of the inclusive dijet cross section $d\sigma/d\bar{\eta}^*$ have been described for interactions containing high transverse energy jets in the kinematic region $1.6 < Q^2 < 100$ GeV^2 and $0.1 < y < 0.7$. The results show a flatter $\bar{\eta}^*$ distribution at low Q^2 than expected from a picture of the photon interacting as a pointlike object. As Q^2 increases the distribution becomes more peaked in the region $\bar{\eta}^* \leq -2$, as expected if all the photon's momentum is involved in the interaction, pushing the jets in the direction of the photon.

When compared to Monte Carlo QCD predictions based on LO QCD the data support models in which the photon possesses a partonic quality that is suppressed logarithmically with its virtuality in accordance with the conclusions presented in chapter 4.

Using the same data, a measurement was made of the ratio $\sigma(res)/\sigma(dir)$ as a function of Q^2 in bins of the average transverse energy of the two highest E_T^* jets. The measured ratio disfavours a model that treats the photon as pointlike independent of its virtuality. The data are also inconsistent with no suppression of the photon structure with increasing Q^2 . Models which incorporate photon structure that is suppressed as Q^2 increases are able to describe the measured data.
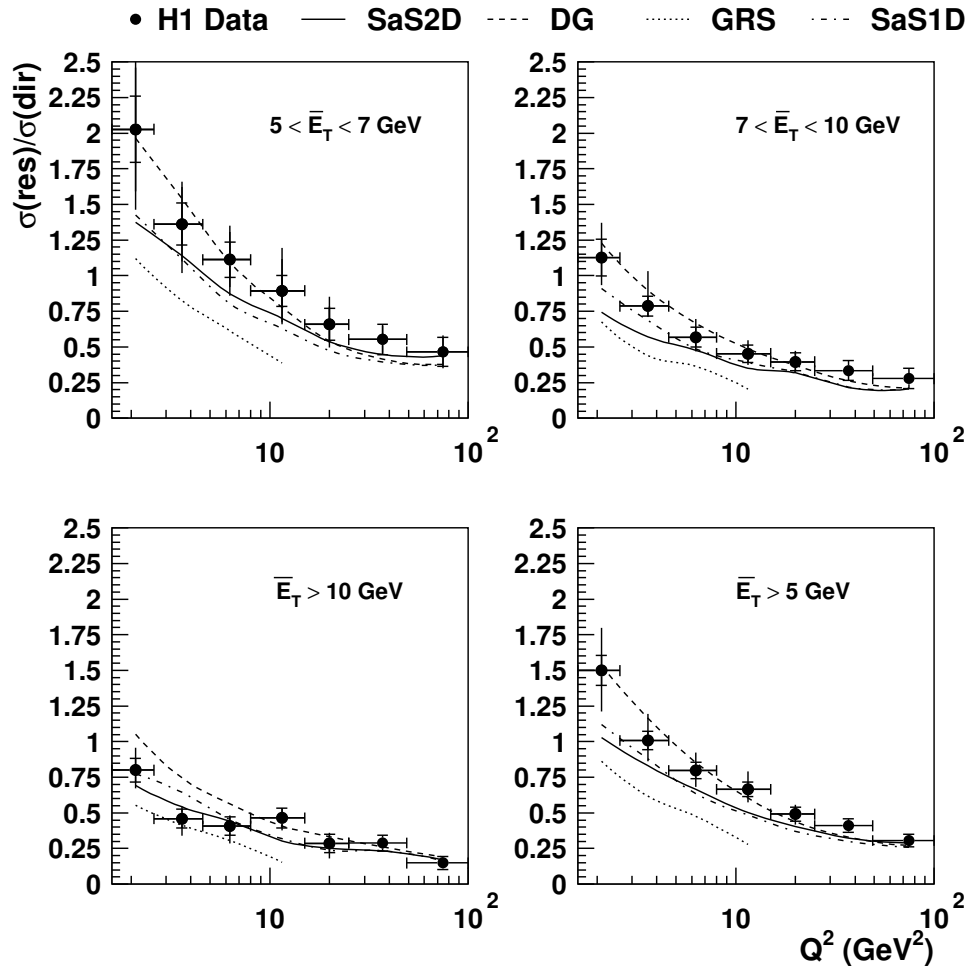
Figure 5.18: The corrected data ratio $\sigma(res)/\sigma(dir)$ as a function of Q^2 shown in three different $\bar{\mathrm{E}}_T^*$ bins. Also shown are the predictions from RAPGAP with four different choices of parton density. The DG model with GRV real photon densities and ω set to 0.2 GeV is shown as the dashed curve. The predictions from SaS2D, SaS1D and GRS are shown as the full, dot-dashed and dotted curves respectively.

Chapter 6

Conclusions

In this thesis, the inclusive jet cross sections $\mathrm{d}\sigma_{ep}/\mathrm{d}E_T^*$ and $\mathrm{d}\sigma_{ep}/\mathrm{d}\eta^*$ have been measured in the kinematic range $0.3 < y < 0.6$ and $0.65 < Q^2 < 50\,\mathrm{GeV}^2$

Models in which the photon only couples directly to a quark from the proton fail to describe the measured data in the kinematic region where $E_T^{*\,2} \gg Q^2$. Models which include both the direct coupling of the photon to a quark and also a resolved component that is suppressed with Q^2 give a good description of the data.

The fraction of the photon's energy that continues in the direction of the photon after the hard collision was measured in events containing jets of large transverse energy. This fraction is large at low Q^2 and decreases with increasing Q^2, consistent with the picture of there being a resolved component to the virtual photon that is suppressed with increasing photon virtuality.

The dijet cross section $\mathrm{d}\sigma/\mathrm{d}\bar{\eta}^*$ was measured as a function of Q^2 and of the average transverse energy of the two highest E_T^* jets, $\bar{E}_T^*$. The measured cross section was compared to a number of QCD based models describing the evolution of the photons structure with increasing virtuality. The model that gives the best description in the region in which $\bar{E}_T^* \gg Q^2$ is the Drees-Godbole model using a logarithmic suppression of real photon structure with increasing Q^2 . As expected, when $Q^2 \approx E_T^*$ the resolved contribution vanishes and a good description of the data is obtained without the need for including photon structure.

The ratio $\sigma(res)/\sigma(dir)$ was also measured as a function of Q^2 in three sepa-

rate regions of $\bar{E}_T^*$. The measured ratios confirm the picture of a resolved virtual photon with suppression as a function of Q^2. Due to the large uncertainties present in the measurement, no distinction between different models of photon structure is possible.

In conclusion, the notion of the photon possessing structure that is suppressed with increasing virtuality provides a framework which allows a description of the transition from photoproduction to DIS. An increase in data and a better understanding of the uncertainties of the measurement should allow better differentiation of the different models of virtual photon structure.

6.1   Future Measurements

The measurements presented in this thesis provide evidence that jet cross sections in the region of phase space where $E_T^2 \gg Q^2$ can be understood in terms of the virtual photon fluctuating into a partonic object which then interacts with the proton. Using shifted vertex data, the single inclusive jet cross sections were measured down to a Q^2 of $0.65\,\mathrm{GeV}^2$. The small amount of luminosity prevented dijet cross sections being measured down to such low Q^2 values.

At the start of the 1997 running period a new calorimeter was added to the H1 detector, covering the angular region between the SPACAL and the backward beampipe. This VLQ (Very Low Q^2) calorimeter will enable the measurement of the scattered electron down to very small angles covering the kinematic region $Q^2 \approx 0$ to $Q^2 \approx 1.0\,\mathrm{GeV}^2$. Due to the large cross section in this kinematic region the detector should be calibrated quickly and allow interesting physics measurements to be made in the transition region between photoproduction and DIS. In particular, measurements of jet cross sections and photon structure measurements would benefit greatly from having hermetic coverage of this low Q^2 region.

Appendix A

Evaluating correlated errors

Evaluating the correction factors used to correct the measured data for detector effects involves evaluating the ratio of events generated in a bin divided by the number of events reconstructed in the same bin.

$$C_F = \frac{N_{gen}}{N_{rec}} = \frac{\sum_n W_n}{\sum_p W_p} = \frac{a}{b} \tag{A.1}$$

If a and b were uncorrelated then the error for C_F could be found by :-

$$\delta_{C_F}^2 = \sum_{a,b} (\frac{\delta f}{\delta x_{a,b}})^2 \ \sigma_{a,b}^2 \tag{A.2}$$

One would hope (if we are not just wasting our time) that the variables $a = \sum_n W_n = N_{gen}$ and $b = \sum_p W_p = N_{rec}$ are highly correlated.

In this case more care is needed, a and b need to be broken down into independent terms :-

$$N_{gen} = N_{i,i} + N_{i,j} + N_{i,\bar{i}} = \sum W_{i,i} + \sum W_{i,j} + \sum W_{i,\bar{i}} = s + t + u$$

$$N_{rec} = N_{i,i} + N_{j,i} + N_{\bar{i},i} = \sum W_{i,i} + \sum W_{j,i} + \sum W_{\bar{i},i} = s + x + y \tag{A.3}$$

where :-

- $N_{i,i}$ = Number of events that are generated in bin i and reconstructed in bin i

  This is the term common to both a and b.

- $N_{i,j}$ = Number of events generated in bin i that migrate out of bin i

- $N_{i,\bar{i}}$ = Number of events generated in bin i but failed reconstructed cuts.

- $N_{j,i}$ = Number of events generated outside bin i that migrate into bin i.

- $N_{\bar{i},i}$ = Number of events failing generated cuts that pass reconstructed cuts in bin i.

The sensitivity of C_F to the rate of change of each of these components can be found by taking partial derivatives of C_F.

$$
\frac{\partial C_F}{\partial s} = \frac{x + y - t - u}{(s + x + y)^2} \quad \frac{\partial C_F}{\partial t} = \frac{1}{(s+x+y)} \quad \frac{\partial C_F}{\partial u} = \frac{1}{(s + x + y)}
$$
$$
\frac{\partial C_F}{\partial x} = -\frac{(s + t + u)}{(s + x + y)^2} \qquad\qquad \frac{\partial C_F}{\partial y} = -\frac{(s + t + u)}{(s + x + y)^2} \qquad (A.4)
$$

$$
\sigma^2_{C_F} = \sum \left(\frac{\partial C_F}{\partial W}\right) \qquad (A.5)
$$

If each event is generated with a weight W_ϵ then the bin content will be $\sum W_\epsilon$ and the variance of the bin content will be $\sigma^2 = \sum W^2$ and, since $\sigma^2_W = W^2$ then the variance of the correction factors can be written as:

$$
\sigma^2_{C_F} = \quad \left(\frac{N_{rec} - N_{gen}}{N^2_{rec}}\right)^2 \sum W^2_s + \left(\frac{1}{N_{rec}}\right)^2 \sum W^2_t
$$
$$
+ \quad \left(\frac{1}{N_{rec}}\right)^2 \sum W^2_u + \left(\frac{N_{gen}}{N_{rec}}\right)^2 \sum W^2_x + \left(\frac{N_{gen}}{N_{rec}}\right)^2 \sum W^2_y \qquad (A.6)
$$

Appendix B

Definition of x$_\gamma$

For a resolved event in the hadronic centre of mass system the four momenta of the photon and the proton are given by

$$q = \frac{1}{2W}(W^2 - Q^2, 0, 0, -W^2 - Q^2) \tag{B.1}$$

$$P = \frac{1}{2W}(W^2 + Q^2, 0, 0, W^2 + Q^2) \tag{B.2}$$

Here W^2 is the centre of mass energy squared.

$$W^2 = (P + q)^2 = 2Pq - Q^2 = ys - Q^2 \tag{B.3}$$

Assuming the incoming parton p_0 from the photon to be collinear with the photon, the parton's four momentum is $p_0 = x_\gamma q$. The invariant form of x_γ is then $x_\gamma = p_0 P / qP$.

If the fraction of the proton's momentum carried by the parton entering the interaction is ξ then energy and momentum conservation requires

$$x_\gamma q + \xi P = \sum_i p_i \tag{B.4}$$

where the sum is over the outgoing final state partons from the hard scattering process, substituting for q and p gives

$$\sum_i E_i = x_\gamma \frac{W^2 - Q^2}{2W} + \xi \frac{W^2 + Q^2}{2W} \tag{B.5}$$

$$\sum_i p_{zi} = -x_\gamma \frac{W^2 + Q^2}{2W} + \xi \frac{W^2 + Q^2}{2W} \tag{B.6}$$

Subtracting the two terms and rearranging in terms of x_γ leads to

$$x_\gamma = \frac{\sum_i (E^i - P_z^i)}{W} \tag{B.7}$$

Here, the summation is over all partons involved in the hard scattering process and W is the hadronic centre of mass energy and is given by $\sum_{allpartons}(E - P_z)$ of all partons in the event.

Appendix C

Tables of results

Q^2 (GeV^2)	E_T^* (GeV)	$\mathrm{d}\sigma_{ep}/\mathrm{d}E_T^*$ (nb/GeV)	$\delta(stat)$	$+\delta(sys)$	$-\delta(sys)$	$\pm\delta(norm)$
$Q^2 < 10^{-2}$	$5-7$	40.7	0.5	4.8	4.0	7.1
	$7-10$	6.4	0.2	1.0	1.0	1.3
	$10-20$	0.31	0.02	0.05	0.06	0.06
$0.65 < Q^2 < 1.2$	$4-5$	3.5	0.3	0.4	0.6	0.6
	$5-7$	1.1	0.1	0.1	0.2	0.2
	$7-10$	0.17	0.04	0.04	0.09	0.05
	$10-20$	0.016	0.008	0.012	0.009	0.005
$1.2 < Q^2 < 2.6$	$4-5$	3.4	0.3	0.5	0.6	0.5
	$5-7$	1.2	0.1	0.2	0.2	0.2
	$7-10$	0.22	0.04	0.04	0.06	0.03
	$10-20$	0.017	0.007	0.009	0.007	0.007
$2.6 < Q^2 < 4$	$4-5$	1.5	0.2	0.4	0.3	0.2
	$5-7$	0.48	0.08	0.16	0.10	0.13
	$7-10$	0.049	0.016	0.023	0.018	0.008
	$10-20$	5.1×10^{-3}	3.8×10^{-3}	5.3×10^{-3}	6.9×10^{-3}	1.3×10^{-3}
$4 < Q^2 < 9$	$4-5$	1.6	0.2	0.5	0.2	0.3
	$5-7$	0.69	0.09	0.26	0.12	0.22
	$7-10$	0.13	0.03	0.04	0.05	0.01
	$10-20$	0.024	0.011	0.019	0.016	0.006
$9 < Q^2 < 20$	$4-5$	1.10	0.03	0.12	0.16	0.12
	$5-7$	0.48	0.01	0.07	0.11	0.08
	$7-10$	0.143	0.007	0.032	0.037	0.022
	$10-20$	1.13×10^{-2}	0.09×10^{-2}	0.44×10^{-2}	0.42×10^{-2}	0.23×10^{-2}
$20 < Q^2 < 25$	$4-5$	0.26	0.02	0.06	0.08	0.04
	$5-7$	0.107	0.007	0.028	0.029	0.016
	$7-10$	0.033	0.003	0.017	0.019	0.007
	$10-20$	5.7×10^{-3}	1.0×10^{-3}	4.9×10^{-3}	60.8×10^{-3}	2.3×10^{-3}
$25 < Q^2 < 36$	$4-5$	0.33	0.02	0.06	0.07	0.04
	$5-7$	0.092	0.005	0.056	0.019	0.011
	$7-10$	0.029	0.002	0.020	0.009	0.004
	$10-20$	5.2×10^{-3}	0.6×10^{-3}	2.8×10^{-3}	2.3×10^{-3}	0.7×10^{-3}
$36 < Q^2 < 49$	$4-5$	0.19	0.01	0.08	0.05	0.03
	$5-7$	0.051	0.003	0.042	0.013	0.004
	$7-10$	0.032	0.003	0.014	0.011	0.006
	$10-20$	5.4×10^{-3}	0.7×10^{-3}	3.0×10^{-3}	2.3×10^{-3}	1.1×10^{-3}

Table C.1: The inclusive differential jet cross-section $\mathrm{d}\sigma_{ep}/\mathrm{d}E_T^*$ for jets with $-2.5 < \eta^* < -0.5$ in the $\gamma^*\mathrm{p}$ centre of mass frame measured in the range $0.3 < y < 0.6$ for nine different Q^2 ranges. The statistical, positive systematic, negative systematic and normalisation errors are given. In addition, the uncertainty in the luminosity determination leads to a 3% normalisation error for the data with $0.65 < Q^2 < 9\,GeV^2$ and a 1.5% normalisation error elsewhere.

Q^2 (GeV^2)	η^*	$\mathrm{d}\sigma_{ep}/\mathrm{d}\eta^*$ (nb)	$\delta(stat)$	$+\delta(sys)$	$-\delta(sys)$	$\pm\delta(norm)$
$0.65 < Q^2 < 1.2$	$-2.5 < \eta^* < -2.1$	1.9	0.3	0.8	0.4	0.3
	$-2.1 < \eta^* < -1.7$	1.6	0.3	0.2	0.7	0.4
	$-1.7 < \eta^* < -1.3$	1.9	0.4	0.5	0.8	0.4
	$-1.3 < \eta^* < -0.9$	1.2	0.2	0.2	0.4	0.2
	$-0.9 < \eta^* < -0.5$	0.73	0.16	0.18	0.37	0.24
$1.2 < Q^2 < 2.6$	$-2.5 < \eta^* < -2.1$	2.3	0.4	1.1	0.7	0.5
	$-2.1 < \eta^* < -1.7$	1.7	0.3	0.4	0.5	0.4
	$-1.7 < \eta^* < -1.3$	1.0	0.2	0.4	0.3	0.3
	$-1.3 < \eta^* < -0.9$	1.3	0.3	0.4	0.6	0.3
	$-0.9 < \eta^* < -0.5$	1.3	0.3	0.2	0.8	0.2
$2.6 < Q^2 < 4$	$-2.5 < \eta^* < -2.1$	0.75	0.21	0.37	0.25	0.18
	$-2.1 < \eta^* < -1.7$	0.51	0.16	0.23	0.14	0.05
	$-1.7 < \eta^* < -1.3$	0.49	0.16	0.17	0.26	0.15
	$-1.3 < \eta^* < -0.9$	0.62	0.22	0.25	0.40	0.16
	$-0.9 < \eta^* < -0.5$	0.35	0.13	0.24	0.16	0.12
$4 < Q^2 < 9$	$-2.5 < \eta^* < -2.1$	1.5	0.3	0.9	0.5	0.5
	$-2.1 < \eta^* < -1.7$	1.5	0.4	0.6	0.6	0.3
	$-1.7 < \eta^* < -1.3$	0.79	0.21	0.37	0.28	0.27
	$-1.3 < \eta^* < -0.9$	0.64	0.19	0.39	0.22	0.14
	$-0.9 < \eta^* < -0.5$	0.67	0.21	0.27	0.21	0.13
$9 < Q^2 < 20$	$-2.5 < \eta^* < -2.1$	1.25	0.09	0.22	0.27	0.20
	$-2.1 < \eta^* < -1.7$	0.78	0.08	0.14	0.16	0.14
	$-1.7 < \eta^* < -1.3$	0.62	0.06	0.12	0.15	0.10
	$-1.3 < \eta^* < -0.9$	0.68	0.06	0.15	0.18	0.12
	$-0.9 < \eta^* < -0.5$	0.48	0.04	0.11	0.24	0.09
$20 < Q^2 < 25$	$-2.5 < \eta^* < -2.1$	0.23	0.04	0.07	0.06	0.03
	$-2.1 < \eta^* < -1.7$	0.26	0.04	0.07	0.12	0.04
	$-1.7 < \eta^* < -1.3$	0.21	0.03	0.06	0.08	0.03
	$-1.3 < \eta^* < -0.9$	0.08	0.02	0.04	0.06	0.02
	$-0.9 < \eta^* < -0.5$	0.11	0.02	0.03	0.05	0.02
$25 < Q^2 < 35$	$-2.5 < \eta^* < -2.1$	0.25	0.05	0.09	0.04	0.03
	$-2.1 < \eta^* < -1.7$	0.15	0.04	0.09	0.06	0.02
	$-1.7 < \eta^* < -1.3$	0.16	0.03	0.05	0.04	0.02
	$-1.3 < \eta^* < -0.9$	0.13	0.03	0.04	0.05	0.02
	$-0.9 < \eta^* < -0.5$	0.13	0.03	0.03	0.08	0.02
$35 < Q^2 < 49$	$-2.5 < \eta^* < -2.1$	0.37	0.04	0.07	0.12	0.03
	$-2.1 < \eta^* < -1.7$	0.16	0.04	0.04	0.11	0.02
	$-1.7 < \eta^* < -1.3$	0.067	0.03	0.06	0.08	0.010
	$-1.3 < \eta^* < -0.9$	0.077	0.02	0.04	0.06	0.019
	$-0.9 < \eta^* < 0.5$	0.09	0.01	0.03	0.1	0.02

Table C.2: The inclusive differential jet cross-section $\mathrm{d}\sigma_{ep}/\mathrm{d}\eta^*$ for jets with $E_T^2 > 5\,$GeV in the γ^*p centre of mass frame measured in the range $0.3 < y < 0.6$ for nine different Q^2 ranges. The statistical, positive systematic, negative systematic and normalisation errors are given. In addition, the uncertainty in the luminosity determination leads to a 3% normalisation error for the data with $0.65 < Q^2 < 20\,GeV^2$ and a 2.0% normalisation error elsewhere.

Q^2 (GeV^2)	E_T^* (GeV)	$\bar{\eta}$	$\mathrm{d}\sigma_{ep}/\mathrm{d}\eta^*$ (nb)	$\delta(stat)$	$+\delta(sys)$	$-\delta(sys)$
$1.6 < Q^2 < 2.6$	$5 < E_T^* < 7$	$-2.5 < \eta^* < -2.2$	1.9	0.3	0.8	0.4
		$-2.2 < \eta^* < -1.9$	1.6	0.3	0.2	0.7
		$-1.9 < \eta^* < -1.6$	1.9	0.4	0.5	0.8
		$-1.6 < \eta^* < -1.3$	1.2	0.2	0.2	0.4
		$-1.3 < \eta^* < -1.0$	0.73	0.16	0.18	0.37
		$-1.0 < \eta^* < -0.7$	0.73	0.16	0.18	0.37
		$-0.7 < \eta^* < -0.4$	0.73	0.16	0.18	0.37
$1.6 < Q^2 < 2.6$	$7 < E_T^* < 10$	$-2.5 < \eta^* < -2.2$	1.9	0.3	0.8	0.4
		$-2.2 < \eta^* < -1.9$	1.6	0.3	0.2	0.7
		$-1.9 < \eta^* < -1.6$	1.9	0.4	0.5	0.8
		$-1.6 < \eta^* < -1.3$	1.2	0.2	0.2	0.4
		$-1.3 < \eta^* < -1.0$	0.73	0.16	0.18	0.37
		$-1.0 < \eta^* < -0.7$	0.73	0.16	0.18	0.37
		$-0.7 < \eta^* < -0.4$	0.73	0.16	0.18	0.37
$1.6 < Q^2 < 2.6$	$10 < E_T^*$	$-2.5 < \eta^* < -2.2$	1.9	0.3	0.8	0.4
		$-2.2 < \eta^* < -1.9$	1.6	0.3	0.2	0.7
		$-1.9 < \eta^* < -1.6$	1.9	0.4	0.5	0.8
		$-1.6 < \eta^* < -1.3$	1.2	0.2	0.2	0.4
		$-1.3 < \eta^* < -1.0$	0.73	0.16	0.18	0.37
		$-1.0 < \eta^* < -0.7$	0.73	0.16	0.18	0.37
		$-0.7 < \eta^* < -0.4$	0.73	0.16	0.18	0.37
$2.6 < Q^2 < 4.6$	$5 < E_T^* < 7$	$-2.5 < \eta^* < -2.2$	1.9	0.3	0.8	0.4
		$-2.2 < \eta^* < -1.9$	1.6	0.3	0.2	0.7
		$-1.9 < \eta^* < -1.6$	1.9	0.4	0.5	0.8
		$-1.6 < \eta^* < -1.3$	1.2	0.2	0.2	0.4
		$-1.3 < \eta^* < -1.0$	0.73	0.16	0.18	0.37
		$-1.0 < \eta^* < -0.7$	0.73	0.16	0.18	0.37
		$-0.7 < \eta^* < -0.4$	0.73	0.16	0.18	0.37
$2.6 < Q^2 < 4.6$	$7 < E_T^* < 10$	$-2.5 < \eta^* < -2.2$	1.9	0.3	0.8	0.4
		$-2.2 < \eta^* < -1.9$	1.6	0.3	0.2	0.7
		$-1.9 < \eta^* < -1.6$	1.9	0.4	0.5	0.8
		$-1.6 < \eta^* < -1.3$	1.2	0.2	0.2	0.4
		$-1.3 < \eta^* < -1.0$	0.73	0.16	0.18	0.37
		$-1.0 < \eta^* < -0.7$	0.73	0.16	0.18	0.37
		$-0.7 < \eta^* < -0.4$	0.73	0.16	0.18	0.37
$2.6 < Q^2 < 4.6$	$10 < E_T^*$	$-2.5 < \eta^* < -2.2$	1.9	0.3	0.8	0.4
		$-2.2 < \eta^* < -1.9$	1.6	0.3	0.2	0.7
		$-1.9 < \eta^* < -1.6$	1.9	0.4	0.5	0.8
		$-1.6 < \eta^* < -1.3$	1.2	0.2	0.2	0.4
		$-1.3 < \eta^* < -1.0$	0.73	0.16	0.18	0.37
		$-1.0 < \eta^* < -0.7$	0.73	0.16	0.18	0.37
		$-0.7 < \eta^* < -0.4$	0.73	0.16	0.18	0.37

Q^2 (GeV^2)	E_T^* (GeV)	$\bar{\eta}$	$\mathrm{d}\sigma_{ep}/\mathrm{d}\eta^*$ (nb)	$\delta(stat)$	$+\delta(sys)$	$-\delta(sys)$
$4 < Q^2 < 9$	$5 < E_T^* < 7$	$-2.5 < \eta^* < -2.2$	1.5	0.3	0.9	
		$-2.2 < \eta^* < -1.9$	1.5	0.4	0.6	0.3
		$-1.9 < \eta^* < -1.6$	0.79	0.21	0.37	0.28
		$-1.6 < \eta^* < -1.3$	0.64	0.19	0.39	0.22
		$-1.3 < \eta^* < -1.0$	0.67	0.21	0.27	0.21
		$-1.0 < \eta^* < -0.7$	0.67	0.21	0.27	0.21
		$-0.7 < \eta^* < -0.4$	0.67	0.21	0.27	0.21
$9 < Q^2 < 20$		$-2.5 < \eta^* < -2.2$	1.25	0.09	0.22	0.27	0.20
		$-2.2 < \eta^* < -1.9$	0.78	0.08	0.14	0.16	0.14
		$-1.9 < \eta^* < -1.6$	0.62	0.06	0.12	0.15	0.10
		$-1.6 < \eta^* < -1.3$	0.68	0.06	0.15	0.18	0.12
		$-1.3 < \eta^* < -1.0$	0.48	0.04	0.11	0.24	0.09
		$-1.0 < \eta^* < -0.7$	0.48	0.04	0.11	0.24	0.09
		$-0.7 < \eta^* < -0.4$	0.48	0.04	0.11	0.24	0.09
$20 < Q^2 < 25$		$-2.5 < \eta^* < -2.2$	0.23	0.04	0.07	0.06	0.03
		$-2.2 < \eta^* < -1.9$	0.78	0.08	0.14	0.16	0.14
		$-1.9 < \eta^* < -1.6$	0.62	0.06	0.12	0.15	0.10
		$-1.6 < \eta^* < -1.3$	0.68	0.06	0.15	0.18	0.12

E_T^* (GeV)	Q^2 (GeV^2)	$\sigma(res)/\sigma(dir)$	$\delta(stat)$	$+\delta(sys)$	$-\delta(sys)$
$5 < E_T^* < 7$	$1.6 - 2.6$	3.495	0.231	0.425	0.334
	$2.6 - 4.6$	2.415	0.148	0.137	0.151
	$4.6 - 8.0$	1.888	0.124	0.06	0.050
	$8.0 - 15$	1.503	0.109	0.10	0.031
	$15 - 25$	1.267	0.112	0.02	0.001
	$25 - 49$	1.1559	0.107	0.01	0.018
	$49 - 100$	0.8994	0.100	0.03	0.027
$7 < E_T^* < 10$	$1.6 - 2.6$	1.447	0.130	0.205	0.144
	$2.6 - 4.6$	0.834	0.0692	0.236	0.032
	$4.6 - 8.0$	0.743	0.070	0.109	0.071
	$8.0 - 15$	0.6347	0.062	0.070	0.050
	$15 - 25$	0.540	0.0625	0.045	0.028
	$25 - 49$	0.558	0.069	0.084	0.020
	$49 - 100$	0.482	0.0717	0.066	0.076
$E_T^* > 10$	$1.6 - 2.6$	0.601	0.084	0.106	0.280
	$2.6 - 4.6$	0.479	0.065	0.053	0.10
	$4.6 - 8.0$	0.497	0.065	0.033	0.10
	$8.0 - 15$	0.476	0.069	0.015	0.049
	$15 - 25$	0.378	0.064	0.036	0.086
	$25 - 49$	0.366	0.056	0.034	0.030
	$49 - 100$	0.228	0.045	0.032	0.019
$E_T^* > 5$	$1.6 - 2.6$	2.203	0.105	0.28	0.267
	$2.6 - 4.6$	1.454	0.064	0.170	0.132
	$4.6 - 8.0$	1.20	0.057	0.110	0.100
	$8.0 - 15$	0.978	0.051	0.110	0.078
	$15 - 25$	0.796	0.050	0.040	0.055
	$25 - 49$	0.736	0.048	0.051	0.57
	$49 - 100$	0.563	0.045	0.055	0.090

Table C.4: The measured ratio $\sigma(res)/\sigma(dir)$ as a function of Q^2 shown in three different $\bar{\mathrm{E}}_T^*$ bins.

Bibliography

[1] B. R. Martin and G. Shaw. *Particle Physics. John Wiley and Sons, 1992*

[2] D. H. Perkins. *Introduction to High Energy Physics.* Addison-Wesley, 1982

[3] F. Halzen and A. D. Martin. *Quarks and Leptons.* Wiley, 1984

[4] G. Altarelli and G.Parisi. *Nucl. Phys. B 126(1997)298*

[5] H1 Collaboration, C. Adloff et al., Phys. Lett. **B415** (1997) 418.

[6] H1 Collaboration, *Measurement of the Inclusive Di-Jet Cross-Section in Photoproduction and the Determination of an Effective Parton Distribution in the Photon*, preprint DESY-97-164, submitted to Z. Phys C.

[7] Altarelli-Parisi

[8] PLUTO Collab, Ch. Berger et al., Phys. Lett. B142 (1984) 111.

[9] M. Erdmann. The Partonic Structure of the Photon, Springer STMP 138 (1997)

[10] J.J. Sakurai, Ann. Phys. II(1960) I

[11] F Borzumati, G Schuler, Real and virtual photon contributions to inelastic *ep* scattering, Z. Phys C. 58, 1993

[12] E Witten, Nucl. Phys B120 (1977) 189

[13] D.W. Duke and J.F. Owens Phys Rev. D22 (1980) 2280
C. Berger and W. Wagner Phys Rept 146:1 (1987)

[14] M. Glück, E. Reya and M. Stratmann, Phys. Rev. **D54** (1996) 5515.

[15] M. Glück, E. Reya and A. Vogt, Z. Phys. C67 (1995) 133

[16] S. Frixione, M. Mangano, P. Nason and G. Ridolfi, Phys. Lett.**B319** (1993) 339.

[17] C. F. v. Weizsäcker, Z. Phys. **88** (1934) 612
E. J. Williams, Phys. Rev. **45** (1934) 729.

[18] H1 Collaboration, I. Abt et al., Nucl. Instr. and Meth. **A386** (1997) 310 and **A386** (1997) 348.

[19] H1 Calorimeter Group, B. Andrieu et al., Nucl. Instr. and Meth. **A336** (1993) 460.

[20] H1 SPACAL group, R. D. Appuhn et al., DESY preprint 96-171, submitted to Nucl. Instr. and Meth.

[21] H1 SPACAL group I. Gorelov, M. Weber., Performance of the H1 Lead/Scintillating-Fibre Calorimeter, H1 internal note

[22] Performance of an Electromagnetic Lead/Scintillating-Fibre Calorimeter for the H1 detector, H1 SPACAL Group.

[23] H1 Collaboration, C. Adloff et al., Nucl.Phys. **B497** (1997) 3.

[24] H1 Calorimeter Group, Nucl. Instr. and Meth. **A336** (1993) 499.

[25] H1 Collaboration, Technical Proposal for the Upgrade of the Backward Region of the H1 detector, DESY Internal Report, PRC-93/02.

[26] JADE collaboration. W. Bartel et al. Zeit Phys. **C33 (1986) 23.**
R. Engel, Proceedings of the XXIXth Reconre de Morion

[27] **S. Catani, Yu.L. Dokshitzer and B.R. Webber Phys. Lett. B285 (1992) 291.**

[28] **ZEUS Collaboration; M.Derrick et al., Phys. Lett. B354 (1995) 163 Study of the Photon Remnant in Resolved Photoproduction at HERA**

[29] **S.D. Ellis, D.E. Soper, Phys.Rev D48 (1993) 3160**

[30] **M. Seymour, k_t algorithm for DIS**

[31] S. Levonian, A. Panitch, Treatment of the Proton Satellite Bunches in 1994 Data, H1 Internal Note , H1-09/95-454.

[32] M. Dirkmann, K. Pfeiffer, Improved position-reconstruction in the SpaCal's inner region, H1 Internal Note , H1-01/97-512

[33] OPAL Collaboration. Z. Phys C47, page 505.

[34] R. Brun et al, GEANT3 User's Guide, CERN-DD/EE 84-1, Geneva (1987)

[35] T. Sjöstrand, Comp. Phys. Comm. 82 (1994) 74.
T. Sjöstrand, CERN preprint TH-7112-93 (Dec. 1993, revised Aug. 1994)

[36] G. Ingelman, Proc. of the Workshop Physics at HERA, ed W. Buchmüller and G. Ingelman, Oct. 1991, Vol. 3, 1366.

[37] R. Engel, Proceedings of the XXIXth Recontre de Moriond (1994) ed. J Tran Thanh Van, (edition frontieres, 1994) 321.

[38] L. Lönnblad, Comp. Phys. Comm. 71 (1992) 15.

[39] G. Gustafson and U. Petterson, Nucl. Phys. B306 (1988) 746.
G. Gustafson, Phys. Lett. B175 (1986) 453.
B. Andersson et al., Z. Phys. C43 (1989) 625.

[40] G. Marchesini, B. Webber et al., Comp. Phys. Comm. 67 (1992) 465.

[41] H. Jung, Comp. Phys. Comm. 86 (1995) 147. RAPGAP 2.06 manual, to be published.

[42] DJANGO: The interface for the event generators HERACLES and LEPTO, Proceedings, Physics at HERA, vol 3 1419-1432
G. Schuler, H. Spiesberger (1991)

[43] M. Wobish, H1 note (1997)

[44] M. Drees and R. Godbole, Phys. Rev. D50 (1994) 3124.

[45] F. Borzumati and G. Schuler, Z. Phys. C58 (1993) 139.

[46] T. Sjöstrand and G. A. Schuler, Phys. Lett. B376 (1996) 193.

[47] M. Glück, E. Reya and M. Stratmann DO-TH 96/08 1996

[48] Jet Photoproduction and QCD at HERA, R. Gregory Feild, Pennsylvania State University, 1995

[49] HERACLES 4.4; A. Kwiatkowski, H. Spiesberger and H.-J. Möhring, Comp. Phys. Comm. 69 (1992) 155.

[50] U. Bassler, G. Bernadi, On the Kinematic Reconstruction of Deep Inelastic Scattering at HERA: the $\sum$ Method, DESY preprint, DESY 94-231

[51] J. Spiekermann Die Messung der Rate von 2-jet Ereignissen in tiefinelasticher Streuung bei HERA Dortmand 1997

[52] S. Frixione and G. Ridolfi, Nucl. Phys. B507 (1997) 315

[53] Jets and Energy Flow in Photon-Proton Collisions at HERA, H1 Collaboration, S. Aid et al., hep-ex/9511012 29 Nov 1999

[54] To be filled in...

[55]

[56] Survey of recent data on photon structure and resolved photon processes, hep-ph/9806291